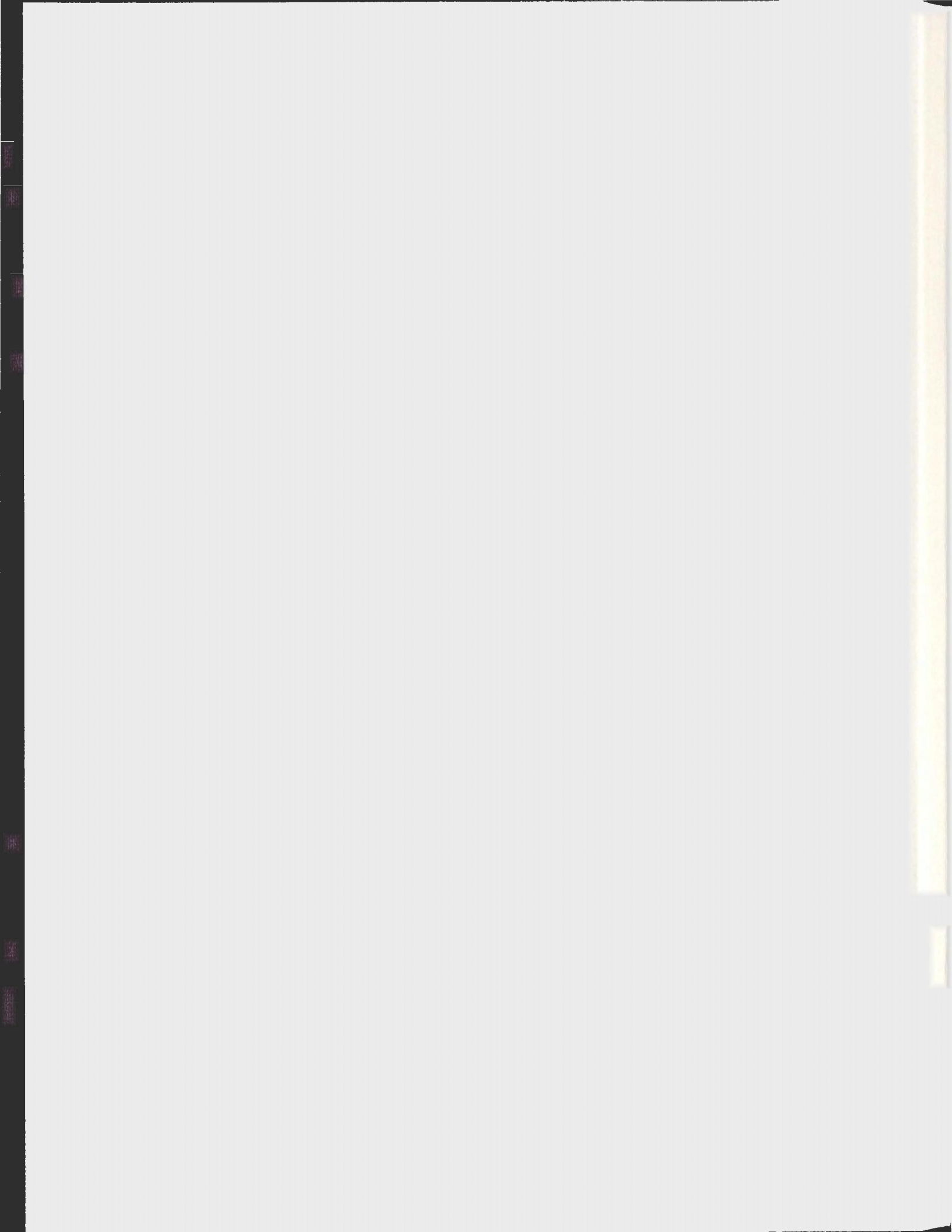


MODEL STUDY OF COUPLED
PHYSICAL-BIOGEOCHEMICAL VARIABILITY IN
THE LABRADOR SEA

HAKASE HAYASHIDA



Model Study of Coupled Physical-Biogeochemical Variability in the Labrador Sea

by

© Hakase Hayashida

A thesis submitted to the
School of Graduate Studies
in partial fulfilment of the
requirements for the degree of
Master of Science

Department of Physics and Physical Oceanography
Memorial University of Newfoundland

September 2013

St. John's

Newfoundland

Abstract

This thesis presents results from a model study of coupled physical-biogeochemical variability in the Labrador Sea. The coupled physical-biogeochemical ocean model (OPA-PISCES) is implemented for three monitoring stations in the Labrador Sea; two of these stations are located on the shelves of the western and eastern parts of the basin, whereas the third station is in the central Labrador Sea. The results of the hindcasting for 1994 are validated with available observations. The results of the sensitivity analysis suggest that the model response to parameter variations differs from region to region. The parameters with highest model sensitivity are identified for each station. The simulated seasonal variability of the low trophic level ecosystem dynamics and their relations to coupled physical-biogeochemical processes are discussed. The seasonal variability of dissolved inorganic carbon (DIC) is driven by the bloom drawdown of surface DIC and export through sinking, while the simulated surface $p\text{CO}_2$ concentration appears to be underestimated throughout the year. Besides the process study of the coupled physical-biogeochemical system at the selected regions in the Labrador Sea, the present study demonstrates the applicability of the PISCES ocean biogeochemical model for regional coupled physical-biogeochemical modeling.

Acknowledgements

First of all, I would like to thank my supervisor, Dr. Entcho Demirov, for his generous support towards the completion of my thesis. I would also like to thank the professors, staff, and colleagues in the Department of Physics and Physical Oceanography for their help. I would like to acknowledge the financial support of the Natural Sciences and Engineering Research Council of Canada (NSERC) and Memorial University of Newfoundland (MUN). Finally, I would like to thank my wife, Aishah Bakhtiar, for her patience and my family back home for their encouragements.

Contents

Abstract	ii
Acknowledgements	iii
List of Tables	viii
List of Figures	ix
1 Introduction	1
1.1 Ocean Carbon Cycle	2
1.1.1 Air-Sea Exchange and Marine Carbon Chemistry	4
1.1.2 Physical and Biological Drawdown of Surface DIC	5
1.2 The Labrador Sea	9
1.2.1 Physical Characteristics	9
1.2.1.1 Seasonal Variability	12
1.2.1.2 Interannual Variability and its connection to the North Atlantic Oscillation	13
1.2.2 Biogeochemical Characteristics	15
1.2.2.1 Seasonal Cycle	17

1.2.2.2	Interannual Variability	19
1.3	Objectives	21
1.4	Organization	21
2	Methods	22
2.1	Coupled Physical-Biogeochemical Ocean Model	22
2.1.1	Physical Model	23
2.1.2	Biogeochemical Model	25
2.2	Experimental Design	28
2.2.1	Studied Regions	28
2.2.2	Data for Model Validation and Initialization	28
2.2.3	Model Implementation	29
3	Model Validation and Sensitivity to Parameter Variations	33
3.1	Model-Data Comparison	33
3.1.1	Vertical Structures of Physical and Biogeochemical Tracers . .	34
3.1.2	Seasonal Evolution of Primary Productivity	36
3.2	Model Sensitivity to Parameter Variations	40
4	Simulation of Coupled Physical-Biogeochemical Seasonal Variability	
	in the Labrador Sea	51
4.1	Seasonal Physical and Biogeochemical Variability	52
4.1.1	Simulated Mixed Layer Depth and Surface Conditions	52
4.1.2	Simulated Variability in the Surface 100 m Layer	53
4.2	Simulated Annual Carbon Cycle	62

5	Conclusions	68
6	Future Work	71
	Bibliography	73
A	PISCES	95
A.1	Model Equations	95
A.1.1	Nanophytoplankton	95
A.1.2	Diatoms	98
A.1.3	Chlorophyll in nanophytoplankton and diatoms	99
A.1.4	Iron in nanophytoplankton and diatoms	100
A.1.5	Silicon in diatoms	101
A.1.6	Microzooplankton	102
A.1.7	Mesozooplankton	103
A.1.8	Dissolved organic carbon	104
A.1.9	Small particulate organic carbon	106
A.1.10	Big particulate organic carbon	107
A.1.11	Small particulate organic iron	108
A.1.12	Big particulate organic iron	109
A.1.13	Biogenic silica	109
A.1.14	Calcite	110
A.1.15	Nitrate	111
A.1.16	Ammonium	112
A.1.17	Phosphate	112

A.1.18 Silicate	113
A.1.19 Iron	113
A.1.20 Dissolved Inorganic Carbon	114
A.1.21 Total alkalinity	115
A.1.22 Dissolved oxygen	116
A.2 External supply of nutrients	116
A.2.1 Atmospheric dust deposition	117
A.2.2 River discharge	117
A.2.3 Reductive Mobilization of Iron from Marine Sediments	118
A.2.4 Bottom Boundary Conditions	119
A.3 Model State Variables	119
A.4 Model Parameters	121
A.5 Namelist Parameters	127

List of Tables

A.1	Description of the PISCES state variables	120
A.2	PISCES model parameters	121
A.3	Model parameters listed in <i>namelist_pisces</i> of NEMO version 3.4.1 . .	127

List of Figures

1.1	Schematic diagram for the global carbon cycle. The reservoir sizes and natural fluxes of carbon prior to the industrial revolution are indicated in black, and the reservoir sizes and fluxes after the revolution (therefore, anthropogenic effects) are shown in red. Source: http://www.ipcc.ch/graphics/ar4-wg1/jpg/fig-7-3.jpg	3
1.2	Ocean carbon uptake. Source: http://pmel.noaa.gov/co2/files/pmel-research.003.jpg	6
1.3	The low trophic level marine food web. Source: http://www1.whoi.edu/general_info/gallery_modeling/slide4.html	8
1.4	Map of the Labrador Sea with the locations of AR7W monitoring line (in green) and stations (numbered 8, 15, and 25). The bathymetry contour interval is 1000 m.	11
1.5	The North Atlantic Oscillation index. Data provided by the Climate Analysis Section, NCAR, Boulder, USA, Hurrell (1995). Updated regularly. Accessed 20 July 2013.	15

1.6	Seasonal-mean surface chlorophyll-a concentration in the Labrador Sea during a) winter, b) spring, c) summer, and d) fall. Source: http://oceandata.sci.gsfc.nasa.gov/SeaWiFS/Mapped/	18
2.1	Schematic diagram of PISCES	27
2.2	Initial data for a) nitrate, b) phosphate, c) silicate, d) iron, e) oxygen, f) dissolved organic carbon, g) dissolved inorganic carbon, and h) total alkalinity	32
3.1	Simulated and observed vertical profiles of active and passive tracers at Station 8	37
3.2	Same as Figure 3.1, but at Station 15	38
3.3	Same as Figure 3.1, but at Station 25	39
3.4	Simulated (<i>black</i>) and measured (<i>red</i>) temporal evolutions of weekly-averaged surface chlorophyll concentration at Station 8 (a), 15 (b), and 25 (c).	41
3.5	Sensitivity of the diatoms bloom to the 80 model parameters at Station 8, quantified as the standard deviation of Δ DCHL.	45
3.6	Same as Figure 3.5, but for Station 15	46
3.7	Same as Figure 3.5, but for Station 25	47
3.8	Diatoms response to variations in the key parameters at Station 8	48
3.9	Same as Figure 3.8, but for Station 15	49
3.10	Same as Figure 3.8, but for Station 25	50

4.1	Simulated evolutions of a) turbocline depth, b) atmospheric wind at 10 above sea surface, c) shortwave radiation, and d) sea-ice cover. . .	54
4.2	The evolution of simulated a) temperature, b) salinity, c) dissolved inorganic carbon, d) nitrate, e) ammonium, f) phosphate, g) iron, and h) silicate at Station 8	56
4.3	The evolution of simulated a) nanophytoplankton, b) diatoms, c) microzooplankton, d) mesozooplankton, e) dissolved organic matter, f) small particulate organic carbon, g) big particulate organic carbon, and h) calcite and i) biogenic silica at Station 8	57
4.4	Same as Figure 4.2, but at Station 15	59
4.5	Same as Figure 4.3, but at Station 15	60
4.6	Same as Figure 4.2, but at Station 25	63
4.7	Same as Figure 4.3, but at Station 25	64
4.8	Simulated daily-mean a) sea-air $\Delta p\text{CO}_2$, b) surface chlorophyll concentration, and c) DIC flux at Stations 8, 15, 25	67

Chapter 1

Introduction

Over the last 420,000 years, the earth's climate system has operated within a relatively constrained domain of atmospheric CO₂ concentration and temperature, including the four glacial-interglacial cycles [27]. However, since the beginning of the industrial revolution, human-induced (anthropogenic) activities have altered the global carbon cycle drastically [19], and subsequently, the present-day atmospheric CO₂ concentration has exceeded its natural variability [94]. Understanding the consequences of such change on the climate system and the potential impacts on the constituents of the earth system, namely the ocean and terrestrial biosphere, is essential to improve the predictability of the fate of our planet in the coming century.

The global carbon cycle describes the continuous movement of carbon and compounds involving a number of complex physical, chemical, and biological processes on the Earth. Figure 1.1 illustrates the carbon exchange between and within the different components of the earth system, including the atmosphere, ocean, and land. The total amount of carbon in the atmosphere, in the form of carbon dioxide (CO₂),

is a good indicator for characterizing the status of the cycle [108], since it is a relatively small reservoir that acts as a conveyor of carbon exchange between two other important reservoirs: the ocean and terrestrial biosphere. The ocean is the largest carbon reservoir in the earth system, accounting for approximately 85 % of the total inorganic carbon available on the planet. This is equivalent to about 50 times the amount of inorganic carbon present in the atmosphere. On a timescale of decades to millions of years, air-sea interaction plays the dominant role in controlling the atmospheric CO₂ concentration [99].

In recent years, numerical models have become important tools in studies of the carbon cycle and other biogeochemical and climatological processes (e.g. [115, 109, 50, 97]). A number of collaborative research projects, such as the Coupled Model Intercomparison Project (CMIP; <http://cmip-pcmdi.llnl.gov/>), have been undertaken to investigate the responses and feedback of the ocean carbonate system to ongoing climate change on regional to global scales. In the following sections, ocean carbon cycle processes and their role in atmospheric CO₂ uptake are discussed in the context of an open ocean. The Labrador Sea, the region of interest in the current study, is introduced, followed by the goals and organization of the thesis.

1.1 Ocean Carbon Cycle

The oceans play a crucial role in regulating the atmospheric CO₂ concentration as it exchanges vast amounts of CO₂ at the air-sea interface within short periods of time. In fact, more than 90 Gt of inorganic carbon are transferred from the surface ocean to the atmosphere and vice versa every year (Figure 1.1).

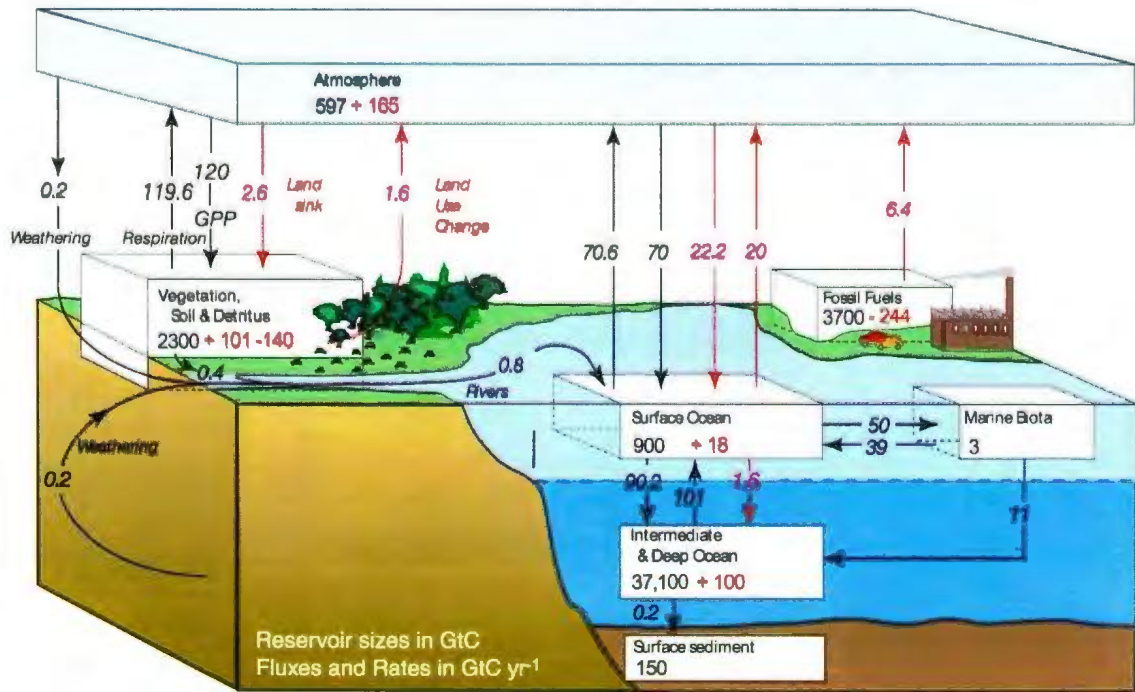
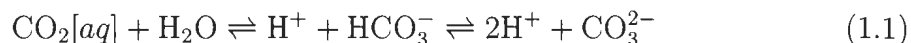


Figure 1.1: Schematic diagram for the global carbon cycle. The reservoir sizes and natural fluxes of carbon prior to the industrial revolution are indicated in black, and the reservoir sizes and fluxes after the revolution (therefore, anthropogenic effects) are shown in red. Source: <http://www.ipcc.ch/graphics/ar4-wg1/jpg/fig-7-3.jpg>

1.1.1 Air-Sea Exchange and Marine Carbon Chemistry

Carbon dioxide is continuously exchanged between the atmosphere and the ocean, primarily through molecular diffusion caused by the difference in the partial pressure of gaseous CO_2 ($p\text{CO}_2$) between the two media. The fluxes between the atmosphere and the ocean depend on the intensity and scale of turbulent fluctuations in the near-surface thin layer of the atmosphere. In practical ocean simulations, the turbulent fluxes are defined as functions of characteristics of the atmospheric boundary layer, such as temperature, humidity, and wind speed [140] [89].

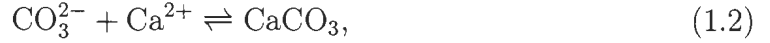
The carbon dioxide dissolved in seawater, the aqueous carbon dioxide $\text{CO}_2[\text{aq}]$, immediately reacts with water (H_2O) to form bicarbonate (HCO_3^-) ion, which may dissociate once more to form carbonate (CO_3^{2-}) ion, according to the following chemical reactions:



These three carbonate compounds comprise most of the dissolved inorganic carbon (DIC) in seawater¹. The chain of these reactions, known as the buffer system, reduces the oceanic $p\text{CO}_2$ and hence allows more atmospheric CO_2 uptake. The direction of the above equilibria depends on the pH level of seawater. The Bjerrum plot [9] is often used to identify the dominant carbonate species at a particular pH level [1], as well as to track the response of carbonate system to changes in pH [141]. The typical seawater pH is around 8.1 [53], where the equilibrium state of the DIC reactions (Equation 1.1) is HCO_3^- . Under such circumstances, the oceanic $p\text{CO}_2$ is buffered, and therefore

¹The aqueous carbon dioxide also reacts with water to form carbonate acid (H_2CO_3). However, the concentration of H_2CO_3 is less than 0.3 % of the aqueous carbon dioxide [59] and therefore it is neglected here.

more atmospheric CO_2 enters the ocean. Occasionally², a further chemical reaction of carbonate ion with calcium ion (Ca^{2+}) takes place:



where CaCO_3 is calcium carbonate in solid form. While this reaction is possible (provided that the set of Ca^{2+} and CO_3^{2-} concentrations exceeds a certain threshold for the reaction to occur), it is generally prevented by the presence of other compounds that are taking up calcium ions for their calcification. Nevertheless, if the above reaction (Equation 1.2) does occur, by the Le Chatelier's principle [116], additional CO_2 would be removed from the atmosphere to compensate for the loss of carbonate ion. Hence, the formation of calcium carbonate enhances the oceanic CO_2 uptake, which leads to acidification and the reduction of carbonate ion concentration, and therefore shifts the equilibrium state of Equation 1.2 to the left. The overall effect of increased CaCO_3 formation through this process is therefore, the weakening of the CO_2 sink.

1.1.2 Physical and Biological Drawdown of Surface DIC

Despite the fact that the external supply of oceanic DIC (i.e. atmospheric CO_2) enters from the sea surface, the DIC concentration increases with depth especially below 300 m, where it remains substantially higher than the surface concentration in all ocean basins [27]. This surface-to-deep DIC gradient is caused by a combination of physical, chemical, and biological processes that transport the surface DIC into the ocean interior. The two fundamental processes responsible for this DIC export are

²Most CaCO_3 production in the ocean is biogenic and not geochemical [57].

the solubility and biological pumps (Figure 1.2). The efficiency of the solubility and biological pumps are highly constrained by climatic conditions which affect ocean circulation, stratification, temperature, salinity, wind stress, and sea-ice cover. In turn, these pumps determine the vertical inventory of atmospheric CO_2 .

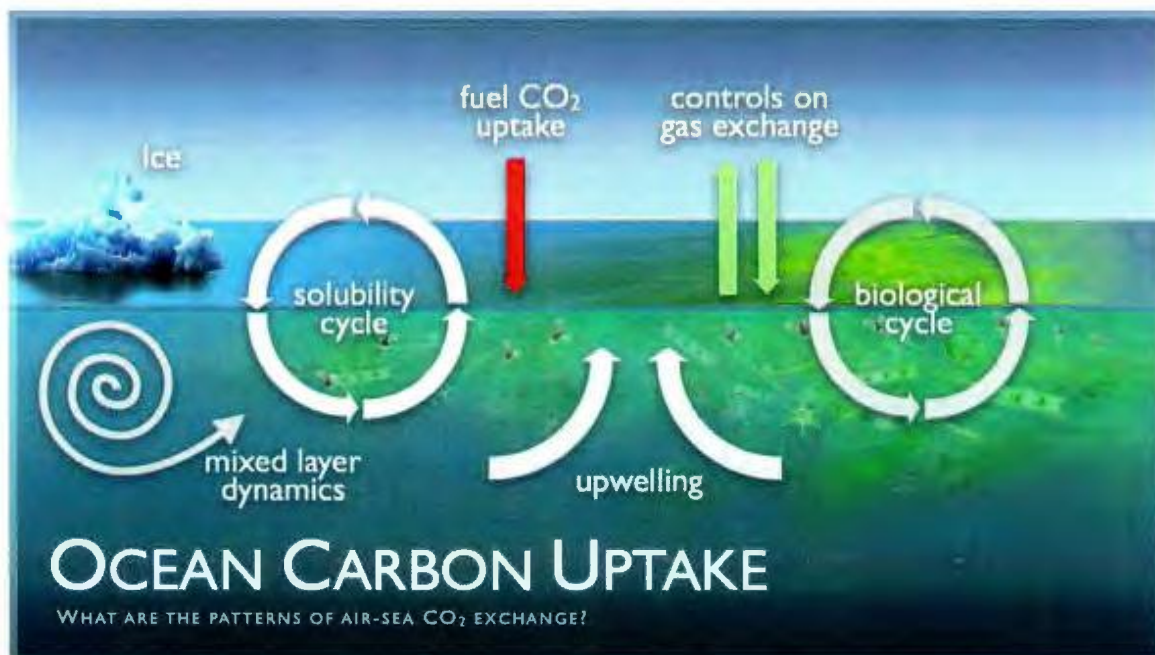


Figure 1.2: Ocean carbon uptake. Source: <http://pmel.noaa.gov/co2/files/pmel-research.003.jpg>

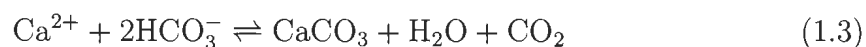
Solubility Pump

The solubility pump is a physico-chemical process of localized sinking of water mass associated with the Meridional Overturning Circulation (MOC) [19]. The pump is highly active in regions of cold and dense water mass formation at high latitudes, especially in the North Atlantic, off the coast of Greenland and Labrador, and in the

Southern Ocean [99]. The inorganic carbon captured in these regions sinks to deeper layers, where it travels latitudinally as part of the MOC until it is released back into the sea surface after decades to several hundred years. The solubility pump accounts for approximately one-third of the surface carbon sequestration [137].

Biological Pump

The other important process that contributes to ocean carbon uptake is the biological pump. Phytoplankton, the primary producer of marine ecosystems, consumes dissolved CO₂ and other nutrients in seawater to make plant tissue through photosynthesis. This process promotes the atmospheric CO₂ sink by reducing the surface pCO₂ concentration. Whilst most of the CO₂ taken up by phytoplankton is recycled through the marine food chain in the upper ocean (Figure 1.3), a considerable amount (approximately 25 % [28, 61]) sinks into the ocean interior in both living and dead forms. The export of marine biota (of about 11 GtC/year [19]) is significant as it keeps the atmospheric CO₂ concentration 150 to 200 ppm lower than it would be otherwise [61]. The CO₂ remineralized in the deep ocean is carried out by thermohaline circulation and is brought back into the atmosphere by upwelling. Although most of the biogenic carbon in the deep ocean is remineralized, a small portion (0.2 GtC/year [19]) reaches the seafloor where it is buried in the sediment. In addition to the biological pump explained above, several plankton species and corals utilize bicarbonate ion to form calcium carbonate shells and skeletons, according to the following chemical equilibrium:



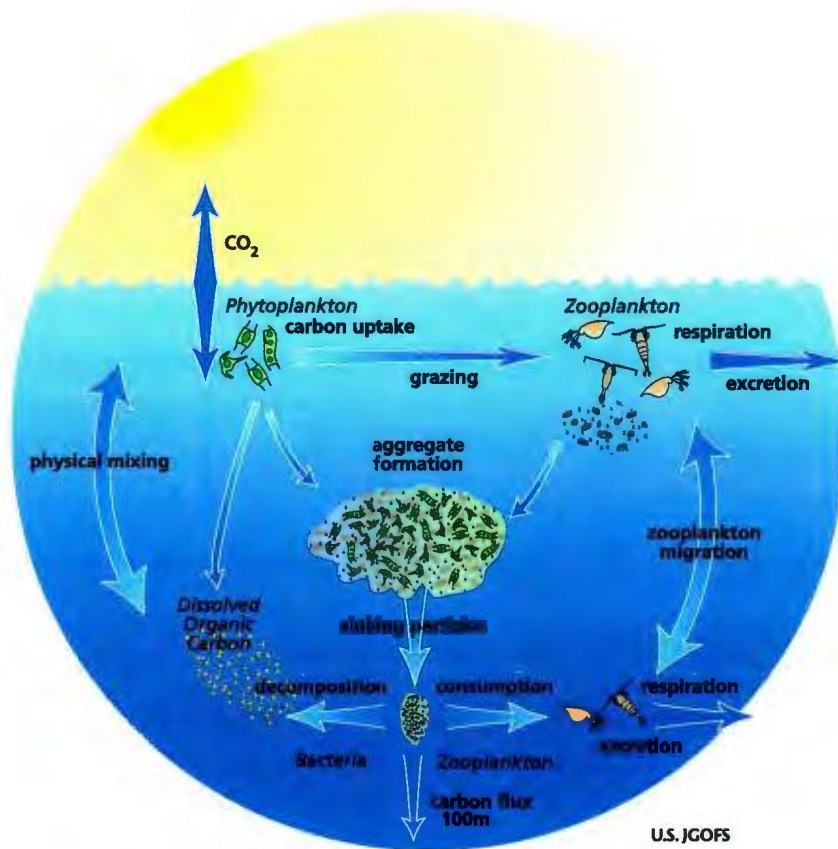


Figure 1.3: The low trophic level marine food web. Source:
http://www1.whoi.edu/general_info/gallery_modeling/slide4.html

While this biogenic calcification process produces one CO_2 molecule, two bicarbonate ions (and hence two CO_2 molecules, by the Le Chatelier's principle [116]) are required for this reaction. Therefore, the overall effect of the biological calcification is a net sink similar to the chemical calcification in Equation 1.2. Furthermore, sinking and deposition of CaCO_3 amplify the sink strength. Therefore, this production and sequestration of biogenic calcium carbonate is called the carbonate pump [137].

1.2 The Labrador Sea

As described in Section 1.1, the strength of atmospheric CO_2 uptake fundamentally depends on the efficiency of the solubility and biological pumps that maintain $p\text{CO}_2$ of surface water below the atmospheric level. One important region that both of these pumps are highly active, and hence acts as a significant sink for atmospheric CO_2 is the Labrador Sea.

1.2.1 Physical Characteristics

The Labrador Sea is the northwestern arm of the North Atlantic Ocean. The boundaries of the Sea are defined as follows [47]:

- On the North: the South end of Davis Strait and Baffin Bay.
- On the East: a line from Cape St. Francis, Canada, to Cape Farewell, Greenland.
- On the West: the East Coast of Newfoundland and Labrador and the Northeast end of the Gulf of St. Lawrence.

The general circulation of the Labrador Sea is part of the intense cyclonic flow of the subpolar North Atlantic, whereas the interior circulation is much weaker. The boundary flow consists of three major currents: the Irminger Current, West Greenland Current, and Labrador Current (Figure 1.4). The Irminger Current travels along the Greenland Coast, transporting a relatively warm and salty water mass to the Labrador Sea. This so-called Irminger Water [145] is a northern extension of the North Atlantic Current, which is additionally transformed in the Irminger Sea by surface cooling. The West Greenland Current is the northward boundary current along the west Greenland Coast, which transports low-salinity and cold water from the Nordic Seas [14]. The southward flow at the western boundary is the Labrador Current, which is a continuation of the Baffin Island Current from Hudson Strait to the Grand Banks [118]. The transport of the Labrador Current is considered to possess a strong barotropic component. The continental shelf and slope branches of the Labrador Current are estimated to be 3 and 16 Sv, respectively [100]. In the northern Labrador Sea, the branches of the West Greenland Current and the Labrador Current meander and interact to form mesoscale eddies and shelf waves, which promotes variability in this region [87]. The West Greenland Current also carries small icebergs north of 60-70 °N and larger icebergs off the West Greenland Shelf into Baffin Bay. These icebergs are transported southward by the Labrador Current, where they are either recirculated within the Labrador Sea or end up melting in the vicinity of the North Atlantic shipping lanes. The heat exchange between the interior region and the boundary current system is generated via eddy-induced transport [64].

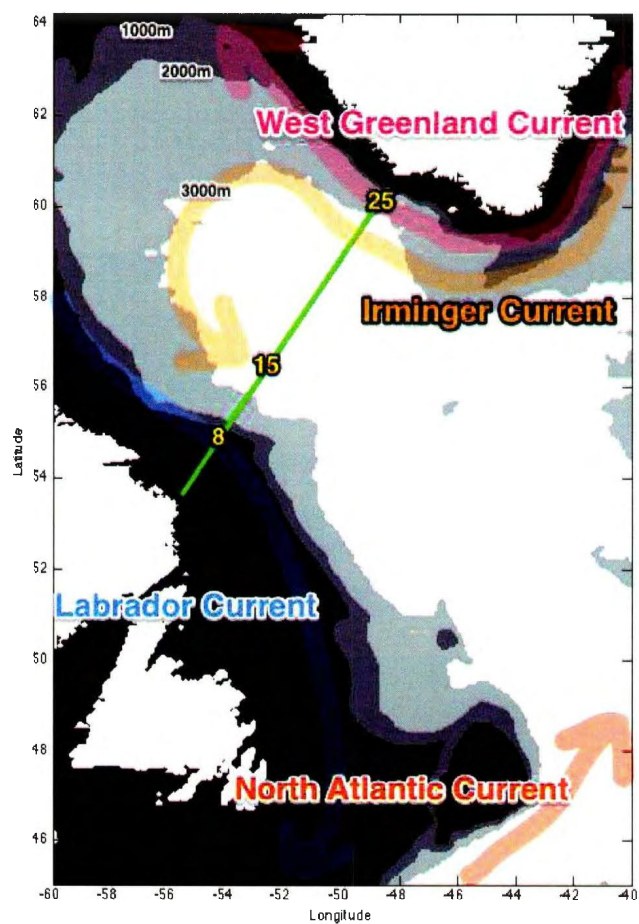


Figure 1.4: Map of the Labrador Sea with the locations of AR7W monitoring line (in green) and stations (numbered 8, 15, and 25). The bathymetry contour interval is 1000 m.

1.2.1.1 Seasonal Variability

The Labrador Sea experiences substantial seasonal variability in the surface layer [122], primarily driven by variations in surface forcing. The seasonal variability in the Sea differs regionally in the coastal and deep areas of the Labrador Sea. The winter cooling homogenizes the surface layer, resulting in the formation of the cold intermediate layer in the coastal regions [95]. The water temperature decreases until the ice that eventually forms at the surface interrupts the connection between the ocean and the atmosphere. In the spring, a strong pycnocline forms the surface layer which has anomalously low salinity due to the process of ice melting. The waters of this fresh surface layer are warmer over the summer and early fall. The melting of ice transported into the Labrador Sea by the West Greenland and Labrador Currents also contributes to the freshwater budget in the surface layer.

The mean seasonal cycle in the deep area can be characterized by two distinct periods [122]: deep convection and restratification period. The convective period takes place during winter, and is associated with a cooling of surface waters due to intensified surface heat fluxes. Consequently, severe atmospheric cooling and wind mixing during this season drive deep convection over a certain region in the central Labrador Sea. This convective process generates the formation of dense intermediate water mass, known as the Labrador Sea Water (LSW), which then sinks to depths between 500 to 2000 m [62] where it spreads throughout the subpolar North Atlantic [101]. The LSW is one of the constituents of the North Atlantic Deep Water (NADW) [56] along with two other water masses that occupy the layers below the LSW: the Gibbs Fracture Zone Water (GFZW) and the Denmark Strait Overflow Water (DSOW) [18].

These water masses possess unique physical and chemical properties, which can be derived from vertical sections in the Labrador Sea [142].

Following the convection period, the upper portion of the central Labrador Sea starts to stratify as the heat and moisture fluxes generate buoyancy during the warmer part of the year [122]. The vertical transport of heat and salt is now restricted to the upper layer, and hence, variations in the LSW at intermediate depths during this period are related to the lateral exchange of heat and salt with surrounding water masses [122]. The gyre circulation in the upper layer is also reduced during this season, and thus permits the lateral exchange of water masses with boundary currents in the upper layer, including the influx of heat and salt from the Irminger Current. These lateral heat and buoyancy fluxes result in the restratification of the interior Labrador Sea [122].

In addition to the influence of atmospheric forcing on the seasonal variability in the strength of deep convection and restratification, the LSW formation is also susceptible to the freshwater supply from the margins, including an influx of Arctic waters and continental run-off [93], as well as transport by offshore eddies [55, 54].

1.2.1.2 Interannual Variability and its connection to the North Atlantic Oscillation

As described in the previous section, the variability of the convective activity and other physical characteristics in the upper Labrador Sea is strongly linked with the atmospheric variability. Over interannual to quasi-decadal timescales, the atmospheric variability in the Northern Hemisphere is dominated by the North Atlantic Oscillation (NAO) [45]. Previous studies suggest a close connection between the NAO and

the variability of circulation and deep convection in the Labrador Sea [142].

The winds blowing over the North Atlantic sector are predominantly Westerlies, which exist quasi-permanently due to the high- and low-pressure systems over the Azores and Iceland, respectively [45]. The anomaly of sea level pressure difference between these two locations is used as a measure of the NAO. This so-called NAO index, is widely used to quantify the characteristics of the longer-term (greater than a year) climatic variability over the North Atlantic Ocean. The NAO index is a measure indicative of the position of the jet stream and extra-tropical storm tracks across the North Atlantic; whether they tend to move to the north or south of the climatological position of the jet streams. The positive NAO index (NAO^+) refers to cold and dry weather in the northern North Atlantic, intensified storminess, and intense surface cooling over the Labrador Sea. The negative NAO index (NAO^-) is associated with opposite variability [46].

On interannual timescales, the impact of NAO on the Labrador Sea variability is associated with variations in the surface heat flux, which then influence the strength of deep convection and LSW formation [21, 67]. For instance, the continuous NAO^+ years during 1990-1994 (Figure 1.5) correspond to the period of the coldest and deepest (> 2000 m [62]) LSW observed in the past 50 years [102, 142]. The rate of LSW formation was between 5-11 Sv during this period [102].

The NAO^- years prevailed from 1958 to 1971, where the NAO index was all negative except for year 1967 (Figure 1.5). The LSW and the entire central Labrador Sea was warmer and saltier due to the mild winters of these predominantly NAO^- years [142]. Such an environment prevented the exchange of heat and salt between the upper and deeper layers. Consequently, LSW had become even warmer and

saltier due to lateral exchange with the surrounding intermediate waters [142]. The mean formation rate of LSW was about 2-4 Sv during this period [142], much weaker than the formation rate during the positive phase [102] mentioned previously. The situation ended with the arrival of a severe winter in 1972 and 1973 [142], which corresponds to a quasi-decadal shift in the NAO index.

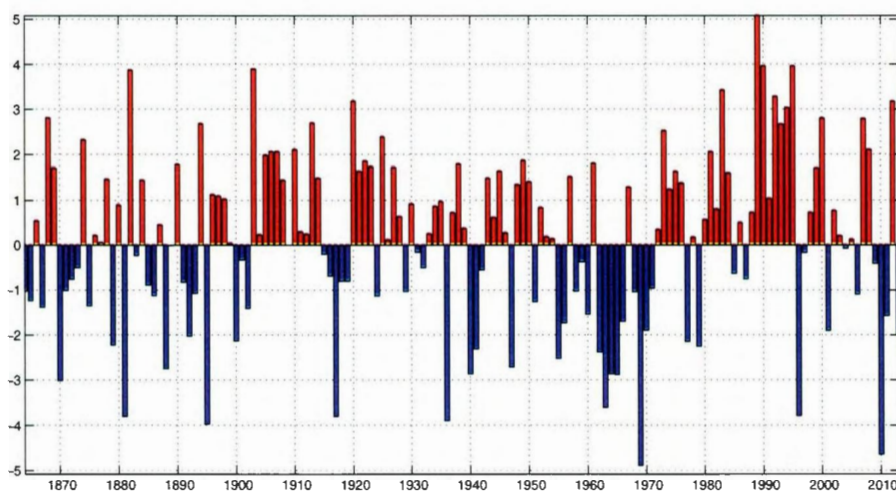


Figure 1.5: The North Atlantic Oscillation index. Data provided by the Climate Analysis Section, NCAR, Boulder, USA, Hurrell (1995). Updated regularly. Accessed 20 July 2013.

1.2.2 Biogeochemical Characteristics

Recent observational studies on atmosphere-ocean carbon fluxes have revealed the subpolar North Atlantic to be a strong sink for atmospheric CO_2 . *Takahashi et al* (2009) estimated this net CO_2 sink to be 0.2-0.5 Gt/yr for 1990, based on the ocean

surface $p\text{CO}_2$ measurements for the time period of 1972-1992 [127]. This influx is a combination of a substantial natural sink and approximately doubled uptake of anthropogenic CO_2 [41]. The subpolar North Atlantic is one of the most intense anthropogenic CO_2 sinks per unit area of the world ocean [81]. Areas of strongest CO_2 uptake coincide with the water mass formation regions of the NADW [127], and hence indicate high inventories of anthropogenic CO_2 in the Labrador Sea.

During winter, convective mixing enhances the CO_2 solubility at the sea surface, promoting transport of atmospheric CO_2 into the deeper layer on short time scales, where some of which may be stored for decades to hundreds of years until they travel across the deep Atlantic Ocean latitudinally and are brought back into the atmosphere. Observations estimate that the Labrador Sea accounts for 8 - 19 % of the global deep carbon sequestration, where the range is primarily subject to the strength of winter deep convection [125]. Thus, deep convection in the Labrador Sea plays an important role in sustaining a vertical transport of carbon dioxide and other atmospheric gases such as oxygen and the chlorofluorocarbons (CFCs), from the surface to the deeper oceans [62], where the convected LSW is ventilated at intermediate depths through the lateral exchange with the surrounding water masses [60, 96].

Figure 1.6 shows the seasonal-mean climatological distribution of surface chlorophyll-a in the Labrador Sea. The timing of the phytoplankton bloom differs region to region within the Sea, starting from early April to mid-July [114]. The first bloom takes place near the coastal regions in early spring (Figure 1.6b). The magnitude of this so-called early spring bloom is greater in the eastern Labrador Sea (off the Greenland coast) than the western Labrador Sea (off the Labrador coast). The driving mechanism for this bloom is the combination of offshore advection, runoff, and eddies

associated with the West Greenland and Irminger Currents [58], which intensify both surface stratification and nutrient supply in the coastal region [32]. In the central part of the Sea, the phytoplankton growth starts later in June upon the thermal stratification over the deep convection area [32] (Figure 1.6c). High nutrient concentrations due to wintertime enhanced vertical mixing triggers high biological productivity in this region that peaks in June/July [133, 123]. In fall, a weak bloom appears on the Labrador coast (Figure 1.6d).

1.2.2.1 Seasonal Cycle

The seasonal variability of surface ocean $p\text{CO}_2$ in the Labrador Sea is triggered by intense vertical mixing during winter and phytoplankton blooms during spring/summer. Physical and biological forcings enhance the solubility and biological pumps respectively, and maintain the $p\text{CO}_2$ of surface water undersaturated almost all year round [17]. Both observations and models suggest that the surface $p\text{CO}_2$ concentration over the deep convection site is maximum in winter and minimum in summer [58]. The winter maximum is associated with the counteractive effect of deep convection [17]; In spite of increased solubility due to surface cooling and wind effect, intense mixing ventilates the vertical column, allowing respiratory CO_2 in the ocean interior to enter the surface layer, and hence raising its $p\text{CO}_2$ level to near atmospheric equilibrium. The summertime $p\text{CO}_2$ minimum coincides with the season of highly-active primary production and subsequent biogenic export.

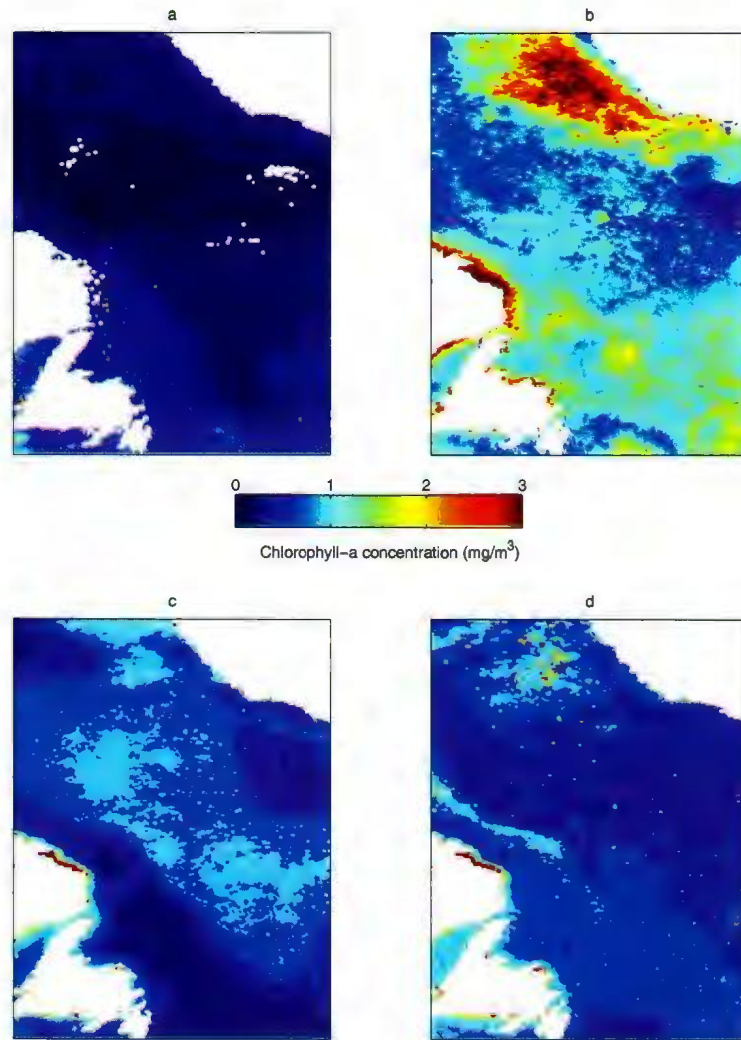


Figure 1.6: Seasonal-mean surface chlorophyll-a concentration in the Labrador Sea during a) winter, b) spring, c) summer, and d) fall.

Source: <http://oceandata.sci.gsfc.nasa.gov/SeaWiFS/Mapped/>

1.2.2.2 Interannual Variability

Observations in the last few decades suggest a considerable decline of the ocean CO₂ uptake in the subpolar North Atlantic. The uptake rate over the southeastern part of the gyre has declined by approximately 50 %, from -0.20 GtC/yr in the mid-1990s to -0.09 GtC/yr in the mid-2000s [111]. Other observational studies further explain that the decline is associated with a rise in the surface ocean pCO₂ during both in summer and winter. A summertime oceanic pCO₂ increase across the subpolar region during 1982-1998 was estimated to be between 2.3 and 3.5 μatm/yr, while the atmospheric pCO₂ increase for the same time period was only 1.5 μatm/yr [63]. The increase in winter was reported to be even greater, ranging from 5.8±1.1μatm/yr to 7.2±1.3μatm/yr for the time period 2001-2008 [78].

Model studies, however, do not support such weakening of the subpolar carbon sink. Rather, both an atmospheric inversion model [105] and a regional coupled physical-biogeochemical model [135] studies have shown a decadal increase of 0.03 GtC/yr and 0.04 GtC/yr over the same time period and same region, respectively. Comparison of the observational and model studies is difficult because of their lack of coherence in time and space [112]. Therefore, identifying the mechanisms for both of the observed and simulated changes is essential to distinguish the decadal variability from longer-term trends.

Several papers have attempted to connect the decadal pCO₂ variability with NAO. *Corbiere et al.* (2007) attributed a positive-to-negative NAO phase shift during the mid-1990s and the mid-2000s to the increased pCO₂ in the subpolar gyre, primarily caused by warmer surface waters in this region [13]. Additionally, reduced gyre

circulation in the 1990s increased advective inflow of subtropical waters, and hence weakened the CO₂ uptake in the subpolar gyre [113]. On the contrary, *Ullman et al.* (2009) demonstrated that the decline in NAO led to reduced penetration of high DIC from depths, which resulted in decreased pCO₂ at the surface and thus promoted the atmospheric carbon uptake [135].

However, it should be noted that the NAO only accounts for about 30 % of climate variability over the North Atlantic Ocean [71]. Therefore, additional factors may drive the carbon sink variability. For instance, *Metzl et al.* (2010) argues that the increase of surface ocean pCO₂ in the early 2000s was due to seawater carbonate chemistry changes, and not NAO variability [78]. Undoubtedly, the fact that the carbon sink is influenced by a combination of various and vigorous mechanisms makes a precise determination difficult, especially as they vary on interannual to decadal timescales, that are subject to both observational and model uncertainty [112].

1.3 Objectives

Given the critical role of the subpolar North Atlantic in the global carbon cycle, determining the mechanisms that control the variability of the carbon sink over this region is a fundamental step in quantifying the oceanic response to increasing anthropogenic carbon emissions. Furthermore, to the best of the author's knowledge, no ocean carbon studies using 3-D eddy-resolving coupled physical-biogeochemical ocean models have yet been published for the Labrador Sea. Thus, the present study takes the initiative towards the development of such a model for this region.

Using the coupled physical-biogeochemical ocean model in 1-D offline mode, the present thesis attempts to:

1. examine the performance of the model implemented for three distinct locations in the Labrador Sea.
2. analyze the structure of seasonal variability of the ecosystem and carbon dynamics and their relations to coupled physical-biogeochemical processes.

1.4 Organization

The rest of the thesis is organized as follows: the model and the methodology of the experiments are described in Chapter 2. Results from the model experiments and sensitivity analysis are presented for validation in Chapter 3. Simulated physical and biogeochemical variability and carbon cycle in the Labrador Sea are discussed in Chapter 4. The conclusions of the thesis are provided in Chapter 5, followed by the suggestions for future work in Chapter 6.

Chapter 2

Methods

This chapter describes the coupled physical-biogeochemical model used in the present study, and its implementation to the three monitoring stations in the Labrador Sea.

2.1 Coupled Physical-Biogeochemical Ocean Model

Coupled physical-biogeochemical ocean general circulation models are an essential tool for describing ocean carbon dynamics, analyzing the effects of various interdisciplinary processes, and interpreting observational findings [23]. The present study employed the NEMO (Nucleus for European Modelling of the Ocean) system, which is a state-of-the-art modeling framework for oceanographic research, operational oceanography, seasonal forecast, and climate studies (NEMO website: <http://www.nemo-ocean.eu/>). The coupled system used for the present study is called OPA-PISCES, where OPA is the physical component and PISCES is the biogeochemical component of the NEMO system [69].

2.1.1 Physical Model

Description

The physical component of NEMO is OPA, a primitive equation ocean circulation model [69], which was implemented for the Labrador Sea basin based on a two-way nesting of the North Atlantic model [146]. The model domain covers the Labrador Sea and the Northwest Atlantic basin between 36°W and 78°W , and between 32°N and 64°N . The horizontal resolution of the model is $1/12^{\circ}$ in longitude and $1/12^{\circ} \times \cos \phi$ in latitude where ϕ is the latitude, enabling each grid cell to be approximately square. Thus, the horizontal resolution is eddy resolving across the entire domain. There are 46 vertical levels using z partial steps, with 13 levels in the top 100 m. The model is coupled to the Louvain-la-neuve Ice Model 2 [30], the sea-ice component of NEMO. The numerical scheme used in the model was the finite volume method on an Arakawa C-grid. The radiative open boundary conditions were defined for the North Atlantic model at the northern and southern boundaries using the SODA data [10]. The model was initialized with climatological temperature and salinity fields derived from the World Ocean Atlas 2005 (WOA05) dataset [2, 66], and run for 30 years with climatological atmospheric forcing. After this spin-up phase, the model was run using 6-hourly NCEP/NCAR reanalysis [51] as atmospheric forcing. The time step of the model simulation was 1800 seconds. The vertical mixing was parameterized by the 1.5 turbulent closure model [34]. Throughout the simulation period, a spectral nudging scheme was applied to reduce model bias [132].

Governing Equations

The governing equations of OPA include the incompressible, Boussinesq, hydrostatic, thin-shell primitive equations, the thermodynamic equations of heat and salt, and the equation of state for seawater:

$$\frac{\partial U_h}{\partial t} = -((\nabla \times U) \times U + \frac{1}{2} \nabla U^2)_h - f \hat{k} \times U_h - \frac{1}{\rho_0} \nabla_h p + D^U + F^U \quad (2.1)$$

$$\frac{\partial p}{\partial z} = -\rho g \quad (2.2)$$

$$\nabla \cdot U = 0 \quad (2.3)$$

$$\frac{\partial T}{\partial t} = -\nabla \cdot (TU) + D^T + F^T \quad (2.4)$$

$$\frac{\partial S}{\partial t} = -\nabla \cdot (SU) + D^S + F^S \quad (2.5)$$

$$\rho = \rho(T, S, p) \quad (2.6)$$

Here, U is the velocity field such that $U = U_h + w\hat{k}$ where $U_h = \langle u, v \rangle$ denotes the horizontal (\hat{i}, \hat{j}) component of U orthogonal to \hat{k} , the local upward vector to the earth, and w is the vertical component of U . z is the vertical coordinate, f is the Coriolis acceleration, ρ is the in-situ density, ρ_0 is the reference density, p is the pressure, g is the gravitational acceleration, T is the potential temperature, and S is the practical salinity. D^i and F^i for $i = U, T, S$ denote the parameterizations of sub-grid scale physics and the surface forcing terms, respectively.

The kinematic boundary conditions at sea surface and bottom are defined as follows:

$$w = \frac{\partial \eta}{\partial t} = u \frac{\partial \eta}{\partial x} + v \frac{\partial \eta}{\partial y}, \text{ at } z = 0 \quad (2.7)$$

$$w = u \frac{\partial H}{\partial x} + v \frac{\partial H}{\partial y}, \text{ at } z = H \quad (2.8)$$

where η denotes the height of sea surface from a reference surface ($z = 0$) and H is the depth of the sea floor from the reference surface. Additionally, no normal flow is assumed at the lateral boundaries:

$$(U_h \cdot \hat{n}) = 0, \quad (2.9)$$

where \hat{n} is the normal vector to a solid boundary. The dynamic boundary conditions at the surface are given by:

$$K \frac{\partial u}{\partial z} = \frac{\tau_x}{\rho_0}, \text{ at } z = 0 \quad (2.10)$$

$$K \frac{\partial v}{\partial z} = \frac{\tau_y}{\rho_0}, \text{ at } z = 0 \quad (2.11)$$

where K is the surface vertical eddy diffusivity, τ_x and τ_y are the surface wind stress components.

2.1.2 Biogeochemical Model

PISCES (Pelagic Interaction Scheme for Carbon and Ecosystem Studies) [6] is an intermediate complexity ocean biogeochemical model which simulates low trophic level ecosystem dynamics, as well as carbon and oxygen cycles. The development of the model started in 1997 with the release of the P3ZD model, a classical nitrogen-phytoplankton-zooplankton-detritus (NPZD) model with semi-labile dissolved organic matter (DOM) [5]. After numerous improvements, a stable version of the model was released in 2004, which has become freely available to NEMO users. The full description of the latest version of the model (version 2) is currently in preparation, and will be available on the NEMO website some time next year [7]. PISCES is used in a variety of model studies by oceanographers and climate scientists, including its

contribution to the Fifth Assessment Report (AR5) of the Intergovernmental Panel on Climate Change [124].

There are twenty-four state variables in PISCES (see Figure 2.1 and Table A.1): there are five limiting nutrients (nitrate, ammonium, phosphate, iron, and silicate), four living compartments (two phytoplankton classes: nanophytoplankton and diatoms; and two zooplankton classes: microzooplankton and mesozooplankton), and three non-living compartments (semi-labile dissolved organic matter, small and big sinking particles). In addition to the low trophic level ecosystem model, PISCES also simulates dissolved inorganic carbon, total alkalinity, and dissolved oxygen. The latter tracer is also used to distinguish between oxic and anoxic environments for remineralization process.

PISCES differs from many of the previously-developed Monod models [83] mainly in two aspects. First, phytoplankton growth rates are limited by multiple nutrients: three (Fe, PO₄, NO₃+NH₄) for nanophytoplankton and four (Fe, PO₄, NO₃+NH₄, Si) for diatoms. Previous studies have justified the importance of iron and silicate in limiting phytoplankton growths even at high latitudes, such as in the Iceland basin [88] and in the central Labrador basin [43], respectively.

Secondly, the elemental ratios of Chl, Fe, and Si for the composition of both phytoplankton classes are not fixed by Redfield ratios. Assuming a constant stoichiometry of these elements to carbon is not preferable as these ratios can vary considerably. For example, the Fe/C ratio can vary by at least an order of magnitude when the N/C ratio varies by a factor of two. Thus, these ratios are prognostically predicted in PISCES based on the external concentrations of limiting nutrients as in the quota models [75, 25], which is the other big family of marine biogeochemical model (as

oppose to the Monod-type models). Therefore, the model is capable of simulating phytoplankton of different physiological compositions in terms of Chl/C, Fe/C, and Si/C ratios. On the other hand, the phytoplankton growth rates also depend on these external concentrations of limiting nutrients, assuming a fixed constant Redfield ratio of Fe/P/N/C for nanophytoplankton (or Fe/Si/PO₄/N/C in the case of diatoms). Therefore, PISCES takes a compromise between Monod and quota approaches.

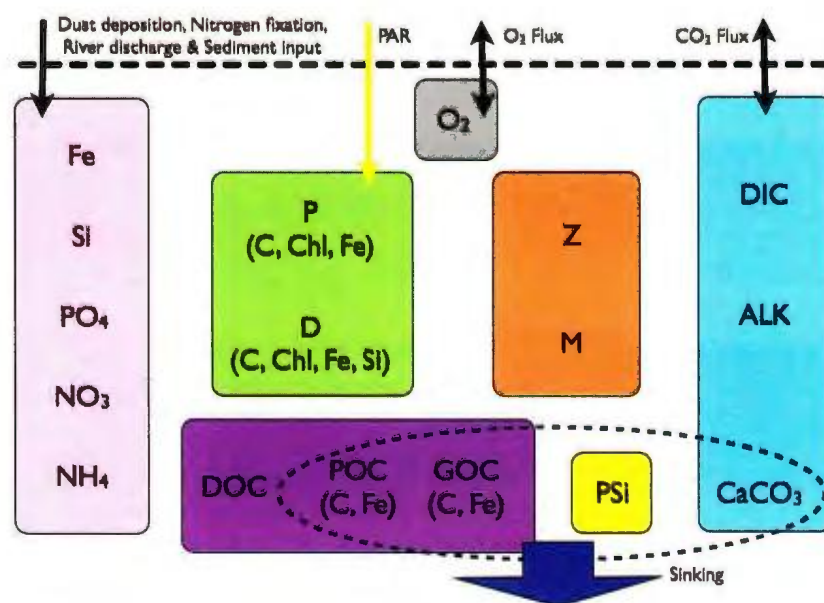


Figure 2.1: Schematic diagram of PISCES

The temporal evolution of biogeochemical tracers can be driven by chemical biological processes and/or by advection and turbulent mixing [29]. The general form of the tracer conservation equation is:

$$\frac{\partial c}{\partial t} = -\vec{V} \cdot \nabla c + \nabla \cdot (D \cdot \nabla c) + SMS(c) \quad (2.12)$$

where c is the concentration of the model state variable of interest, t is the time,

\vec{V} is the velocity field of the ocean current, D is the eddy diffusivity, and SMS stands for source-minus-sink, which describes the chemical biological processes for the considered state variable. The SMS equations of PISCES state variables are described in Appendix A.

2.2 Experimental Design

2.2.1 Studied Regions

Since 1990, the Labrador Sea Monitoring group from the Bedford Institution of Oceanography (BIO) has been carrying out an annual hydrographic expedition across the Labrador Sea (Figure 1.4). This line, referred as the Atlantic Repeat Hydrography Line 7 West (AR7W), consists of 28 sampling stations at which temperature, salinity, dissolved oxygen, inorganic carbon, alkalinity, and nutrients are measured. Three stations, numbered 8, 15, and 25, are selected as points of interest for the present study, that are representative of the Labrador coast, the central Labrador basin, and the Greenland coast, respectively. Subsequently, both physical and biogeochemical processes at these stations are expected to be distinct from one another as described in Section 1.2 of Chapter 1.

2.2.2 Data for Model Validation and Initialization

BioChem Database

The data used in this study are obtained from the BIO's BioChem database [20, 40], which includes the dataset collected at the three stations during four cruises that took

place in 1990, 1992, 1993, 1994, and 1995. These years correspond to the positive NAO period in the early 1990s. No data is available for the three stations during 1991. Each dataset consists of temperature, salinity, pressure, oxygen, nitrate, ammonium, phosphate, and DIC that are measured at various depths. In order to match the units for measured DIC with the model, the density was computed for a set of measured temperature, salinity, and pressure using the *GSW Oceanographic Toolbox* [77], which was then used to convert the units for measured DIC from $\mu\text{mol}/\text{kg}$ to the model units of $\mu\text{mol}/\text{L}$.

SeaWiFS Climatology

The concentration of phytoplankton can be estimated from satellite measurements of sea surface color. Chlorophyll-a is a specific form of pigment that is essential for most phytoplankton groups to photosynthesize, and therefore has been used as a proxy for primary productivity for many decades (e.g. *Ryther and Yentsch (1957)* [106]). In the present study, the chlorophyll data is obtained from the Sea-viewing Wide Field-of-view Sensor (SeaWiFS) [76, 143], which consists of weekly composites of surface chlorophyll-a concentration from 1997 to 2009.

2.2.3 Model Implementation

The coupled OPA-PISCES model is implemented in the Labrador Sea using the one-dimensional vertical configuration [26], in which the model equations are computed at every vertical level over a specified grid point of interest. The 1-D vertical configuration only considers the vertical coordinate and time as independent variables in the model equations in which all the horizontal derivatives are set to zero. Thus,

neither advection nor lateral mixing are incorporated in this configuration, leading to constant vertical velocity fields of zero (i.e. $w = 0$) since it is zero at the surface. Accordingly, the advection-diffusion equation for the PISCES tracers (Equation 2.12) is simplified as:

$$\frac{\partial c}{\partial t} = \frac{\partial}{\partial z} \left(K \frac{\partial c}{\partial z} \right) + SMS(c) \quad (2.13)$$

where K is the vertical eddy diffusivity and the rest of the terms have been described previously.

Three model simulations at Stations 8, 15, and 25 were performed for one year in *offline* mode, which means that the PISCES tracer equations are solved using the previously-computed ocean dynamics of OPA, as opposed to *online* mode, in which the physical and biogeochemical models are computed simultaneously. The ocean dynamics used in the present study consists of eight physical variables (temperature, salinity, turbocline depth, shortwave radiation, surface concentration/dilution water flux, sea-ice coverage, vertical eddy diffusivity, and atmospheric wind at 10 m above sea surface), which are the daily-mean product of the model simulation for year 1994, which are interpolated to the temporal resolution of the model (1 hour). The temporal resolution of 1 day for the ocean dynamics was chosen as a compromise between the need of representation of most important scales of upper ocean variability in this study and the requirement for computational resources and disk storage. One question which can be studied in the future when more computational resources will be available is, how significant is the contribution of daily cycle of physical processes (e.g. temperature and diffusion coefficients) on the results from model simulations.

The biogeochemical tracers are initialized with the climatological values from

GLODAP (for DIC and alkalinity) [107] and World Ocean Atlas 2001 (for oxygen, phosphate, nitrate, silicate, DOC, and iron) [65, 12] Figure 2.2 shows the vertical profiles of these variables at the beginning of model integration. The boundary conditions of nutrients included the climatological monthly-mean dust deposition [130] and the climatological annual-mean river discharge [68]. The atmospheric $p\text{CO}_2$ is set to a fixed value ($360 \mu\text{atm}$) throughout the simulated period, which is close to the recorded annual-mean value for 1994 [52].

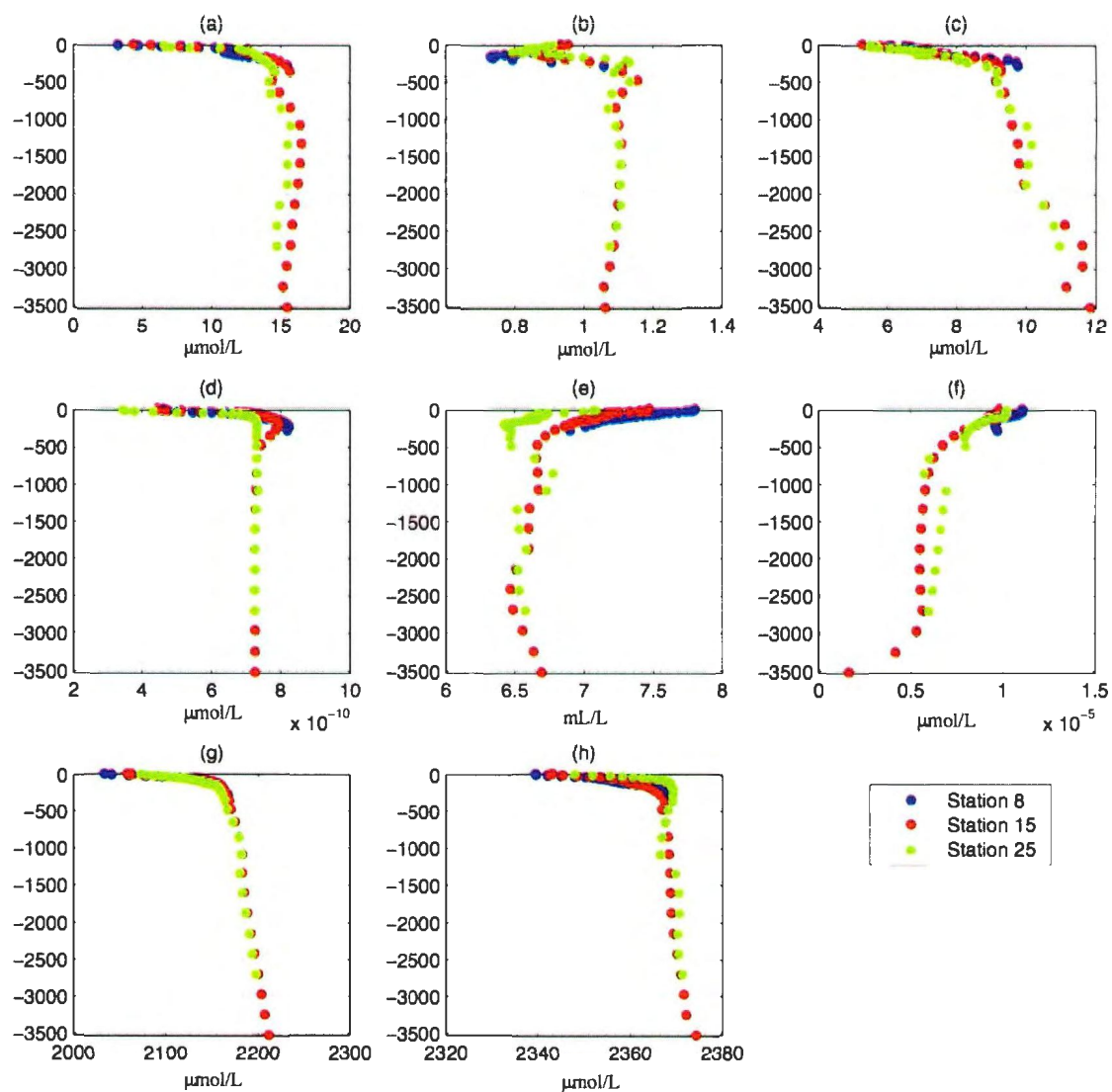


Figure 2.2: Initial data for a) nitrate, b) phosphate, c) silicate, d) iron, e) oxygen, f) dissolved organic carbon, g) dissolved inorganic carbon, and h) total alkalinity

Chapter 3

Model Validation and Sensitivity to Parameter Variations

To the best of author's knowledge, biogeochemical model simulations of the Labrador Sea based on PISCES has not been done previously. Therefore, the first step in the model implementation is validation of the model and study of sensitivity to model parameters.

3.1 Model-Data Comparison

To evaluate the model performance, results are compared to the 1990-1995 BioChem data [20, 40] and the 1999-2005 SeaWiFS climatology [76, 143].

3.1.1 Vertical Structures of Physical and Biogeochemical Tracers

Simulated and observed vertical distributions of temperature, salinity, oxygen, nutrients, and DIC at Station 8 are shown in Figure 3.1. The model output is averaged over the month of June to compare with the field data which were collected around June in 1990 and 1992-1995 (see Fig. 3.1 for the actual data collection date). The horizontal bars on the simulated profiles indicate the range of daily-mean variability at each model depth for June. The observed structure of the temperature gradient with depth is depicted by the model in which the coldest waters are found in the top 50 m (Figure 3.1(a)). The simulated temperature profile fits well with the data above 25 m and below 150 m but not in between. In particular, the model does not reproduce the magnitude of the minimum in the subsurface cold layer between 25 and 50 m depth. The fresh and cold waters in this layer are strongly influenced by the discharge from the rivers and estuaries in the region that are not considered in the model with this resolution. This indicates the model's deficiency in resolving the temperature gradient in the subsurface euphotic zone in this coastal region. In general, the model is able to reasonably reproduce the in-situ vertical structures of salinity, oxygen, and nutrients (nitrate, ammonium, and phosphate) (Figure 3.1c-f). One feature missing in the model results is the representation of oxygen saturation and nutrient depletion in the near surface that are driven by the diurnal cycle of primary production. This deficiency arises from the fact that the model does not resolve the diurnal cycle of Photosynthetically Available Radiation (PAR). Instead, the daily average of PAR is computed at every time step in the model, which resulted in the

relatively uniform distributions of nutrients in the euphotic zone especially above 25 m (Figure 3.1c-f). Nevertheless, the mean depth-variations of nutrients compare well with the observations. The largest difference between the simulations and data occurs in the DIC profile. Except in the top 20 m, the DIC concentration is underestimated by the model at all depths (Figure 3.1g).

Similarly, the model-data comparison is done for the central Labrador Sea (Figure 3.2). The vertical profiles between the simulation and the measured data are in good agreement except for temperature in the deep ocean (below 2300 m) where the model underestimates the measured profile, nitrogen in the intermediate layer (between 250 and 1750 m), and DIC below the sun-lit layer, in which the simulation underestimates all of these observed values (Figure 3.2a,d,g). Furthermore, a big difference between the model and data appears in the representation of the depth at which the oxygen concentration is dropped substantially in the intermediate ocean (Figure 3.2c): a rapid decrease (of approximately $20 \mu\text{mol/L}$) of oxygen is observed at about 2250 m depth, whereas the model reproduces the similar feature at 1750 m depth, thus creating a 500 m difference between the model and the data. This difference may arise from the difference in the position of the water masses, which may be attributed to the influence of the vertical resolution of the model and uncertainties due to unresolved processes of vertical mixing in deep ocean.

Figure 3.3 presents the model validation in the eastern Labrador Sea (Station 25). The simulated profiles in the top 250 m involve relatively large temporal variations for all tracers (seen as dark shaded regions in Figure 3.3), which overlap with the measured values. Unlike at the other two stations, the model-data misfit of active tracers (temperature and salinity) appears throughout the water column below 500

m, in which the model simulates warmer and saltier waters (Figure 3.3a&b). Despite this fact, the vertical distributions of observed oxygen and nutrients are in general well reproduced by the model (Figure 3.3c-f). On the contrary, the simulated vertical profile of DIC is misrepresented with lower-than-observed values throughout the water column, which appears to be a systematic error of the model.

3.1.2 Seasonal Evolution of Primary Productivity

Simulated and measured seasonal evolutions of surface chlorophyll concentrations are shown in Figure 3.4. The red dots show represent the weekly mean values for 1997-2009 with the associated upper and lower limits of one standard deviation (in red circles). Simulated chlorophyll concentrations in nanophytoplankton and diatoms are averaged weekly to match the temporal resolution of the SeaWiFS data. Here, measured data is assumed to represent the sum of the model phytoplankton groups as the data does not distinguish the two groups. The temporal evolution of simulated (sum of nanophytoplankton and diatoms) and observed chlorophyll show good correlation for the central Labrador Sea basin ($r=0.88$; Figure 3.4b), but not for the coastal regions ($r=0.37$ and $r=0.49$; Figure 3.4a and c, respectively). As mentioned in Section 1.2.2 of Chapter 1, the spatial variability in the magnitude and timing of the phytoplankton blooms is evident from these plots.

Two distinct blooms are depicted both by the model and the data at Station 8 (Figure 3.4a). Climatologically, the early spring bloom takes place in June, followed by a relatively weaker bloom in October, known as the late bloom. Simulated results indicate the occurrence of two blooms; one in May and another one in July, which do

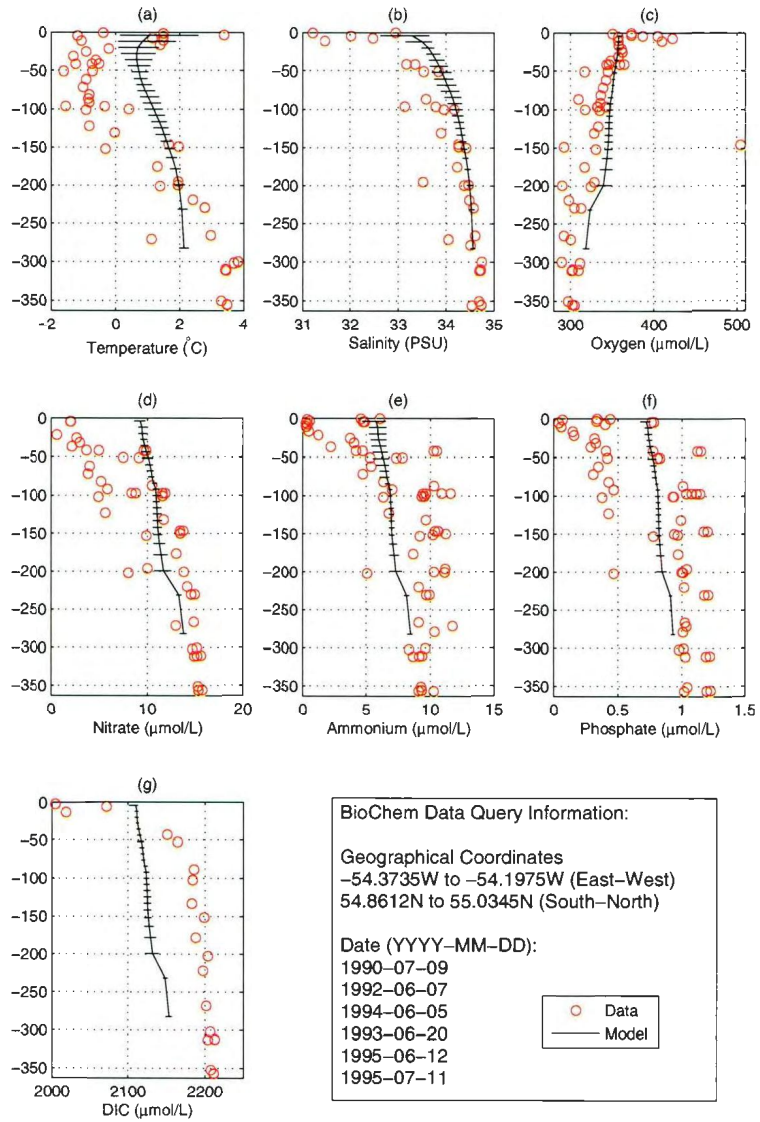


Figure 3.1: Simulated and observed vertical profiles of active and passive tracers at Station 8

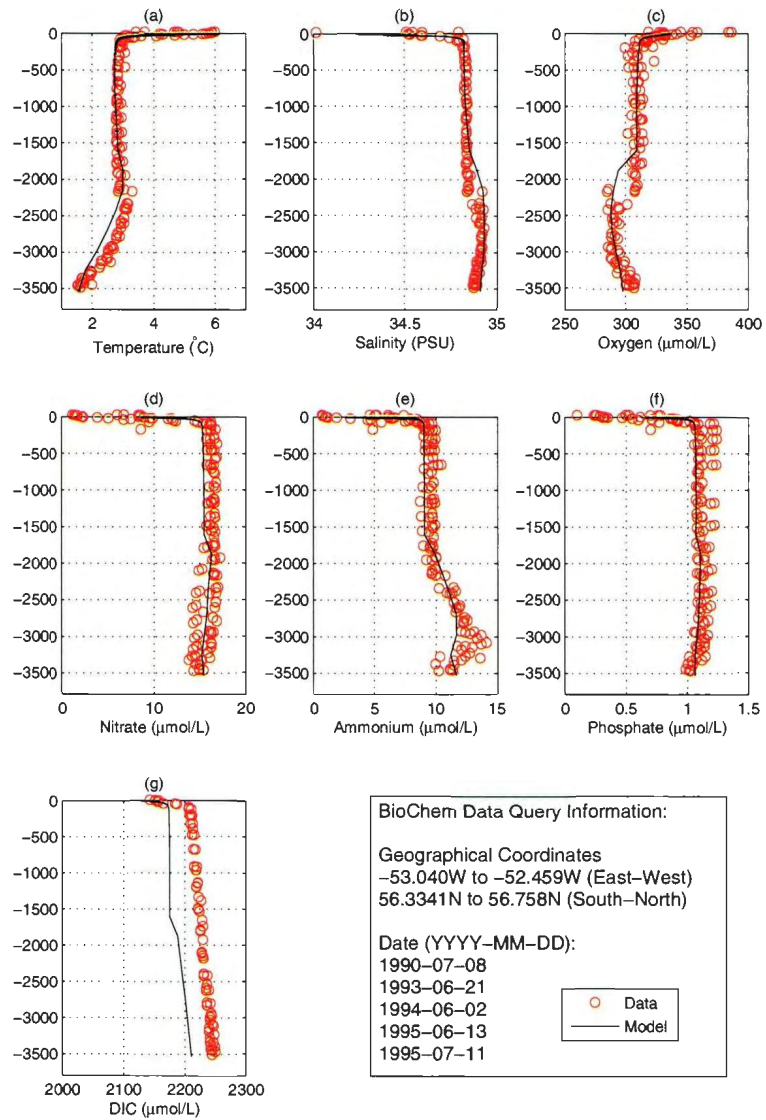


Figure 3.2: Same as Figure 3.1, but at Station 15

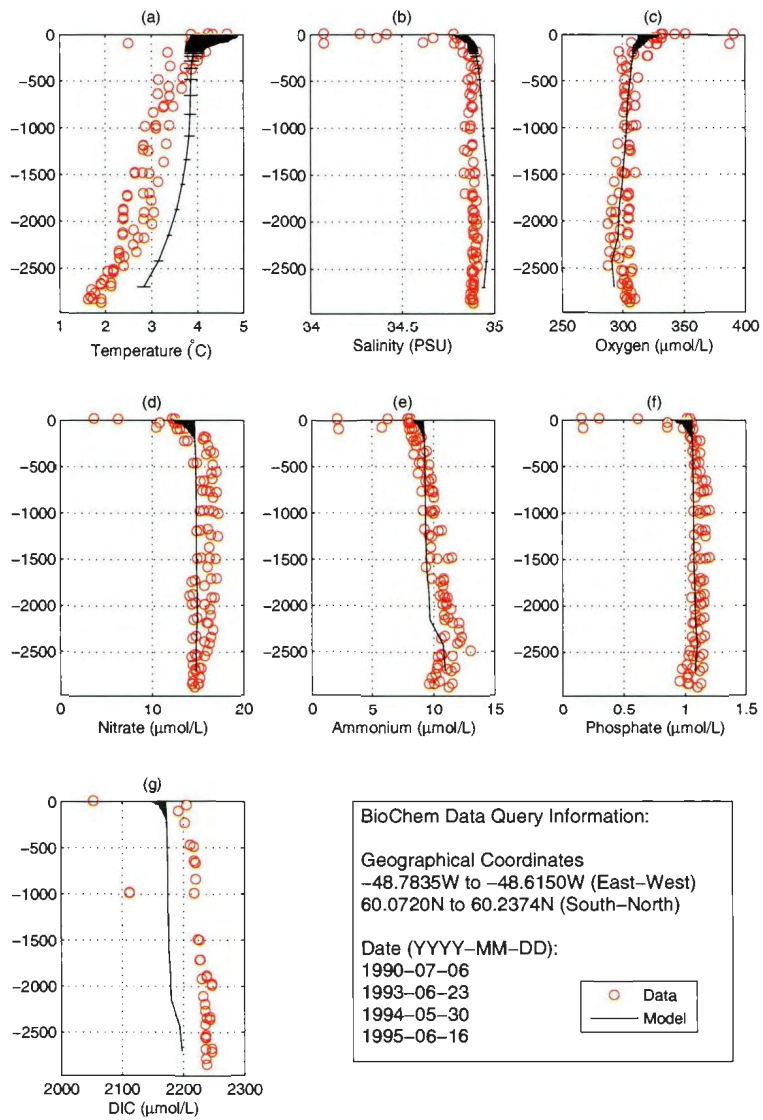


Figure 3.3: Same as Figure 3.1, but at Station 25

not coincide with the observed bloom timings.

In the central Labrador Sea, blooms are not distinguishable from the data (Figure 3.4b). Rather, the surface chlorophyll concentration remains relatively high from mid-May until August. The model reproduces the peak value of about 5 mg/m^3 in late May, matching with the observed timing. Throughout the year, the range of chlorophyll concentrations are within one standard deviation of the climatology, except for the second half of June in which the model exceeded this range.

The seasonal evolution of surface chlorophyll in the eastern Labrador Sea is similar to the western part (Figure 3.4c), which is characterized by the occurrence of two separable blooms; one in May and another one in the beginning of October. The simulated spring bloom, however, was delayed by a month, compared to the climatology. The simulated chlorophyll concentration remained much higher ($> 1.5 \text{ mg/m}^3$) than the observed values ($< 1 \text{ mg/m}^3$) during the summer, as was the case for Station 8 (i.e. Figure 3.4a). This may suggest the influence of other physical and/or biogeochemical processes specific to coastal regions. The signature of the late bloom in October is not clearly present in the model.

3.2 Model Sensitivity to Parameter Variations

The aim of this section is to carry out a series of sensitivity tests to assess which of the model parameters of PISCES have a great impact on the simulated diatoms bloom which was discussed in Section 3.1.2.

A simple method is applied to examine the impact of parameter variations of the input model parameters for the diatoms bloom observed in the end of July (Station

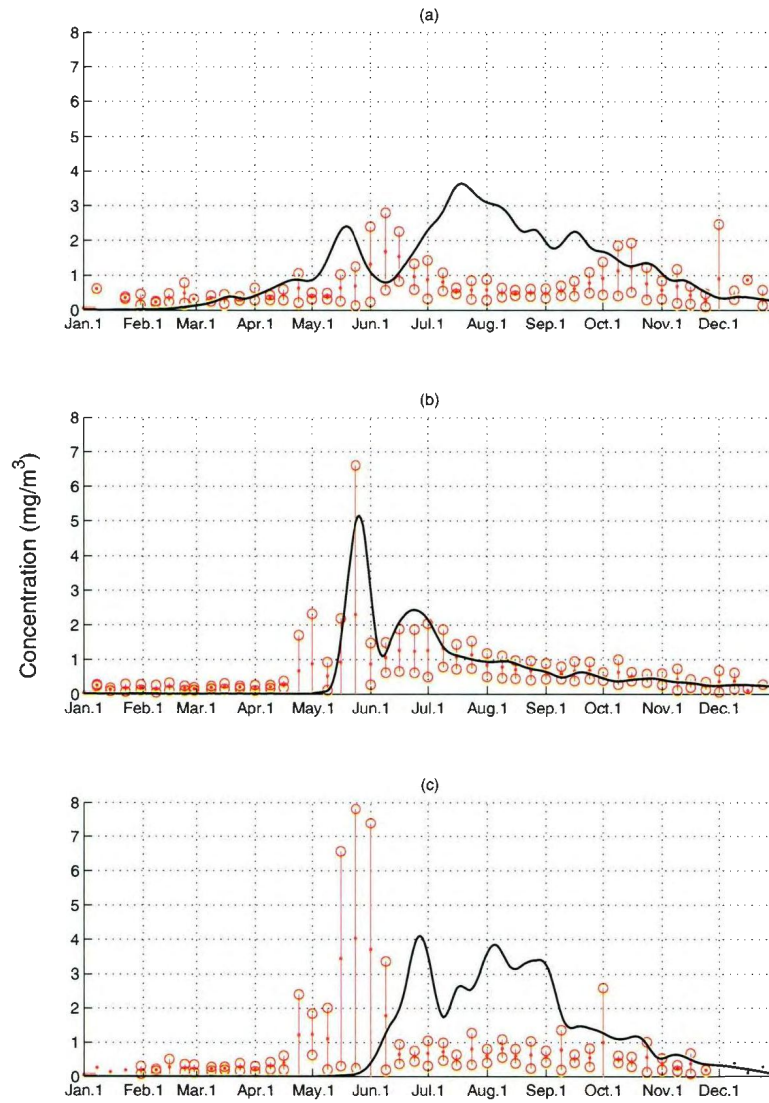


Figure 3.4: Simulated (*black*) and measured (*red*) temporal evolutions of weekly-averaged surface chlorophyll concentration at Station 8 (a), 15 (b), and 25 (c).

8), June (Station 15), and August (Station 25) in the standard runs (see Figure 4.3b, Figure 4.5b, and Figure 4.7b). The input parameters listed in Table A.3 are tunable at the beginning of each model simulation without recompiling the model code. For each parameter, ten simulations are conducted by varying the parameter value of consideration while keeping the values of other parameters unchanged. Starting with 10 % of the standard value (see Table A.3), the value of the considered parameter is increased by 2 % for the succeeding run. Therefore, for each sensitivity experiment, ten model outputs are produced, representing the simulated results with ± 10 % variations from its standard value with an increment of 2 %. Model simulations for sensitivity analysis are performed for 30 days starting from the first day of the month of which the diatoms bloom was observed (July for Station 8, June for Station 15, and August for Station 25; see Figure 3.4b) to compare the the newly-obtained chlorophyll concentrations of diatoms (DCHL) at the end of the simulations (i.e. June 30, July 30, and August 30) with the concentrations obtained from the standard run done with best estimation of model parameters. The sensitivity of the varied parameter value was quantified in terms of the percentage change in DCHL from its standard value, ΔDCHL , as follows:

$$\Delta\text{DCHL} = \frac{\text{DCHL}_{new} - \text{DCHL}_{standard}}{\text{DCHL}_{standard}} \times 100\% \quad (3.1)$$

where DCHL_{new} and $\text{DCHL}_{standard}$ denote the chlorophyll concentration of diatoms on the 30th day of the simulated month based on the sensitivity run and the standard run, respectively.

Figure 3.5 presents the standard deviation of ΔDCHL for each of the 80 tested parameters at Station 8. The difference in the model sensitivity to individual param-

eter variations is evident from the plot; while many parameters have little or almost no impact, others appear to be fairly significant. In particular, the following eight parameters are shown to have a crucial impact on DCHL as their standard deviations exceed 0.02: *conc3m*, *ksi1*, *pislope2*, *chlcdm*, *fecdm*, *whld*, and *grazrat2*. As one would expect, most of these parameters are directly related to determining the functionality of diatoms (*conc3m*, *ksi1*, *pislope2*, *chlcdm*, *fecdm*, *whld*). On the other hand, one parameter, *grazrat2*, influences DCHL indirectly, as it sets the maximum grazing rate of mesozooplankton, the large zooplankton class that prefers to graze on diatoms over nanophytoplankton. Hence, fluctuations in their grazing rate can modify the concentration of diatoms.

Figure 3.6 and Figure 3.7 show the standard deviations of Δ DCHL for the model parameters at Stations 15 and 25, respectively. Similarly to Station 8, top eight parameters of highest standard deviations are considered here to be most influential to DCHL. Variations in the four parameters (*chlcdm*, *conc3m*, *fecdm*, *whld*) are commonly found to be important to DCHL at all stations, all of which have effects on the physiological characteristics of diatoms. By comparing the top eight influential parameters at all three stations, an interesting trend is found. The influential parameters that are unique to Station 8 happen to be all associated with diatoms, including the mean silicon-to-carbon ratio (*grosip*), the slope of photosynthesis-irradiance (PI) curve (*pislope2*), and the half-saturation constant for silicate uptake (*ksi1*) of diatoms. Therefore, the diatoms bloom is more sensitive to changes in the parameters that control the functionality of diatoms alone. The diatoms bloom at Station 15 appears to be sensitive to variations in the parameters that define grazing preference for diatoms (*xpref2d*) and growth efficiency (*epsher*) of microzooplankton, which

suggest an important connection between diatoms and microzooplankton, specific to the central Labrador Sea. Finally, the diatoms bloom at Station 25 appear to be sensitive to the following three parameters which are less influential at the other stations: grazing preference for particulate organic carbon (*xprefc*), half-saturation constant for grazing (*xkgraz2*), and growth efficiency (*epsheer2*) of mesozooplankton. Thus, in the eastern Labrador Sea, the diatoms bloom is more sensitive to variations in the parameters that relates diatoms to mesozooplankton.

Figure 3.8- 3.10 show how the magnitude of diatoms bloom changes from the reference value due to variations in each of the eight influential parameters at the three stations. DCHL responds linearly to variations in the parameters. The range of Δ DCHL is biggest (from -13 to 18 %) at Station 8, and relatively small at Stations 15 and 25 (about $\pm 5\%$), implying spatial dependency of model sensitivity.

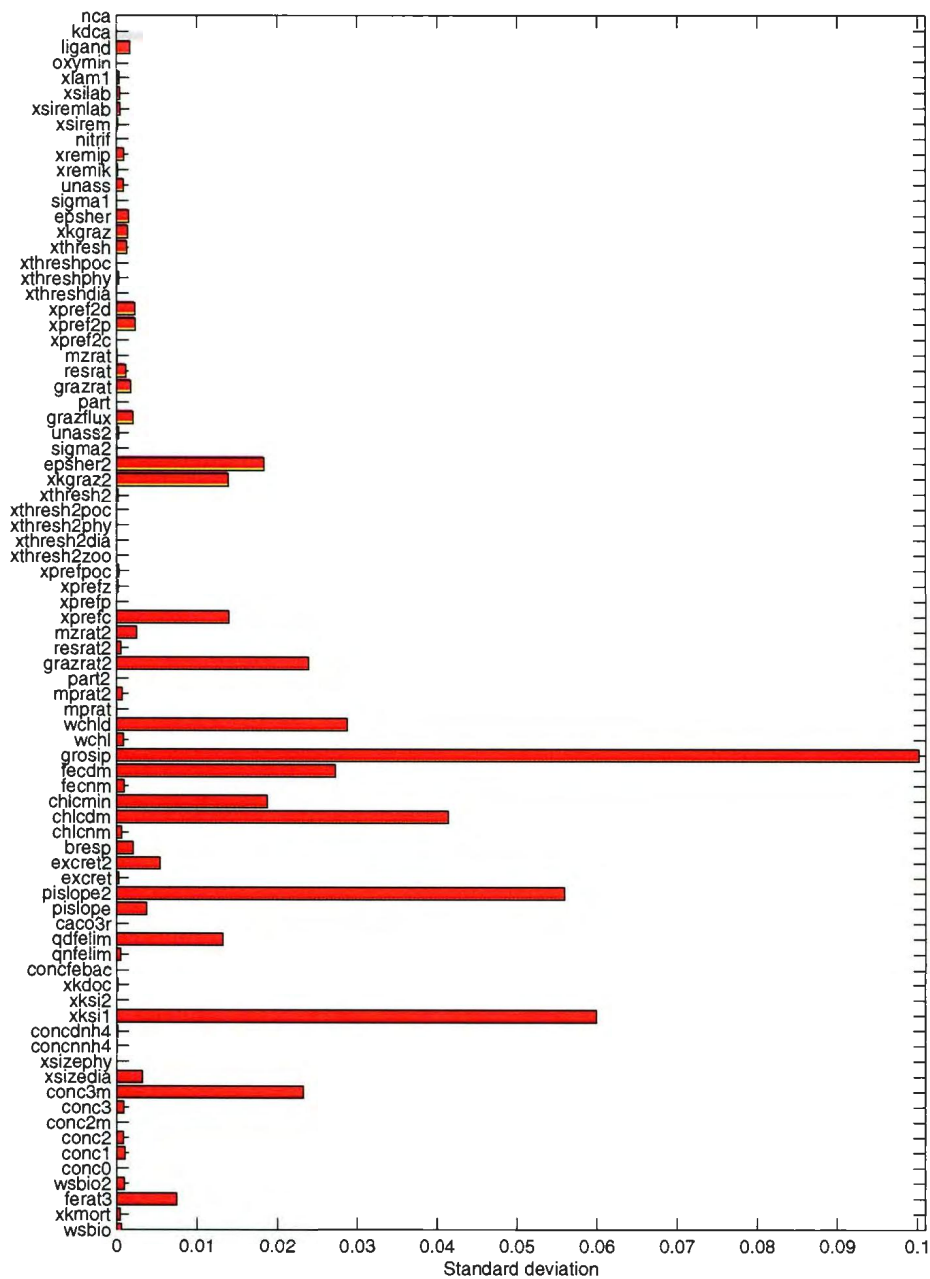


Figure 3.5: Sensitivity of the diatoms bloom to the 80 model parameters at Station 8, quantified as the standard deviation of $\Delta DCHL$.

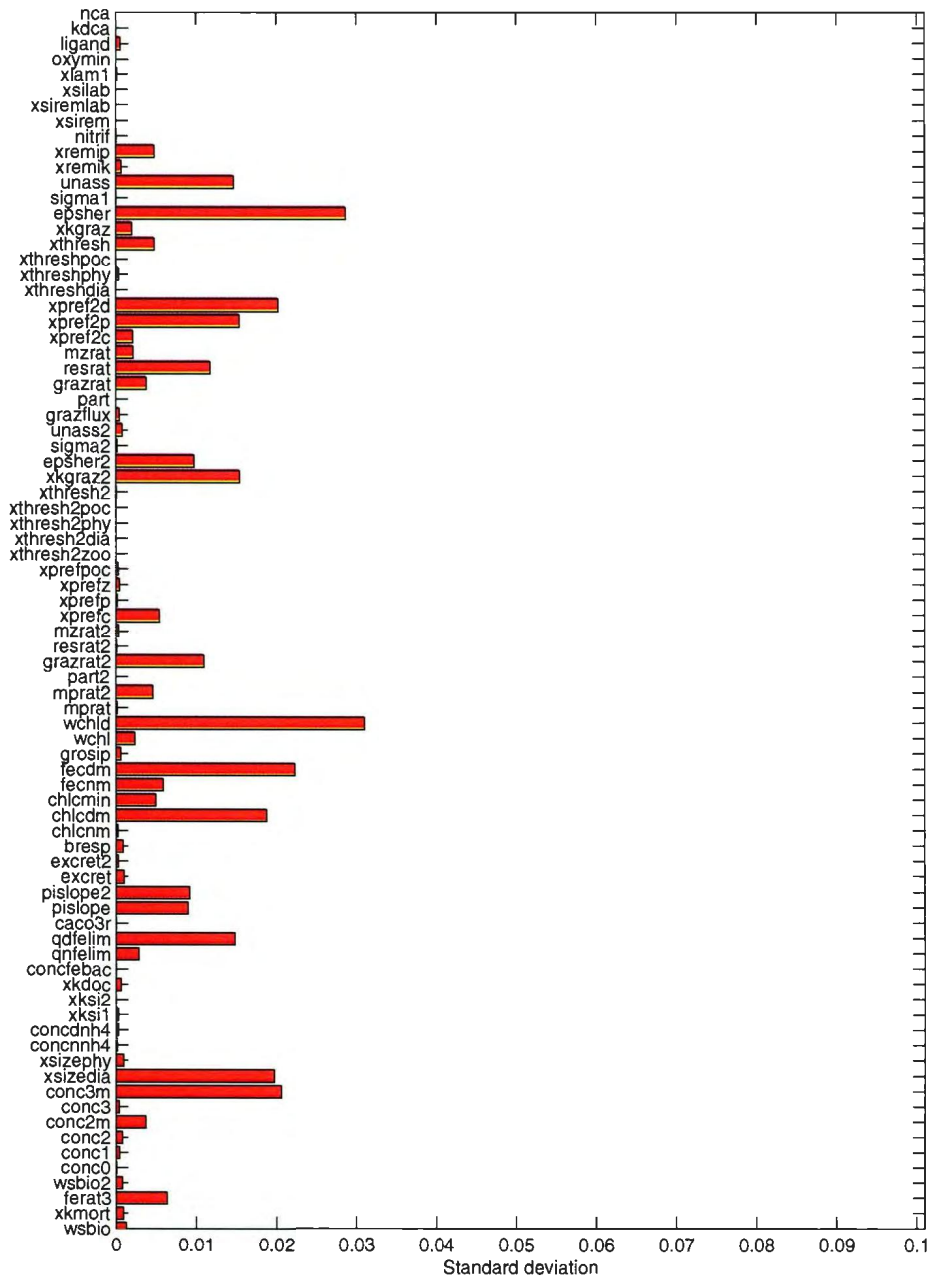


Figure 3.6: Same as Figure 3.5, but for Station 15

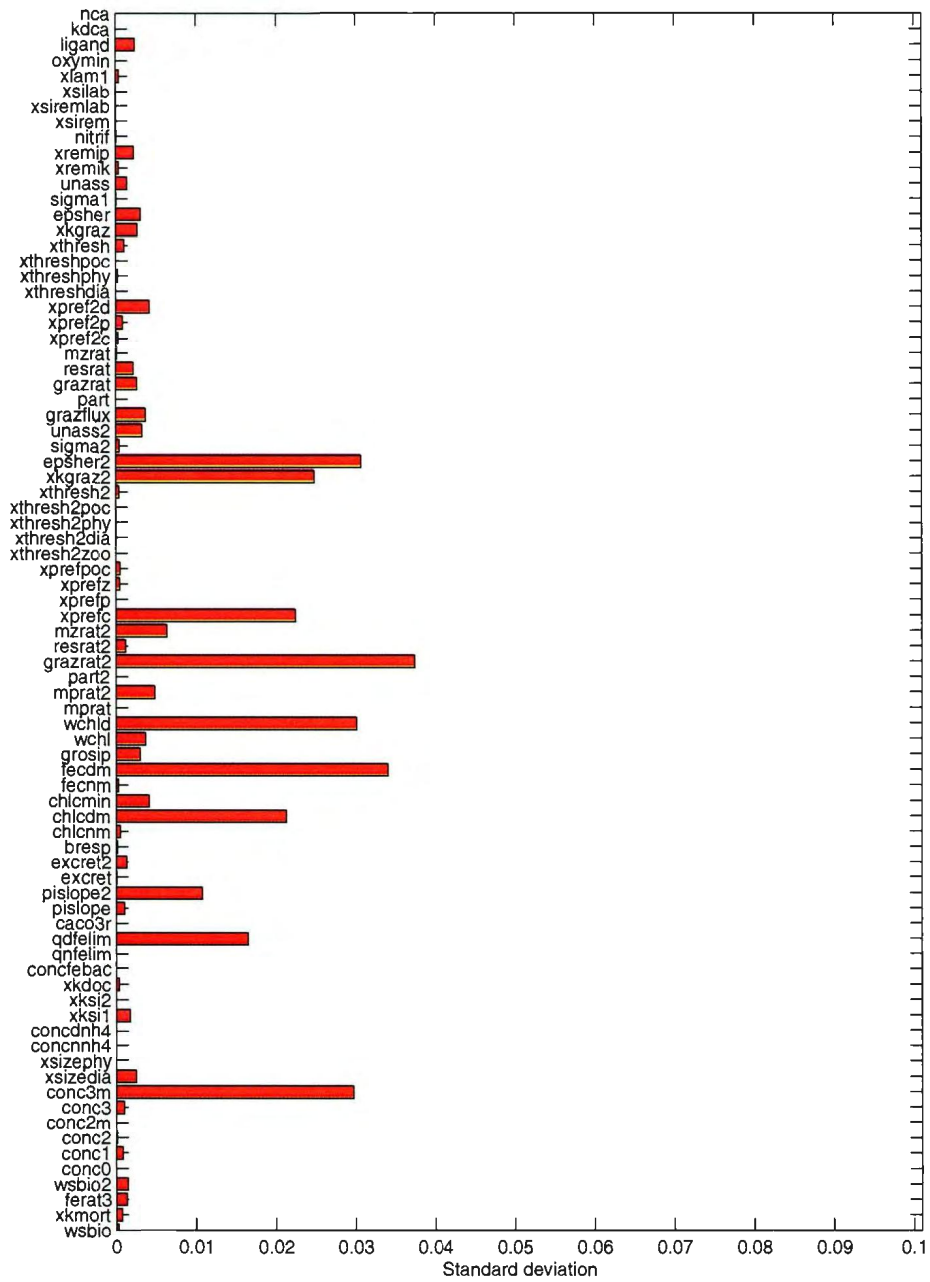
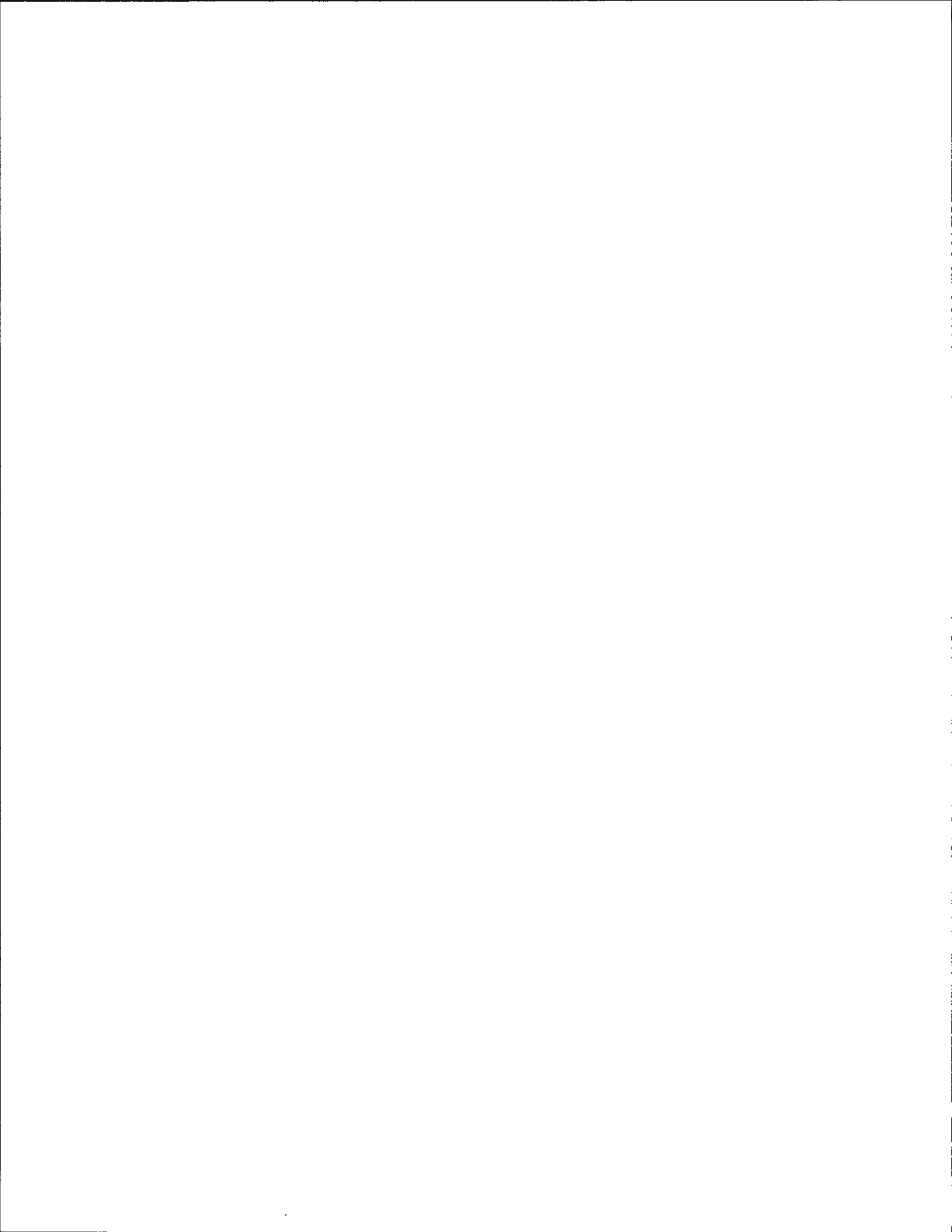
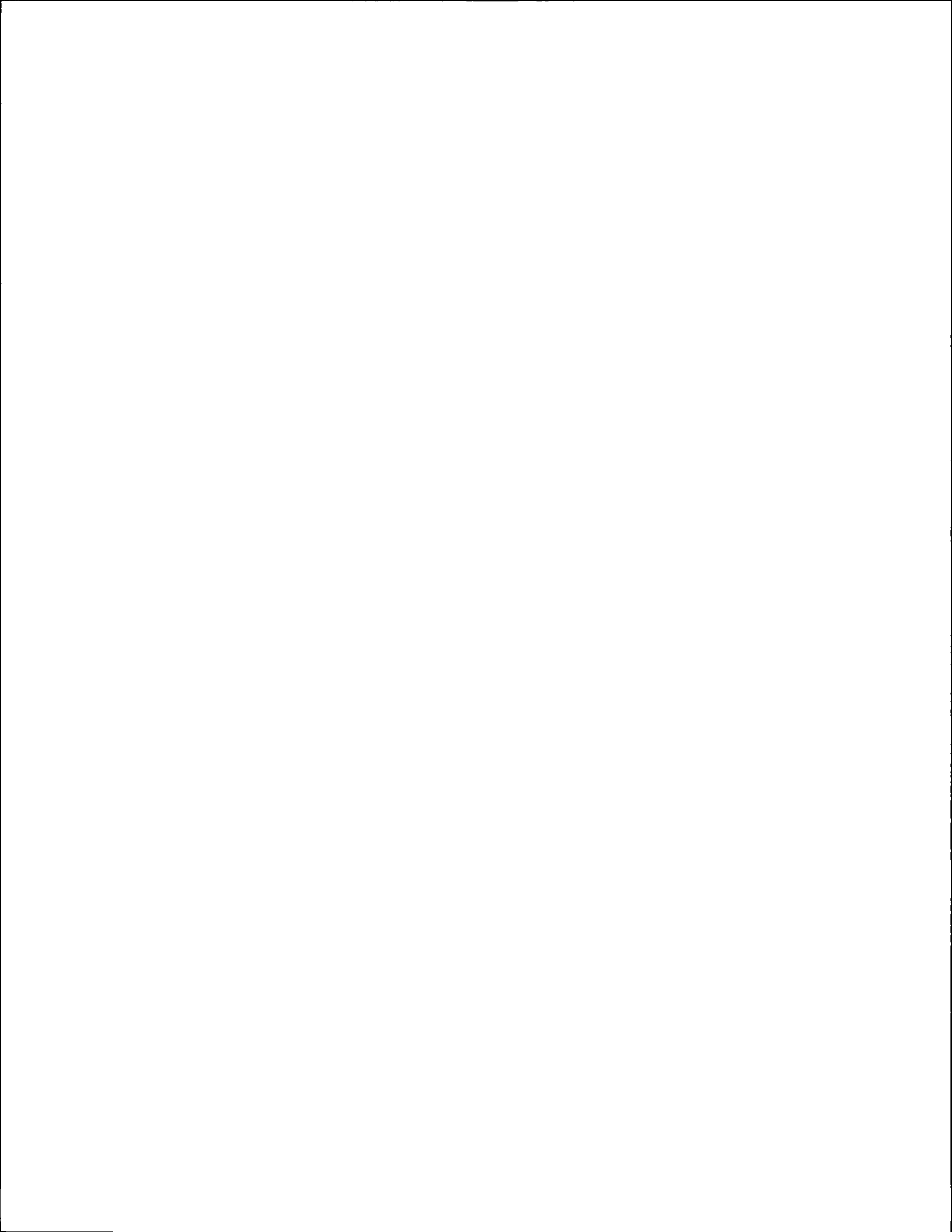


Figure 3.7: Same as Figure 3.5, but for Station 25





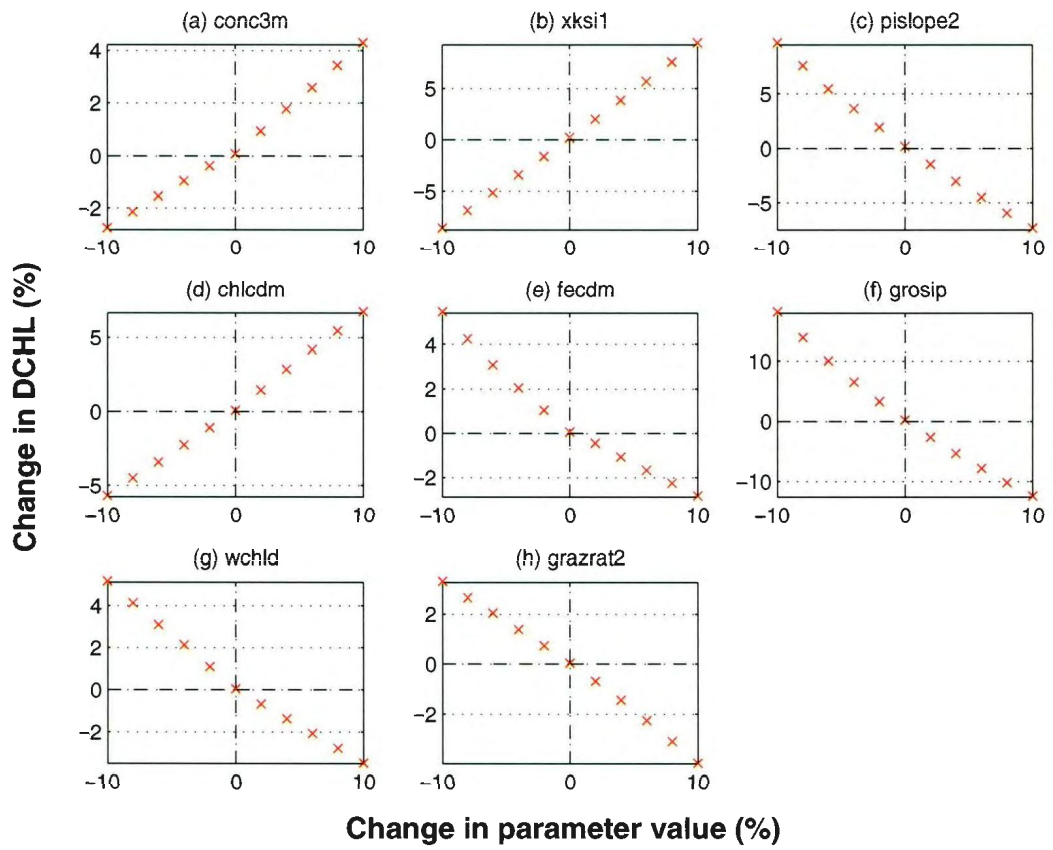


Figure 3.8: Diatoms response to variations in the key parameters at Station 8

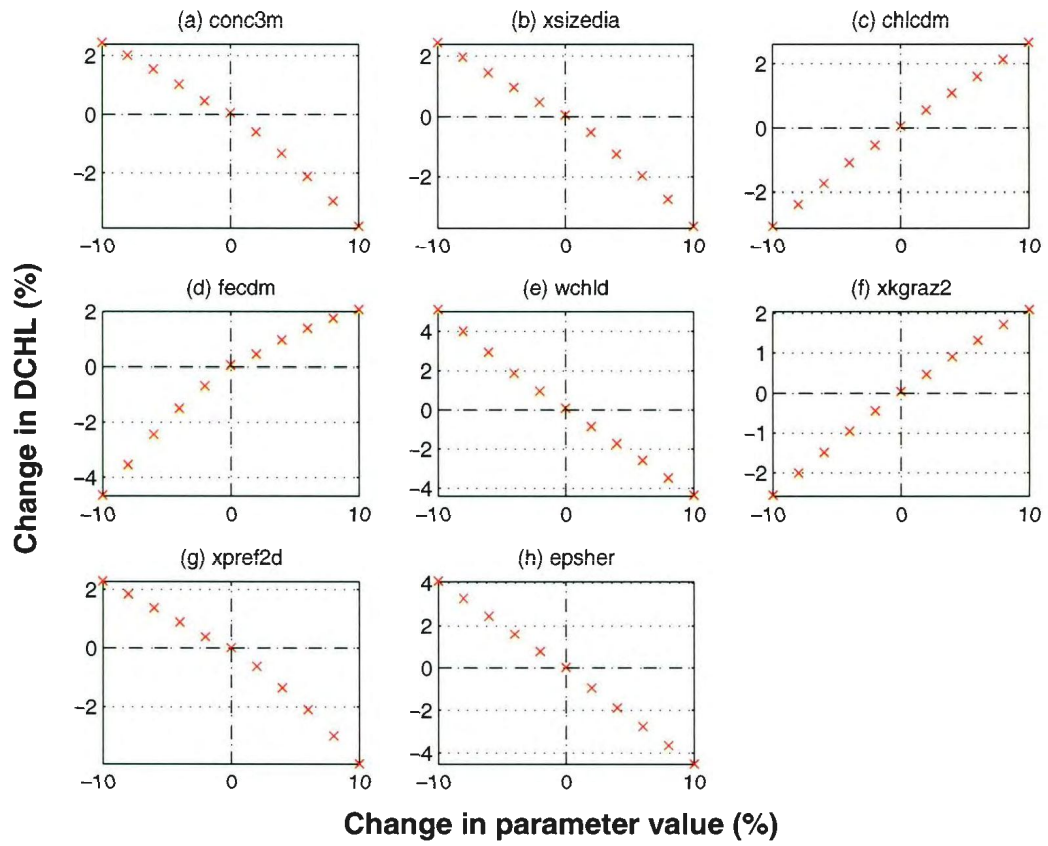


Figure 3.9: Same as Figure 3.8, but for Station 15

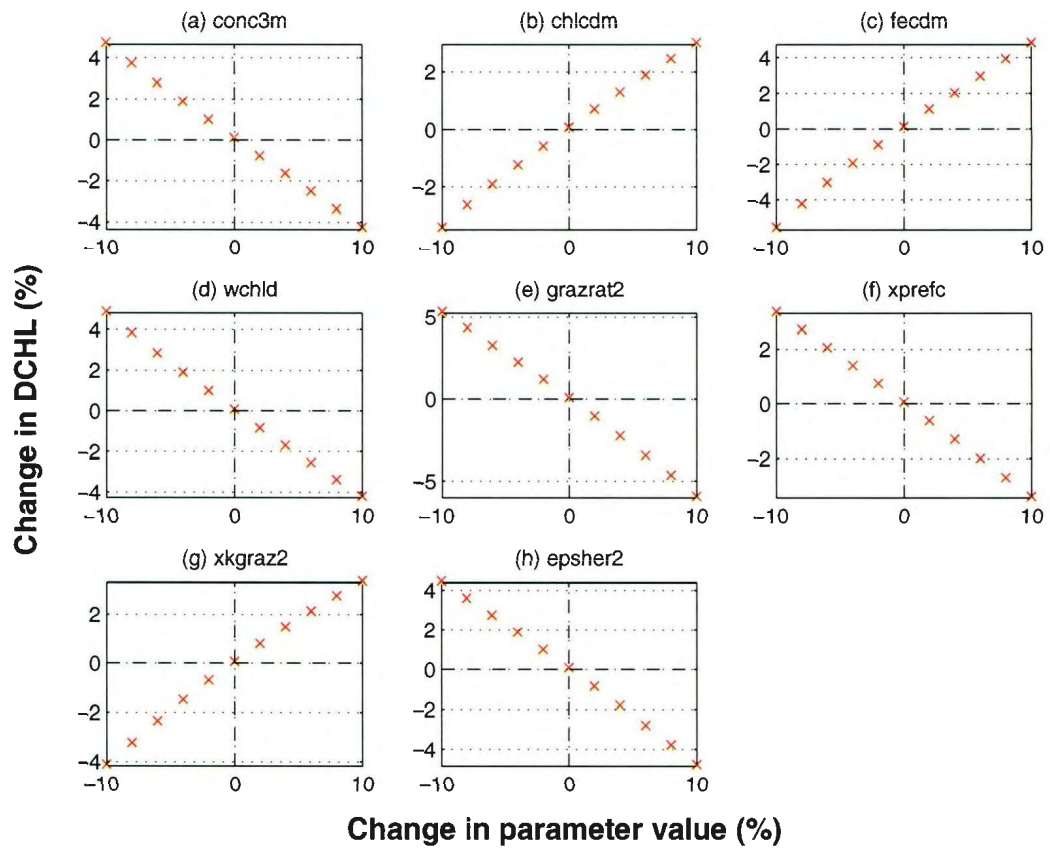


Figure 3.10: Same as Figure 3.8, but for Station 25

Chapter 4

Simulation of Coupled

Physical-Biogeochemical Seasonal

Variability in the Labrador Sea

The discussion of the model results continues in this chapter with analysis of seasonal evolutions of physical and biogeochemical tracers, followed by annual carbon cycle at three locations in the Labrador Sea.

4.1 Seasonal Physical and Biogeochemical Variability

4.1.1 Simulated Mixed Layer Depth and Surface Conditions

Figure 4.1 presents the annual evolutions of physical variables constraining the biogeochemical processes at the three stations that are simulated by the 3-D OPA model. The annual evolution of the simulated daily-mean turbocline are shown in Figure 4.1a. The turbocline is defined as the depth of certain threshold value of turbulent kinetic energy (TKE) which is assumed to be the minimum TKE value for which the flow is still in the turbulent regions. As such the turbocline depends on the intensity of the two major sources of TKE in the flow: buoyancy production and shear production. The buoyancy production is a major source of TKE in the winter in deep convection areas (i.e. Station 15). The shear becomes important in regions with strong flow shear such as the continental slope and the area of rim current. At all stations, strong vertical mixing prevails the mixed-layer depth (MLD) variations in winter. The simulated strong deep convection of 1994 starts to form a deep MLD starting in January, and reaches its peak in late March (in red). The maximum MLD depth at Station 15 is around 1750 m, within the range of observed values [142]. At Station 25, the model gives high MLD, which is triggered by strong shear in the rim current area.

Figures 4.1b-d show the simulated annual evolutions of surface atmospheric forcing and sea-ice cover for the three stations. At all stations, the surface wind possesses a wide range of day-to-day variability which can have profound impacts on ocean

temperature and vertical mixing (Figure 4.1b). The general features of the wind forcing are characterized by a period of strong wind (10 m/s on average) from January to mid-May, followed by a transition to a weaker-wind (5 m/s on average) period from mid-May to mid-August, which then returns back to the strong wind period until the end of the year. The temporal evolutions of simulated shortwave radiation are shown in Figure 4.1c. The incoming solar radiation starts to increase gradually in early spring, which becomes available abundantly ($> 100 \text{ W/m}^2$) until the end of August. The mean radiative flux exceeds 200 W/m^2 during June and most of July. Figure 4.1d shows the simulated sea-ice coverage. No sea-ice was found at Station 15 and 25 throughout the year. The sea-ice covered a fraction of sea surface at Station 8 during most of the winter (January-March) and for several days in April and May, which restricts the penetration of light, and hence, can limit the growth of phytoplankton.

4.1.2 Simulated Variability in the Surface 100 m Layer

To show general features of the model simulations, the results for several variables are presented and described separately for each station. Only the surface 100 m layer is looked at as the depth of euphotic layer did not exceed 100 m during the biologically productive season at all stations (not shown).

Station 8

Figure 4.2a and Figure 4.2b show the simulated annual evolutions of the vertical temperature and salinity profiles in the western Labrador Sea, respectively. Stratification starts to develop in June, forming a warm (above $6 \text{ }^\circ\text{C}$) and fresh (below 34.4

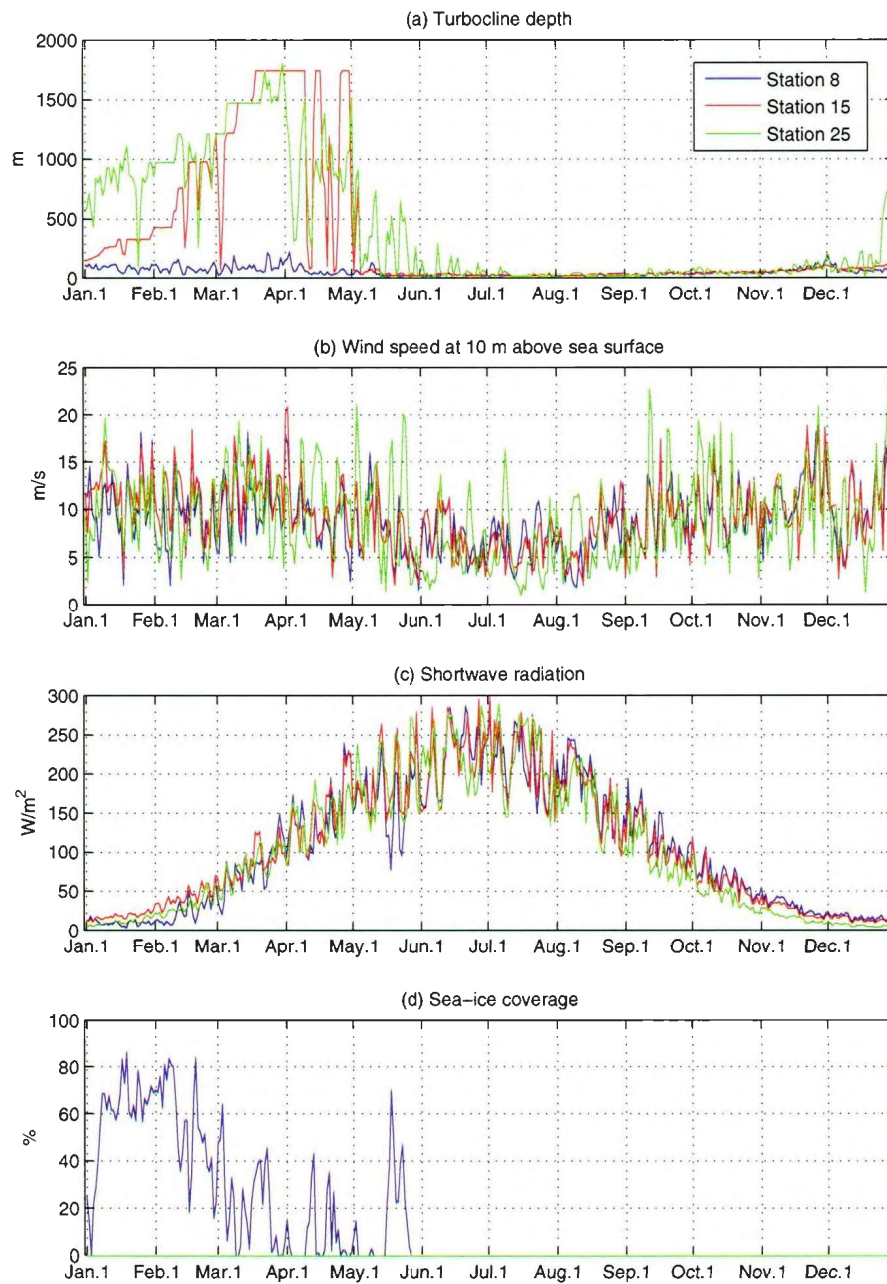


Figure 4.1: Simulated evolutions of a) turbocline depth, b) atmospheric wind at 10 above sea surface, c) shortwave radiation, and d) sea-ice cover.

PSU) surface layer extending down to about 40 m, deepening slowly until the end of October, and the water column begins to destratify in November. The temperature is below 3°C in the water column during winter, except for the adjustment period to initial conditions in January.

Figure 4.2c-h show the temporal evolution of the simulated DIC, nitrate, ammonium, phosphate, iron, and silicate, respectively. Reductions in DIC, nitrate, phosphate, and iron in the end of May correspond to the first nanophytoplankton bloom (Figure 4.3a) which occurs mostly in the upper 20 m and the maximum nanophytoplankton concentration reaches 10 $\mu\text{mol/L}$. The nanophytoplankton bloom triggers the growth of microzooplankton (Figure 4.3c) and the production of ammonium (Figure 4.2e), small particulate organic matter (Figure 4.3f) and calcite (Figure 4.3h). The second phytoplankton bloom is dominated by diatoms, which starts in the end of June, reaching its maximum value ($> 15 \mu\text{mol/L}$) in mid-July, and lasts until late fall. The bloom results in the depletions of DIC and all simulated nutrients (Figure 4.2c-h), whereas it promotes the growth of mesozooplankton (Figure 4.3d) and the production of big particulate organic matter (Figure 4.3g) and biogenic silica (Figure 4.3i).

The DOC concentration starts to increase with the first nanophytoplankton bloom and gradually throughout the rest of the year (Figure 4.3e). A considerable amount of DOC is found in the subsurface (below 40 m) during late fall, which is mostly associated with the remineralization of sinking particles that are accumulated during spring and summer (Figure 4.3f-i). The remineralization is followed by a rise in DIC and all nutrients (except for ammonium), which are brought back into the surface layer via mixing in December.

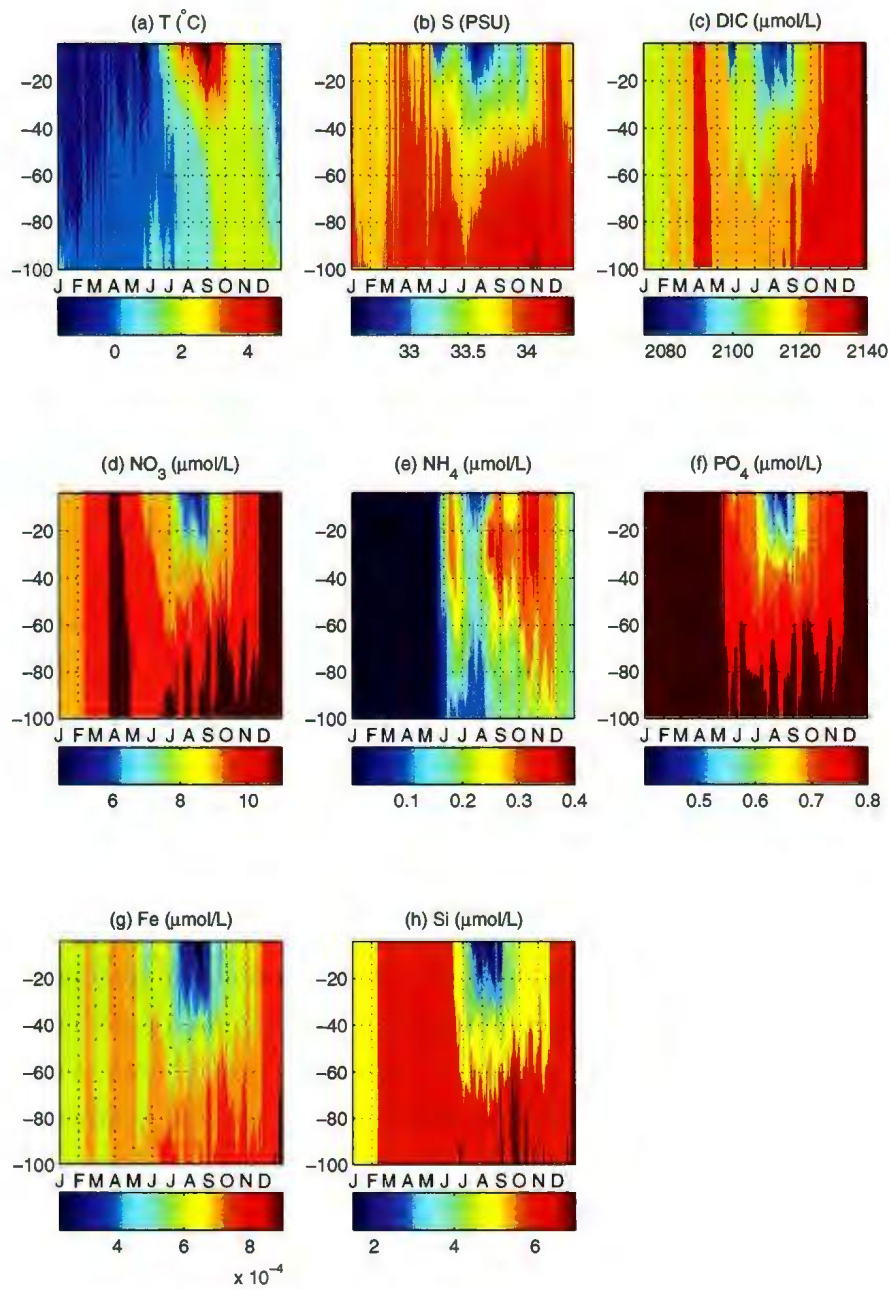


Figure 4.2: The evolution of simulated a) temperature, b) salinity, c) dissolved inorganic carbon, d) nitrate, e) ammonium, f) phosphate, g) iron, and h) silicate at Station 8

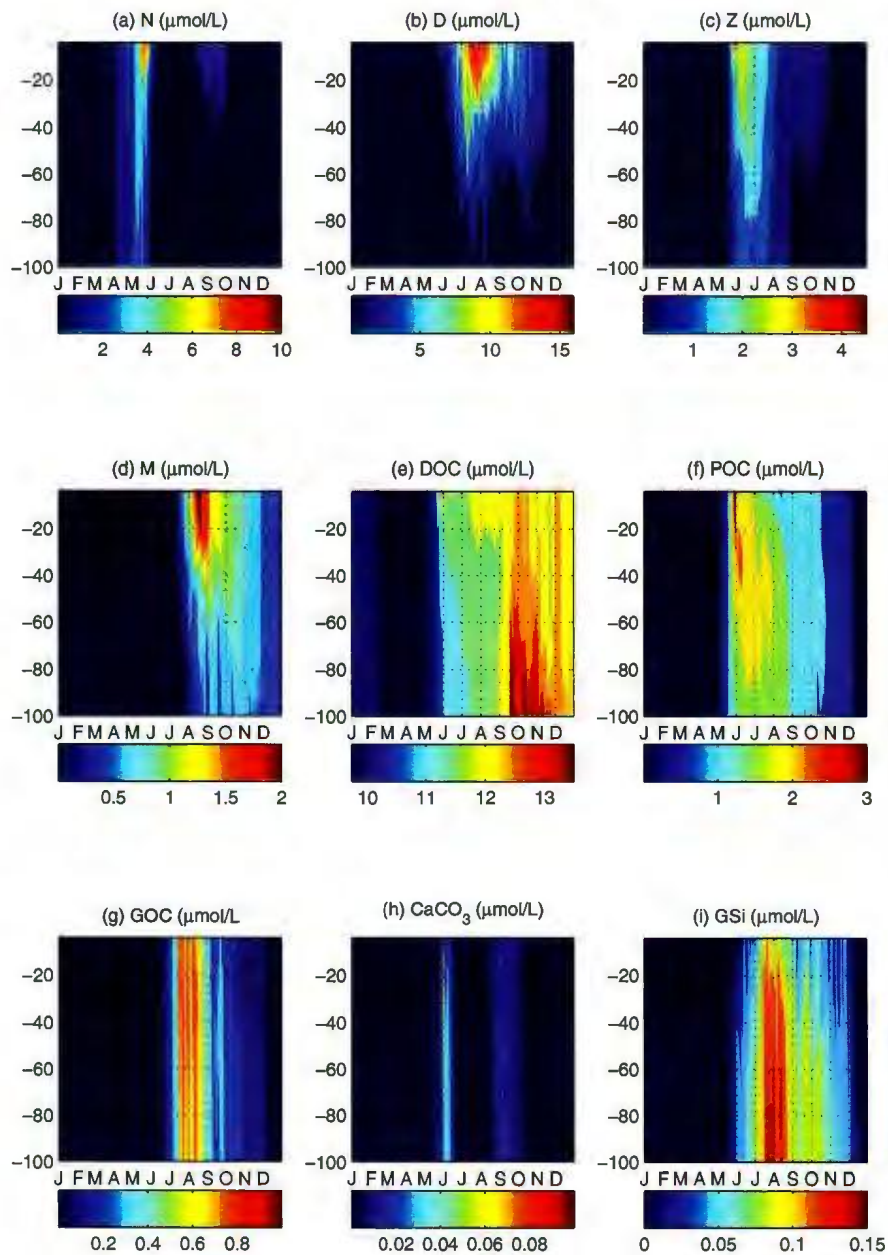


Figure 4.3: The evolution of simulated a) nanophytoplankton, b) diatoms, c) microzooplankton, d) mesozooplankton, e) dissolved organic matter, f) small particulate organic carbon, g) big particulate organic carbon, and h) calcite and i) biogenic silica at Station 8

Station 15

The simulated annual evolutions of the physical and biogeochemical tracers at Station 15 are shown in Figure 4.4 and Figure 4.5. Similarly to Station 8 (Figure 4.2a&b), a warm and fresh surface layer is formed in the top 40 m from June to November. Stratification at this station generates the formation of nutricline (Figure 4.4d-h), which is more distinct than the ones at Station 8 (Figure 4.2d-h). Due to substantial carbon uptake by phytoplankton, the seasonal drawdown of surface DIC coincides with the early nanophytoplankton bloom at the end of May (Figure 4.5a) and the late diatoms bloom in the end of June (Figure 4.5b). The early bloom by nanophytoplankton at this station (Figure 4.5a) is more intense (at least twice as large) than the one observed in the western Labrador Sea (Figure 4.3a), whilst the strengths of the late blooms by diatoms are about the same between the two stations (Figure 4.3a and Figure 4.5b). This leads to a greater rise in microzooplankton (Figure 4.5c), as well as the production and export of small particulate organic carbon (Figure 4.5f) and calcite (Figure 4.5h) at this station.

Simulated variations in DOC illustrated in Figure 4.5e are concentrated in the surface mixed layer, and not in the subsurface as seen for the Labrador coast (Figure 4.3e). In fall, remineralization and mixing reduce the DOC concentration and restore nutrients and DIC concentrations in the surface layer and almost throughout the top 100 m by the end of December.

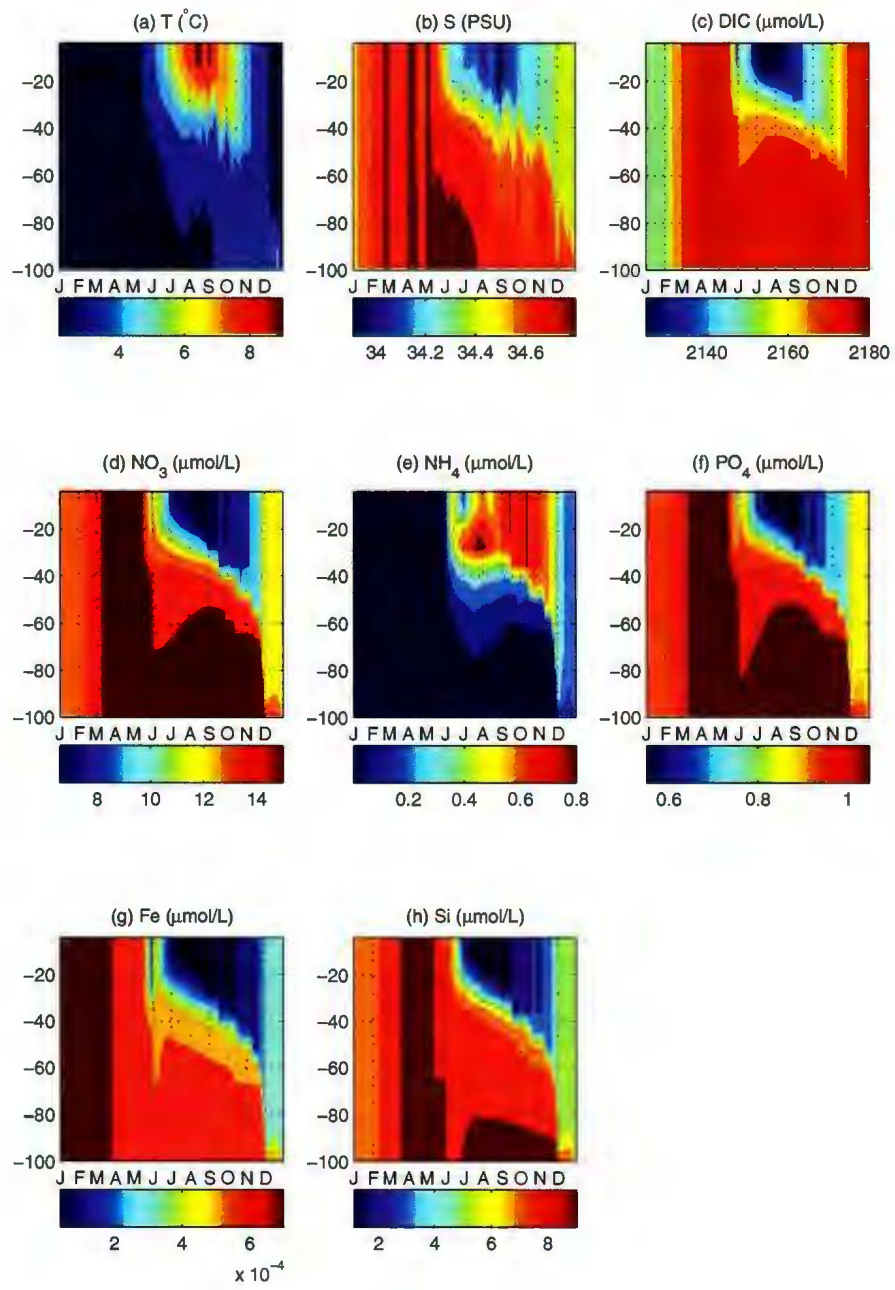


Figure 4.4: Same as Figure 4.2, but at Station 15

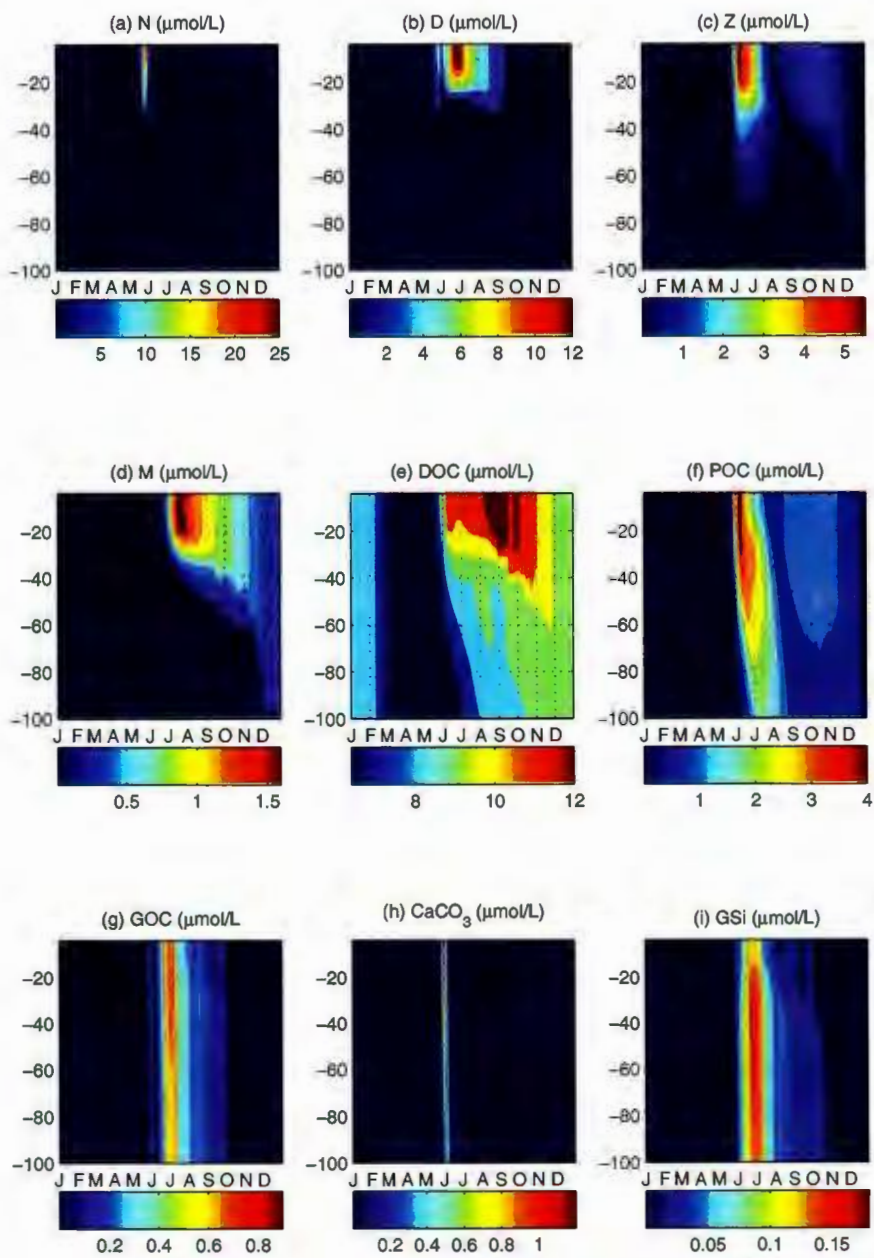


Figure 4.5: Same as Figure 4.3, but at Station 15

Station 25

The simulated annual evolution of vertical temperature and salinity profiles at Station 25 are presented in Figure 4.6a and Figure 4.6b, respectively. Both the structures and ranges of temperature and salinity variations at this station resemble those simulated for the central Labrador Sea (Figure 4.4a and Figure 4.4b) despite considerable differences in the initial temperature and salinity values between the two stations. As for the other two stations, stratification at Station 25 starts in June. The depth of the surface mixed layer is about 40 m, which deepens slowly and eventually the surface 100 m ocean is fully mixed again by the end of the year. The corresponding vertical distributions of DIC and nutrients (Figure 4.6c-h) are similar to those seen in the simulated results for the other side of the coastal region (Figure 4.2c-h).

The vertical profiles of simulated phytoplankton and zooplankton are illustrated in Figure 4.7a-d. The magnitude of the simulated blooms ($10\text{-}15\ \mu\text{mol/L}$) and the subsequent growth of zooplankton ($1.5\text{-}3\ \mu\text{mol/L}$) to the blooms are close to those simulated for the Labrador coast (Figure 4.3a-d). The concentration of nanophytoplankton starts to increase slowly in early June throughout the top 100 m, blooming in the beginning of July, and quickly diminishes by mid-July (Figure 4.2a) as a result of rapid grazing by microzooplankton (Figure 4.7c). Diatoms, on the other hand, experience a longer growing season with multiple spikes of which the maximum value ($> 15\ \mu\text{mol/L}$) appears in early August (Figure 4.7b). This extensive growth period is reflected on mesozooplankton, which starts to grow in late July, reaching its highest growth season ($> 1.5\ \mu\text{mol/L}$ in the top 20 m) from late August to mid-September, and decreases slowly for the remaining of the year.

The vertical distribution of simulated DOC is fairly uniform over the top 100 m layer (Figure 4.7e), which is similar to the simulated results for Station 8 (Figure 4.3e). However, the positions of DOC maxima at the two coastal regions differ from each other; the maximum DOC concentration is found in the subsurface (below 80 m) for Station 8, whereas for Station 25, it is located in the top 20 m.

As for the other two stations, the simulated annual evolutions of sinking particles are nearly uniform in the surface 100 m with a peak in each variable corresponding to the timing of phytoplankton blooms or maxima in zooplankton biomass (Figure 4.7f-i).

4.2 Simulated Annual Carbon Cycle

The annual evolutions of simulated sea-air $p\text{CO}_2$ difference ($\Delta p\text{CO}_2$) at Stations 8, 15, and 25 are shown in Figure 4.8a. First, it should be noted that the initial $p\text{CO}_2$ values at all stations are unreasonably low as compared to the fixed atmospheric $p\text{CO}_2$ level ($360 \mu\text{atm}$), which cause the development of an overly under-saturated waters throughout the year. In spite of this deficiency in the simulated results, the seasonal variability of $\Delta p\text{CO}_2$ are reasonably reproduced by the model, and therefore, is discussed in this section.

The sea-air $p\text{CO}_2$ difference is markedly increased in May at Stations 8 and 15 (Figure 4.8a), related to the spring phytoplankton bloom as shown by the increase of chlorophyll concentration in Figure 4.8b. This is equivalent to a surface ocean $p\text{CO}_2$ removal of approximately $43 \mu\text{atm}$ (Station 8) and $50 \mu\text{atm}$ (Station 15), which are less than the estimated bloom drawdown of $70 \mu\text{atm}$ in 2004 based on the measurement

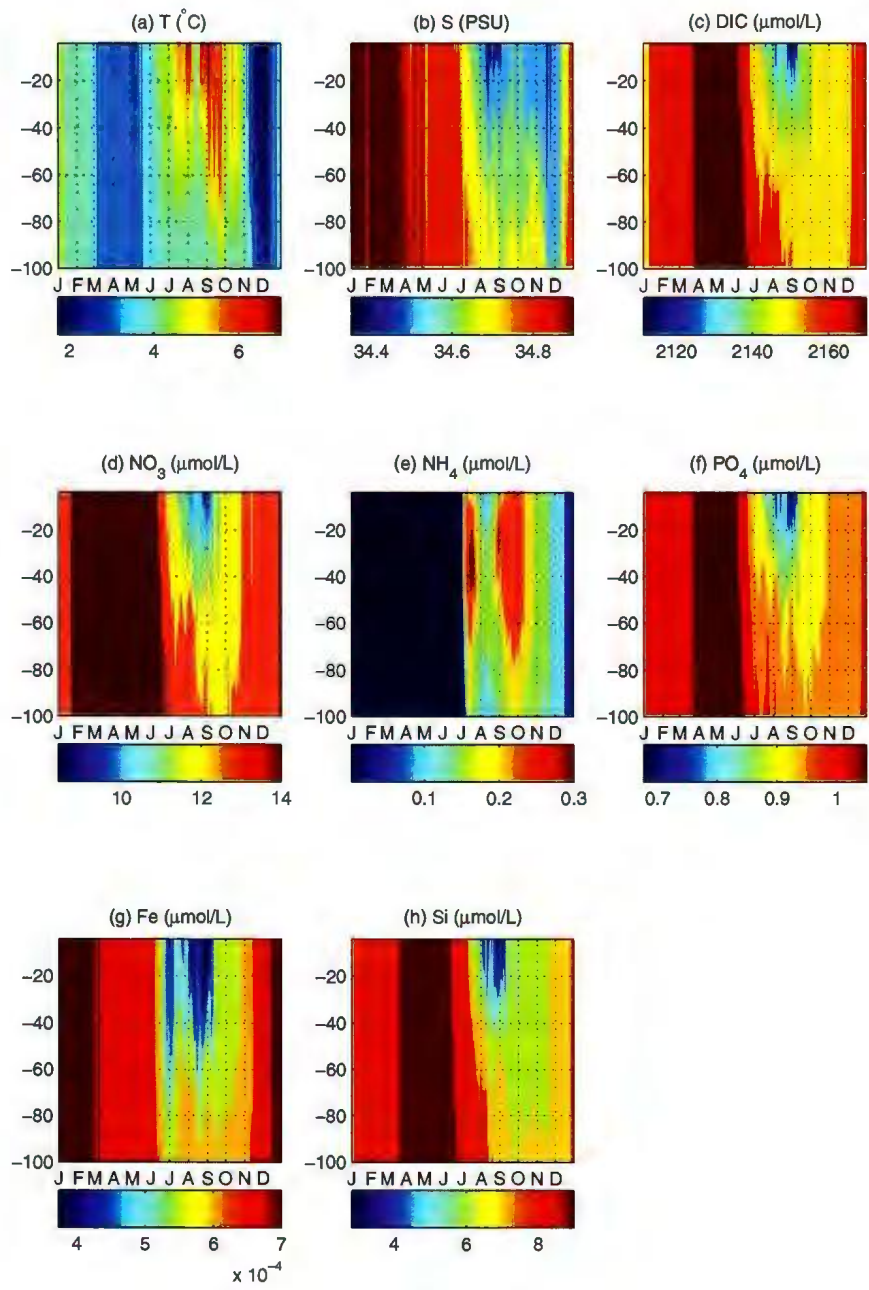


Figure 4.6: Same as Figure 4.2, but at Station 25

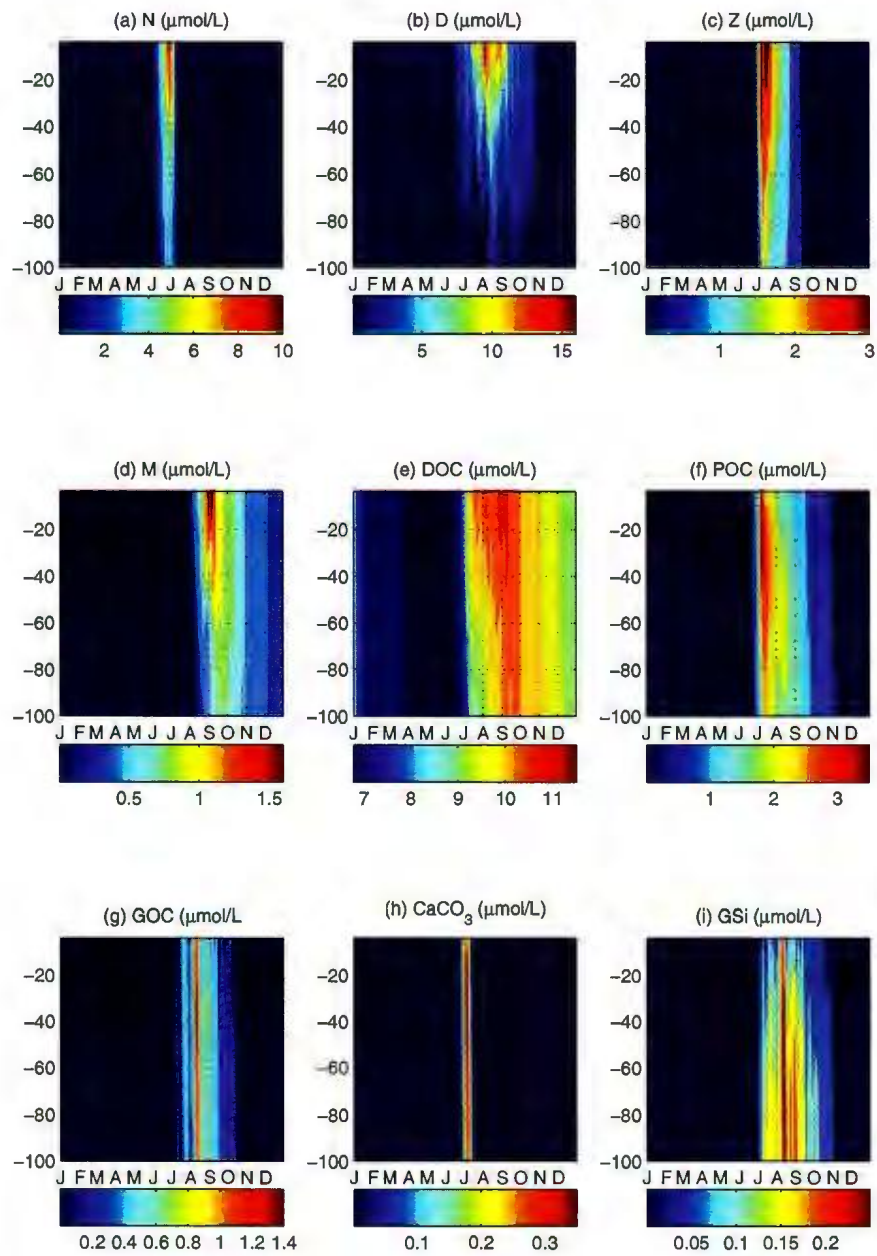


Figure 4.7: Same as Figure 4.3, but at Station 25

from mooring deployed in the central Labrador Sea [73]. In summer, variations in $\Delta p\text{CO}_2$ are driven by the photosynthetic utilization of CO_2 in the strongly stratified surface mixed layer [126], which can be seen as a similarity between fluctuations of $\Delta p\text{CO}_2$ (Figure 4.8a) and primary productivity (Figure 4.8b). In mid-August, the enhanced bloom generates the maximum $\Delta p\text{CO}_2$ ($-110 \mu\text{atm}$) for Station 25 (Figure 4.8a), which is close to the estimated value ($-102 \mu\text{atm}$) for 1990 in the western part of the Labrador Sea [127]. From September to the end of December, surface waters at Stations 8 and 15 maintain relatively high $p\text{CO}_2$ levels of about $-100 \mu\text{atm}$ and $-60 \mu\text{atm}$, respectively. Thus, at least from a qualitative point of view, the overall seasonal trends of low- $p\text{CO}_2$ primarily driven by bloom drawdown and high- $p\text{CO}_2$ during fall and winter are consistent with previous model and observational studies of the central Labrador Sea [17, 58, 73].

The seasonal variability of simulated sea-air DIC flux is shown in Figure 4.8c. Both the magnitude of DIC flux and the amplitude of its fluctuations are in general greater in winter, spring, and fall, than summer. Such seasonal trends are also present in the simulated annual evolution of surface wind (Figure 4.1d), which suggests the wind dependency of the DIC flux variability. The net annual atmospheric CO_2 sink based on the model simulation is 9.6044 mol/m^2 , 7.0605 mol/m^2 , and 7.2635 mol/m^2 for Stations 8, 15, and 25, respectively. The sink of CO_2 in the central Labrador Sea (Station 15) is about 35 % stronger than the estimated value from a 1-D box model (4.6 mol/m^2) [17] and 62 % stronger than the estimate from the same model for a different year ($2.7 \pm 0.8 \text{ mol/m}^2$) [58]. Most of this large difference between the simulated results and the previous studies can be attributed to the overly underestimated $p\text{CO}_2$ due to initial value problems, which create a large $\Delta p\text{CO}_2$. It should be noted

that the values found in the previous studies are based on the model simulations for 2001 [17] and 2004 [58], which are the years of negative NAO (Figure 1.5). Hence, another possible reason for the intensification of the DIC flux may arise from the enhanced turbulent flux for the present study, which is done for 1994, one of the highest positive NAO years in the last few decades.

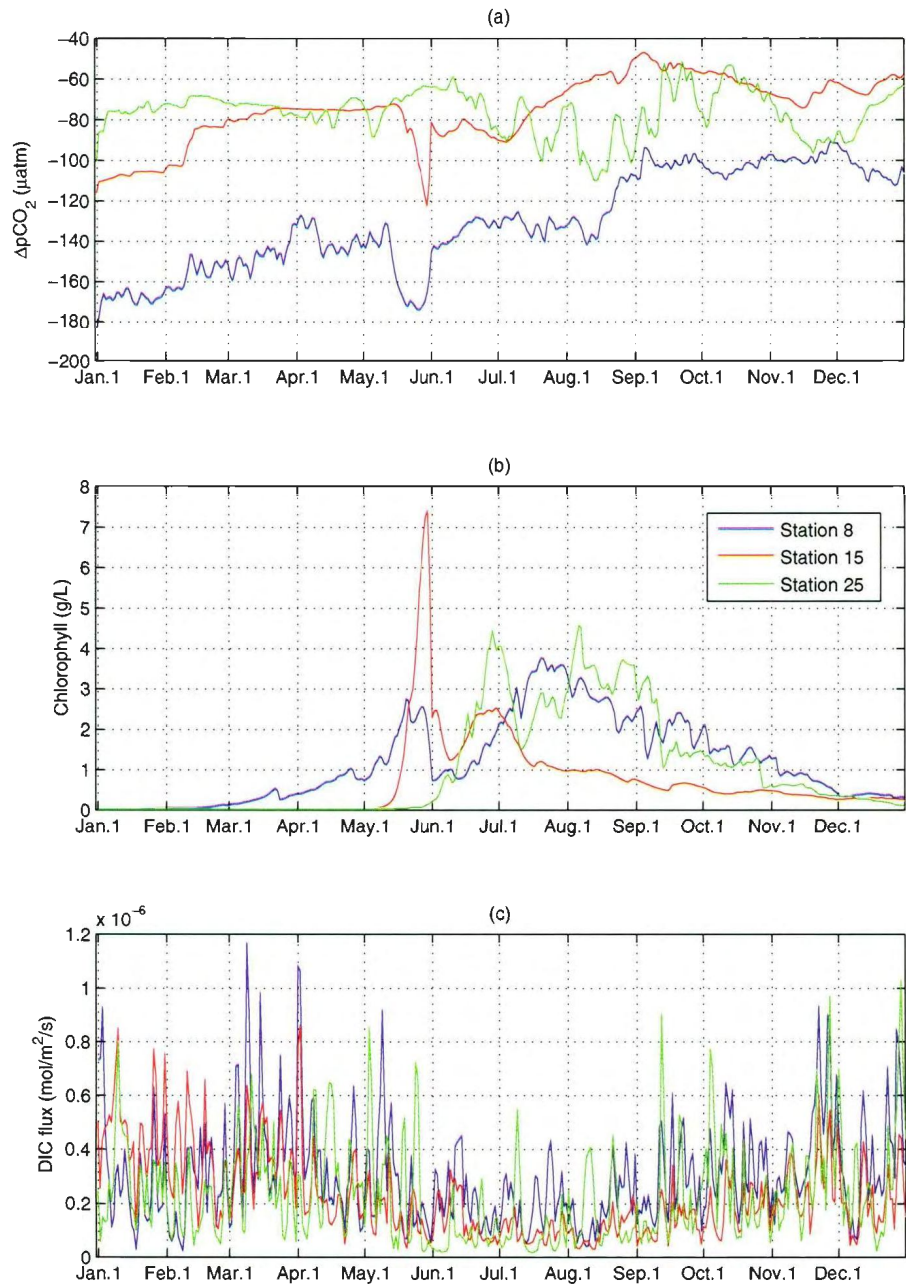


Figure 4.8: Simulated daily-mean a) sea-air $\Delta p\text{CO}_2$, b) surface chlorophyll concentration, and c) DIC flux at Stations 8, 15, 25

Chapter 5

Conclusions

The 1-D PISCES biogeochemical model was coupled to the OPA physical model in offline mode to study the seasonal physical and biogeochemical variability in the western, central, and eastern Labrador Sea. The results from the model simulations show the model's capability in resolving the general structures of observed vertical nutrients and oxygen profiles at Stations 8, 15, and 25 of the AR7W line, while the simulated vertical DIC profiles experience misfit with the data consistently at all three locations. Persistent misfit was found between the simulated and observed profiles of DIC, as well as the surface structures of nutrients depletion and oxygen saturation. The magnitude of the misfit was found to be related to the diurnal variations in PAR, which are not incorporated in PISCES, and errors due to unresolved processes of horizontal and vertical advection.

The annual evolution of the modeled surface chlorophyll concentration was validated with the weekly composite of the SeaWiFS climatology. The model simulated the seasonal cycle of primary production in the central the Labrador Sea reasonably

well, with a correlation coefficient of 0.88. The model-data misfit in the magnitude and timing of the phytoplankton was found for the coastal regions, which arises from a combination of physical factors and processes that are not resolved in the 1-D offline model, such as vertical advection and eddy-driven horizontal transport of diatoms. An additional uncertainty presumably is related to not well known coefficients in parameterizations used by the biogeochemical model.

The results of the sensitivity experiments suggest a spatial dependency of the model response to variations in the parameters. In particular, the magnitude of the diatoms bloom appears to be most sensitive to the mean silicon-to-carbon ratio (*grosip*) in the western Labrador Sea, in which the amplitude of the change in the chlorophyll content of diatoms was about three times greater than the central and eastern Labrador Sea. While most of the sensitive parameters were directly related to the diatoms, other parameters have shown to have crucial impacts on the diatoms bloom as well, that are indirectly related and specific to each of the simulated stations. Interestingly, two key parameters (*xpref2d* and *epsher*) for the central Labrador Sea are the controlling parameters for the physiology of microzooplankton, while for Station 25, three parameters (*xprefc*, *xkgraz2*, *epsher2*) appear to be significant that are related to the functionality of mesozooplankton. The diatoms bloom fluctuated linearly to parameter variations of the tested range for all of the parameters examined.

The results of the model simulations were further discussed to describe the simulated seasonal variability of physical and biogeochemical processes involved in the low trophic level ecosystem and carbon dynamics in the euphotic layer. The model depicted the characteristics of the annual evolutions of biogeochemical tracers specific to the simulated regions. The bloom drawdown of surface DIC and export through

sinking are captured well by the model, at least in a qualitative sense. The surface $p\text{CO}_2$ concentration was systematically lower than the observational estimate all year round, which can be attributed to the underestimated initial conditions for DIC.

This study has shown the applicability of the PISCES biogeochemical model for regional coupled physical-biogeochemical modeling. Furthermore, it has demonstrated that the offline coupling of the 1-D PISCES model and the 3-D eddy-resolving OPA model can be used as a tool for model testing and improvement with relatively low computational resources.

Chapter 6

Future Work

The present study has taken the initiative towards the development of community biogeochemical model for understanding the role of the Labrador Sea in the global carbon cycle and Earth system, which is a part of the VITALS project (For more information about the project, visit: http://www.nserc-crsng.gc.ca/_doc/Professors-Professeurs/CCAR-RCCA_eng.pdf). Based on the results of the model simulations and the sensitivity analysis, the following future work is suggested for the model implementation:

- Improvement on vertical mixing in the physical model, especially for coastal regions.
- Assessment of spatial variability of the results from sensitivity analysis over the entire model domain.
- Optimization of model parameters through data assimilation with surface chlorophyll.

- Implementation of the 3-D coupled model.
- Process studies of the 3-D interannual variability.

Bibliography

- [1] C. B. Andersen. Understanding carbonate equilibria by measuring alkalinity in experimental and natural systems. *Journal of geoscience education*, 50(4):389–403, 2002.
- [2] J. Antonov, R. Locarnini, T. Boyer, A. Mishonov, and H. Garcia. *World Ocean Atlas 2005, Volume 2: Salinity*. S. Levitus, Ed. U.S. Gov. Printing Office, Wash., D.C. NOAA Atlas NESDIS 61, 182pp., 2006.
- [3] D. E. Archer. An atlas of the distribution of calcium carbonate in sediments of the deep sea. *Global Biogeochemical Cycles*, 10(1):159–174, 1996.
- [4] J. Aristegui, J. M. Gasol, C. M. Duarte, and G. J. Herndl. Microbial oceanography of the dark ocean’s pelagic realm. *Limnology and Oceanography*, 54(5):1501–1529, 2009.
- [5] O. Aumont, S. Belviso, and P. Monfray. Dimethylsulfoniopropionate (DMSP) and dimethylsulfide (DMS) sea surface distributions simulated from a global 3-D ocean carbon cycle model. *Journal of Geophysical Research*, 107:4–15, 2002.
- [6] O. Aumont and L. Bopp. Globalizing results from ocean in situ iron fertilization studies. *Global Biogeochemical Cycles*, 20(2):GB2017, 2006.

- [7] O. Aumont and the PISCES community. PISCES: An ocean biogeochemical model for carbon and ecosystem studies. 79pp., 2013.
- [8] W. M. Berelson. Particle settling rates increase with depth in the ocean. *Deep Sea Research Part II: Topical Studies in Oceanography*, 49(13):237–251, 2001.
- [9] J. Bjerrum. *Metal Ammine Formation in Aqueous Solution: Theory of the Reversible Step Reactions*. PhD thesis, University of Copenhagen. 296pp., 1941.
- [10] J. Carton. A reanalysis of ocean climate using Simple Ocean Data Assimilation (SODA). *Monthly Weather Review*, 136(8):2999–3017, 2008.
- [11] P. Claquin, V. Martin-Jezequel, J. C. Kromkamp, M. J. W. Veldhuis, and G. W. Kraay. Uncoupling of silicon compared with carbon and nitrogen metabolisms and the role of the cell cycle in continuous cultures of *Thalassiosira pseudonana* (Bacillariophyceae) under light, nitrogen, and phosphorus control. *Journal of Phycology*, 38(5):922–930, 2002.
- [12] M. Conkright, H. Garcia, T. O'Brien, R. Locarnini, T. Boyer, C. Stephens, and J. Antonov. *World Ocean Atlas 2001, Volume 4: Nutrients*. S. Levitus, Ed. U.S. Gov. Printing Office, Wash., D.C. NOAA Atlas NESDIS 52, 392pp., 2002.
- [13] A. Corbiere, N. Metzl, G. Reverdin, C. Brunet, and A. Takahashi. Interannual and decadal variability of the oceanic carbon sink in the North Atlantic subpolar gyre. *Tellus Series Biochemical and Physical Meteorology*, 59(2):168–178, 2007.

- [14] J. Cuny, P. Niiler, and S. Bacon. Labrador sea boundary currents and the fate of the irvinger sea water. *Journal of Physical Oceanography*, 32(2):627–647, 2002.
- [15] H. J. W. de Baar and J. T. M. de Jong. Distributions, sources, and sinks of iron in seawater. In D. Turner and K. Hunter, editors, *The biogeochemistry of iron in seawater*, pages 85–121. J. Willey, Chichester; New York, 2001.
- [16] A. W. Decho. Microbial exopolymer secretions in ocean environments: Their role(s) in food webs and marine processes. *Oceanogr. Mar. Biol. Ann. Rev.*, 28:73–153, 1990.
- [17] M. DeGrandpre, A. Körtzinger, U. Send, D. W. R. Wallace, and R. G. J. Bellerby. Uptake and sequestration of atmospheric CO₂ in the Labrador Sea deep convection region. *Geophysical Research Letters*, 33:L21S03, 2006.
- [18] M. Dengler, J. Fischer, F. Schott, and R. J. Zantopp. The deep labrador current and its variability in 1996–2005. *Geophysical Research Letters*, (33):5, 2006.
- [19] K. Denman, G. Brasseur, A. Chidthaisong, P. Ciais, P. M. Cox, R. D. D. Hauglustaine, C. Heinze, E. Holland, D. Jacob, U. Lohmann, S. Ramachandran, P. L. da Silva Dias, S. C. Wofsy, and X. Zhang. Couplings between changes in the climate system and biogeochemistry. In *Climate Change 2007: The Physical Science Basis. Contribution of Working Group I to the Fourth Assessment Report of the Intergovernmental Panel on Climate Change [Solomon, S., D. Qin, M. Manning, Z. Chen, M. Marquis, K. B. Averyt, M. Tignor and*

H. L. Miller (eds.)], pages 663–745. Cambridge University Press, Cambridge, United Kingdom and New York, NY, USA, 2007.

- [20] Department of Fisheries and Oceans. BioChem: database of biological and chemical oceanographic data. Version 8. Department of Fisheries and Oceans, Canada. <http://www.meds-sdmm.dfo-mpo.gc.ca/biochem/biochem-eng.htm>, 2005. Database accessed on: 2013-05-10.
- [21] R. Dickson, J. Meincke, P. Rhines, and J. Swift. Long-term coordinated changes in the convective activity of the north atlantic. *Progress in Oceanography*, 38(3):241–295, 1996.
- [22] L. Dilling and A. L. Alldredge. Fragmentation of marine snow by swimming macrozooplankton: A new process impacting carbon cycling in the sea. *Deep Sea Research Part I: Oceanographic Research Papers*, 47(7):1227–1245, 2000.
- [23] S. C. Doney, I. Lima, J. K. Moore, K. Lindsay, M. J. Behrenfeld, T. K. Westberry, N. Mahowald, D. M. Glover, and T. Takahashi. Skill metrics for confronting global upper ocean ecosystem-biogeochemistry models against field and remote sensing data. *Journal of Marine Systems*, 76(1-2):95–112, 2009.
- [24] G. J. Doucette and P. J. Harrison. Aspects of iron and nitrogen nutrition in the red tide dinoflagellate *Gymnodinium sanguineum*. *Marine Biology*, 110(2):165–173, 1991.
- [25] M. R. Droop. 25 years of algal growth-kinetics - A personal view. *Botanica Marina*, 26(3):99–112, 1983.

- [26] C. Ethé. 1-d vertical configuration in nemo system. Technical report, Laboratoire d'Océanographie et du Climat : Expérimentation et Approches Numériques. 11pp., 2005.
- [27] P. Falkowski, R. J. Scholes, E. Boyle, J. Canadell, D. Canfield, J. Elser, N. Gruber, K. Hibbard, P. Hgberg, S. Linder, F. T. Mackenzie, B. Moore III, T. Pedersen, Y. Rosenthal, S. Seitzinger, V. Smetacek, and W. Steffen. The global carbon cycle: A test of our knowledge of earth as a system. *Science*, 290(5490):291–296, 2000.
- [28] P. G. Falkowski, R. T. Barber, and V. Smetacek. Biogeochemical controls and feedbacks on ocean primary production. *Science*, 281(5374):200–206, 1998.
- [29] W. Fennel and T. Neumann. Chapter 5 physical biological interaction. In *Introduction to the Modelling of Marine Ecosystem*, volume 72 of *Elsevier Oceanography Series*, pages 129–181. Elsevier, 2004.
- [30] T. Fichefet and M. Maqueda. Sensitivity of a global sea ice model to the treatment of ice thermodynamics and dynamics. *Journal Of Geophysical Research-Oceans*, 102(C6):12609–12646, 1997.
- [31] K. J. Flynn and C. R. Hipkin. Interactions between iron, light, ammonium, and nitrate: Insights from the construction of a dynamic model of algal physiology. *Journal of Phycology*, 35(6):1171–1190, 1999.
- [32] E. Frajka-Williams, P. B. Rhines, and C. C. Eriksen. Physical controls and mesoscale variability in the labrador sea spring phytoplankton bloom ob-

- served by seaglider. *Deep-Sea Research Part I: Oceanographic Research Papers*, 56(12):2144–2161, 2009.
- [33] V. M. Franck, M. A. Brzezinski, K. H. Coale, and D. M. Nelson. Iron and silicic acid concentrations regulate Si uptake north and south of the Polar Frontal Zone in the Pacific Sector of the Southern Ocean. *Deep Sea Research Part II: Topical Studies in Oceanography*, 47(15-16):3315–3338, 2000.
- [34] P. Gaspar, Y. Grgoris, and J.-M. Lefevre. A simple eddy kinetic energy model for simulations of the oceanic vertical mixing: Tests at station papa and long-term upper ocean study site. *Journal of Geophysical Research: Oceans*, 95(C9):16179–16193, 1990.
- [35] M. Gehlen, L. Bopp, N. Ernprin, O. Aumont, C. Heinze, and O. Raguencau. Reconciling surface ocean productivity, export fluxes and sediment composition in a global biogeochemical ocean model. *Biogeosciences*, 3(4):521–537, 2006.
- [36] R. J. Geider, H. L. MacIntyre, and T. M. Kana. A dynamic model of photoadaptation in phytoplankton. *Limnology and Oceanography*, 41(1):1–15, 1996.
- [37] R. J. Geider, H. L. Macintyre, and T. M. Kana. A Dynamic Regulatory Model of Phytoplanktonic Acclimation to Light, Nutrients, and Temperature. *Limnology and Oceanography*, 43:679–694, 1998.
- [38] W. Gentleman, A. Leising, B. Frost, S. Strom, and J. Murray. Functional responses for zooplankton feeding on multiple resources: a review of assumptions and biological dynamics. *Deep Sea Research Part II: Topical Studies in Oceanography*, 50(22-26):2847–2875, 2003.

- [39] J. C. Goldman and M. R. Dennett. Ammonium regeneration and carbon utilization by marine bacteria grown on mixed substrates. *Marine Biology*, 109(3):369–378, 1991.
- [40] D. Gregory and S. Narayanan. BioChem: A National Archive for Marine Biology and Chemistry Data. *AZMP Bulletin PMZA* 3:11-13, 2003.
- [41] N. Gruber, M. Gloor, S. E. Mikaloff Fletcher, S. C. Doney, S. Dutkiewicz, M. J. Follows, M. Gerber, A. Jacobson, F. Joos, K. Lindsay, D. Menemenlis, A. Mouchet, S. A. Mller, J. L. Sarmiento, and T. Takahashi. Oceanic sources, sinks, and transport of atmospheric CO₂. *Global Biogeochemical Cycles*, 23(1):GB1005, 2009.
- [42] G. I. Harrison and F. M. M. Morel. Response of the marine diatom *thalassiosira weissflogii* to iron stress. *Limnology and Oceanography*, 31(5):989–997, 1986.
- [43] W. G. Harrison and W. K. W. Li. Phytoplankton growth and regulation in the labrador sea: Light and nutrient limitation. *Journal of Northwest Atlantic Fishery Science*, 39:71–82, 2007.
- [44] B. D. Honeyman, L. S. Balistrieri, and J. W. Murray. Oceanic trace metal scavenging: the importance of particle concentration. *Deep Sea Research Part I: Oceanographic Research Papers*, 35(2):227–246, 1988.
- [45] J. W. Hurrell. Decadal trends in the north atlantic oscillation: Regional temperatures and precipitation. *Science*, 269(5224):676–679, 1995.

- [46] J. W. Hurrell, Y. Kushnir, G. Ottersen, and M. Visbeck. An overview of the north atlantic oscillation. *Structure*, 134(2003):1–35, 2003.
- [47] International Hydrographic Organization. Limits of oceans and seas, 3rd edition. International Hydrographic Organization, 38pp. 1953.
- [48] H. Jansen and D. A. Wolf-Gladrow. Carbonate dissolution in copepod guts: a numerical model. *Marine Ecology Progress Series*, 221:199–207, 2001.
- [49] K. S. Johnson, F. P. Chavez, and G. E. Friederich. Continental-shelf sediment as a primary source of iron for coastal phytoplankton. *Nature*, 398(6729):697–700, 1999.
- [50] F. Joos, G.-K. Plattner, T. F. Stocker, O. Marchal, and A. Schmittner. Global Warming and Marine Carbon Cycle Feedbacks on Future Atmospheric CO₂. *Science*, 284(5413):464–467, 1999.
- [51] E. Kalnay, R. Kistler, W. Collins, D. Deaven, and L. Gandin. The NCEP/NCAR 40-year reanalysis project. *Bulletin of the American Meteorological Society*, 77(3):437–471, 1996.
- [52] C. D. Keeling, R. B. Bacastow, A. E. Bainbridge, C. A. Ekdahl, P. R. Guenther, L. S. Waterman, and J. F. S. Chin. Atmospheric carbon dioxide variations at mauna loa observatory, hawaii. *Tellus*, 28(6):538–551, 1976.
- [53] R. M. Key, A. Kozyr, C. L. Sabine, K. Lee, R. Wanninkhof, J. L. Bullister, R. A. Feely, F. J. Millero, C. Mordy, and T.-H. Peng. A global ocean carbon

- climatology: Results from Global Data Analysis Project (GLODAP). *Global Biogeochemical Cycles*, 18(4):GB4031, 2004.
- [54] S. Khatiwala, P. Schlosser, and M. Visbeck. Rates and mechanisms of water mass transformation in the labrador sea as inferred from tracer observations. *Journal of Physical Oceanography*, 32:666–686, 2002.
- [55] S. Khatiwala and M. Visbeck. An estimate of the eddy-induced circulation in the labrador sea. *Geophysical Research Letters*, 27:2277–2280, 2000.
- [56] D. Kieke and M. Rhein. Variability of the overflow water transport in the western subpolar North Atlantic, 1950-97. *Journal of Physical Oceanography*, 36(3):435–456, 2006.
- [57] J. A. Kleypas and C. Langdon. *Coral Reefs and Changing Seawater Carbonate Chemistry*, pages 73–110. American Geophysical Union, 2013.
- [58] A. Körtzinger, U. Send, D. W. R. Wallace, J. Karstensen, and M. DeGrandpre. Seasonal cycle of O₂ and pCO₂ in the central Labrador Sea: Atmospheric, biological, and physical implications. *Global Biogeochemical Cycles*, 22(1):GB1014, 2008.
- [59] D. Langmuir. *Aqueous environmental geochemistry*. Prentice Hall. 586pp., 1997.
- [60] K. Lavender and W. Owens. Mid-depth recirculation observed in the interior labrador and irvinger seas by direct velocity measurements. *Nature*, 407(6800):66–69, 2000.

- [61] E. Laws, P. Falkowski, W. Smith, H. Ducklow, and J. McCarthy. Temperature effects on export production in the open ocean. *Global Biogeochemical Cycles*, 14(4):1231–1246, 2000.
- [62] J. Lazier, R. Hendry, A. Clarke, I. Yashayaev, and P. Rhines. Convection and restratification in the labrador sea, 1990-2000. *Deep-Sea Research Part I: Oceanographic Research Papers*, 49(10):1819–1835, 2002.
- [63] N. Lefvre, A. J. Watson, A. Olsen, A. F. Ros, F. F. Prez, and T. Johannessen. A decrease in the sink for atmospheric CO₂ in the North Atlantic. *Geophysical Research Letters*, 31(7):L07306, 2004.
- [64] J. M. Lilly, P. B. Rhines, F. Schott, K. Lavender, J. Lazier, U. Send, and E. DAsaro. Observations of the labrador sea eddy field. *Progress in Oceanography*, 59(1):75–176, 2003.
- [65] R. Locarnini, T. O'Brien, H. Garcia, J. Antonov, T. Boyer, M. Conkright, and C. Stephens. *World Ocean Atlas 2001, Volume 3: Oxygen. S. Levitus, Ed.* U.S. Gov. Printing Office, Wash., D.C. NOAA Atlas NESDIS 51, 286pp., 2002.
- [66] R. A. Locarnini, A. V. Mishonov, J. I. Antonov, T. P. Boyer, and H. E. Garcia. *World Ocean Atlas 2005, Volume 1: Temperature. S. Levitus, Ed.* U.S. Gov. Printing Office, Wash., D.C. NOAA Atlas NESDIS 61, 182pp., 2006.
- [67] Y. Lu, D. G. Wright, and I. Yashayaev. Modelling hydrographic changes in the labrador sea over the past five decades. *Progress in Oceanography*, 73(34):406–426, 2007.

- [68] W. Ludwig, J.-L. Probst, and S. Kempe. Predicting the oceanic input of organic carbon by continental erosion. *Global Biogeochemical Cycles*, 10(1):23–41, 1996.
- [69] G. Madec. NEMO ocean engine. *Note du Pole de modelisation, Institut Pierre-Simon Laplace (IPSL), France*, 27:1288–1619, 2008.
- [70] N. Mahowald, T. D. Jickells, A. R. Baker, P. Artaxo, C. R. Benitez-Nelson, G. Bergametti, T. C. Bond, Y. Chen, D. D. Cohen, B. Herut, N. Kubilay, R. Losno, C. Luo, W. Maenhaut, K. A. McGee, G. S. Okin, R. L. Siefert, and S. Tsukuda. Global distribution of atmospheric phosphorus sources, concentrations and deposition rates, and anthropogenic impacts. *Global Biogeochemical Cycles*, 22(4):GB4026, 2008.
- [71] J. Marshall, Y. Kushnir, D. Battisti, P. Chang, A. Czaja, R. Dickson, J. Hurrell, M. McCartney, R. Saravanan, and M. Visbeck. North atlantic climate variability: Phenomena, impacts and mechanisms. *International Journal of Climatology*, 21(15):1863–1898, 2001.
- [72] V. Martin-Jézéquel, M. Hildebrand, and M. A. Brzezinski. Silicon metabolism in diatoms: Implications for growth. *Journal of Phycology*, 36(5):821–840, 2000.
- [73] T. R. Martz, M. D. DeGrandpre, P. G. Stratton, W. R. McGillis, and W. M. Drennan. Sea surface pCO₂ and carbon export during the Labrador Sea spring-summer bloom: An in situ mass balance approach. *Journal of Geophysical Research: Oceans*, 114(C9):C09008, 2009.

- [74] I. Masotti, D. Ruiz Pino, and A. Le Bouteiller. Photosynthetic characteristics of *Trichodesmium* in the southwest Pacific Ocean : importance and significance. *Marine Ecology Progress Series*, 338:47–59, 2007.
- [75] J. J. McCarthy. The kinetics of nutrient utilization. In *Canadian Bulletin of Fisheries and Aquatic Sciences*, number 210, pages 211–233. Department of Fisheries and Oceans, 1981.
- [76] C. McClain, M. Cleave, G. Feldman, W. Gregg, S. Hooker, and N. Kuring. Science quality SeaWiFS data for global biosphere research. *Sea Technology*, 39(9):10–16, 1998.
- [77] T. J. McDougall and P. M. Barker. *Getting started with TEOS-10 and the Gibbs Seawater (GSW) Oceanographic Toolbox*. SCOR/IAPSO WG127. ISBN:978-0-646-55621-5., 28pp., 2011.
- [78] N. Metzl, A. Corbire, G. Reverdin, A. Lenton, T. Takahashi, A. Olsen, T. Johannessen, D. Pierrot, R. Wanninkhof, S. R. Iafsdttir, J. Olafsson, and M. Ramonet. Recent acceleration of the sea surface $f\text{CO}_2$ growth rate in the North Atlantic subpolar gyre (1993–2008) revealed by winter observations. *Global Biogeochemical Cycles*, 24(4):GB4004, 2010.
- [79] M. Meybeck. Riverine transport of atmospheric carbon: Sources, global typology and budget. *Water, Air, and Soil Pollution*, 70(1-4):443–463, 1993.
- [80] J. J. Middelburg, K. Soetaert, P. M. J. Herman, and C. H. R. Heip. Denitrification in marine sediments: A model study. *Global Biogeochemical Cycles*, 10(4):661–673, 1996.

- [81] S. E. Mikaloff Fletcher, N. Gruber, A. R. Jacobson, S. C. Doney, S. Dutkiewicz, M. Gerber, M. Follows, F. Joos, K. Lindsay, D. Menemenlis, A. Mouchet, S. A. Mller, and J. L. Sarmiento. Inverse estimates of anthropogenic CO₂ uptake, transport, and storage by the ocean. *Global Biogeochemical Cycles*, 20(2):GB2002, 2006.
- [82] M. M. Mills, C. Ridame, M. Davey, J. La Roche, and R. J. Geider. Iron and phosphorus co-limit nitrogen fixation in the eastern tropical North Atlantic. *Nature*, 429(6989):292–294, 2004.
- [83] J. Monod. *Recherche sur la croissance des cultures bactériennes*, pages 184–204. Actualités scientifiques et industrielles. Hermann, 1959.
- [84] J. K. Moore, S. C. Doney, J. A. Kleypas, D. M. Glover, and I. Y. Fung. An intermediate complexity marine ecosystem model for the global domain. *Deep Sea Research Part II: Topical Studies in Oceanography*, 49(1):403–462, 2001.
- [85] J. K. Moore, S. C. Doney, and K. Lindsay. Upper ocean ecosystem dynamics and iron cycling in a global three-dimensional model. *Global Biogeochemical Cycles*, 18(4):GB4028, 2004.
- [86] A. Morel. Optical modeling of the upper ocean in relation to its biogenous matter content (case I waters). *Journal of Geophysical Research: Oceans*, 93(C9):10749–10768, 1988.
- [87] R. Myers, J. Helbig, and D. Holland. Seasonal and interannual variability of the Labrador Current and West Greenland Current. Technical report, ICES. 10pp., 1989.

- [88] M. C. Nielsdttir, C. M. Moore, R. Sanders, D. J. Hinz, and E. P. Achterberg. Iron limitation of the postbloom phytoplankton communities in the iceland basin. *Global Biogeochemical Cycles*, 23(3):GB3001, 2009.
- [89] P. D. Nightingale, G. Malin, C. S. Law, A. J. Watson, P. S. Liss, M. I. Liddicoat, J. Boutin, and R. C. Upstill-Goddard. In situ evaluation of air-sea gas exchange parameterizations using novel conservative and volatile tracers. *Global Biogeochemical Cycles*, 14(1):373–387, 2000.
- [90] N. Oceanic and A. Administration. *Data Announcement 88-MGG-02, Digital relief of the Surface of the Earth*. National Geophysical Data Center, Boulder, Colorado, 1988. <http://www.ngdc.noaa.gov>.
- [91] R. V. O’Neill, D. L. DeAngelis, J. J. Pastor, B. J. Jackson, and W. M. Post. Multiple nutrient limitations in ecological models. *Ecological Modelling*, 46(34):147–163, 1989.
- [92] P. Parekh, M. J. Follows, and E. A. Boyle. Decoupling of iron and phosphate in the global ocean. *Global Biogeochemical Cycles*, 19(2):GB2020, 2005.
- [93] B. J. Peterson, J. McClelland, R. Curry, R. M. Holmes, J. E. Walsh, and K. Aagaard. Trajectory shifts in the arctic and subarctic freshwater cycle. *Science*, 313(5790):1061–1066, 2006.
- [94] J. R. Petit, J. Jouzel, D. Raynaud, N. I. Barkov, J.-M. Barnola, I. Basile, M. Bender, J. Chappellaz, M. Davis, G. Delaygue, M. Delmotte, V. M. Kotlyakov, M. Legrand, V. Y. Lipenkov, C. Lorius, L. Ppin, C. Ritz, E. Saltz-

- man, and M. Stievenard. Climate and atmospheric history of the past 420,000 years from the Vostok ice core, Antarctica. *Nature*, 399(6735):429–436, 1999.
- [95] B. Petrie. The cold intermediate layer on the Labrador and northeast Newfoundland shelves, 1978–86. *Northwest Atl. Fish. Organ. Sci. Council. Stud.*, 12:57–69, 1988.
- [96] R. Pickart, M. Spall, and J. Lazier. Mid-depth ventilation in the western boundary current system of the sub-polar gyre. *Deep Sea Research Part I: Oceanographic Research Papers*, 44(6):1025–1054, 1997.
- [97] G. K. Plattner, F. Joos, T. F. Stocker, and O. Marchal. Feedback mechanisms and sensitivities of ocean carbon uptake under global warming. *Tellus B*, 53(5):564–592, 2001.
- [98] P. Pondaven, C. Fravallo, D. Ruiz-Pino, P. Trguer, B. Quiguiner, and C. Jeandel. Modelling the silica pump in the permanently open ocean zone of the southern ocean. *Journal of Marine Systems*, 17(14):587–619, 1998.
- [99] J. A. Raven and P. G. Falkowski. Oceanic sinks for atmospheric CO₂. *Plant, Cell & Environment*, 22(6):741–755, 1999.
- [100] T. H. Reynaud, A. J. Weaver, and R. J. Greatbatch. Summer mean circulation of the northwestern Atlantic ocean. *Journal of Geophysical Research: Oceans*, 100(C1):779–816, 1995.
- [101] M. Rhein. Drifters reveal deep circulation. *Nature*, 407(6800):30–31, 2000.

- [102] M. Rhein, W. Smethie, D. Smythe-Wright, R. Weiss, and C. Mertens. Labrador sea water: Pathways, cfc inventory, and formation rates. *Journal of Physical Oceanography*, 32(2):648–665, 2002.
- [103] C. Ridame and C. Guieu. Saharan input of phosphate to the oligotrophic water of the open western Mediterranean Sea. *Limnology and Oceanography*, 47(3):856–869, 2002.
- [104] A. J. Ridgwell, A. J. Watson, and D. E. Archer. Modeling the response of the oceanic Si inventory to perturbation, and consequences for atmospheric CO₂. *Global Biogeochemical Cycles*, 16(4):1071, 2002.
- [105] C. Rodenbeck, T. J. Conway, and R. L. Langenfelds. The effect of systematic measurement errors on atmospheric CO₂ inversions: a quantitative assessment. *Atmospheric Chemistry and Physics*, 6:149–161, 2006.
- [106] J. Ryther and C. Yentsch. The estimation of phytoplankton production in the ocean from chlorophyll and light data. *Limnology and Oceanography*, 2:281–286, 1957.
- [107] C. Sabine, A. Kozyr, and Carbon Dioxide Information Analysis Center (U.S.) and United States. Dept. of Energy. Climate Change Research Division and Pacific Marine Environmental Laboratory (U.S.) and Princeton University. Department of Geosciences and Atlantic Oceanographic and Meteorological Laboratories and Rosenstiel School of Marine and Atmospheric Science. *Global Ocean Data Analysis Project (GLODAP): Results and Data*. Contribution (Pacific Marine Environmental Laboratory). Oak Ridge National Laboratory. 81pp., 2005.

- [108] J. Sarmiento and N. Gruber. *Ocean biogeochemical dynamics*. Princeton University Press. 528pp., 2006.
- [109] J. Sarmiento and C. Le Quéré. Oceanic carbon dioxide uptake in a model of century-scale global warming. *Science*, (274):1346–1350, 1996.
- [110] G. Sarthou, K. R. Timmermans, S. Blain, and P. Treguer. Growth physiology and fate of diatoms in the ocean: a review. *Journal of Sea Research*, 53(1-2):25–42, 2005.
- [111] U. Schuster, A. Hannides, L. Mintrop, and A. Körtzinger. Sensors and instruments for oceanic dissolved carbon measurements. *Ocean Science*, 5:547–558, 2009.
- [112] U. Schuster, G. A. McKinley, N. Bates, F. Chevallier, S. C. Doney, A. R. Fay, M. Gonzalez-Davila, N. Gruber, S. Jones, J. Krijnen, P. Landschuetzer, N. Lefevre, M. Manizza, J. Mathis, N. Metzl, A. Olsen, A. F. Rios, C. Roedenbeck, J. M. Santana-Casiano, T. Takahashi, R. Wanninkhof, and A. J. Watson. An assessment of the Atlantic and Arctic sea-air CO₂ fluxes, 1990-2009. *Biogeosciences*, 10(1):607–627, 2013.
- [113] U. Schuster and A. J. Watson. A variable and decreasing sink for atmospheric CO₂ in the North Atlantic. *Journal of Geophysical Research: Oceans*, 112(C11):C11006, 2007.
- [114] D. A. Siegel, S. C. Doney, and J. A. Yoder. The north atlantic spring phytoplankton bloom and sverdrup’s critical depth hypothesis. *Science*, 296(5568):730–733, 2002.

- [115] K. D. Six and E. Maier-Reimer. Effects of plankton dynamics on seasonal carbon fluxes in an ocean general circulation model. *Global Biogeochemical Cycles*, 10(4):559–583, 1996.
- [116] D. Skoog, D. West, and F. Holler. *Analytical chemistry: an introduction*. Saunders golden sunburst series. Saunders College Pub. 880pp., 2000.
- [117] V. S. Smetacek. Role of sinking in diatom life-history cycles: ecological, evolutionary and geological significance. *Marine Biology*, 84(3):239–251, 1985.
- [118] E. Smith, F. Soule, and O. Mosby. *The Marion and General Green expeditions to Davis Strait and the Labrador Sea*, volume 19. Bull. U.S. Coast Guard. 259pp., 1937.
- [119] S. V. Smith and J. T. Hollibaugh. Coastal metabolism and the oceanic organic carbon balance. *Reviews of Geophysics*, 31(1):75–89, 1993.
- [120] U. Sommer. Nitrate- and silicate-competition among antarctic phytoplankton. *Marine Biology*, 91(3):345–351, 1986.
- [121] L. Stemmann, G. A. Jackson, and G. Gorsky. A vertical model of particle size distributions and fluxes in the midwater column that includes biological and physical processespart ii: application to a three year survey in the NW mediterranean sea. *Deep Sea Research Part I: Oceanographic Research Papers*, 51(7):885–908, 2004.
- [122] F. Straneo. Heat and freshwater transport through the central labrador sea. *Journal of Physical Oceanography*, 36(4):606–628, 2006.

- [123] P. G. Strutton, T. R. Martz, M. D. DeGrandpre, W. R. McGillis, W. M. Drennan, and E. Boss. Bio-optical observations of the 2004 labrador sea phytoplankton bloom. *Journal of Geophysical Research: Oceans*, 116(C11):C11037, 2011.
- [124] R. Sfrian, L. Bopp, M. Gehlen, J. Orr, C. Eth, P. Cadule, O. Aumont, D. Salas y Mlia, A. Voltaire, and G. Madec. Skill assessment of three earth system models with common marine biogeochemistry. *Climate Dynamics*, 40(9-10):2549–2573, 2013.
- [125] V. Tait, R. Gershey, and E. Jones. Inorganic carbon in the labrador sea: Estimation of the anthropogenic component. *Deep Sea Research Part I: Oceanographic Research Papers*, 47(2):295–308, 2000.
- [126] T. Takahashi, J. Olafsson, J. G. Goddard, D. W. Chipman, and S. C. Sutherland. Seasonal variation of CO₂ and nutrients in the high-latitude surface oceans: A comparative study. *Global Biogeochemical Cycles*, 7(4):843–878, 1993.
- [127] T. Takahashi, S. C. Sutherland, R. Wanninkhof, C. Sweeney, R. A. Feely, D. W. Chipman, B. Hales, G. Friederich, F. Chavez, C. Sabine, A. Watson, D. C. E. Bakker, U. Schuster, N. Metzl, H. Yoshikawa-Inoue, M. Ishii, T. Midorikawa, Y. Nojiri, A. Koertzinger, T. Steinhoff, M. Hoppema, J. Olafsson, T. S. Arnarson, B. Tilbrook, T. Johannessen, A. Olsen, R. Bellerby, C. S. Wong, B. Delille, N. R. Bates, and H. J. W. de Baar. Climatological mean and decadal change in

- surface ocean pCO₂, and net sea-air CO₂ flux over the global oceans. *Deep Sea Research Part II: Topical Studies in Oceanography*, 56(8-10):554–577, 2009.
- [128] S. Takeda. Influence of iron availability on nutrient consumption ratio of diatoms in oceanic waters. *Nature*, 393(6687):774–777, 1998.
- [129] T. Tanaka and F. Rassoulzadegan. Vertical and seasonal variations of bacterial abundance and production in the mesopelagic layer of the NW Mediterranean Sea: bottom-up and top-down controls. *Deep-Sea Research Part I-Oceanographic Research Papers*, 51(4):531–544, 2004.
- [130] I. Tegen and I. Fung. Contribution to the atmospheric mineral aerosol load from land surface modification. *Journal of Geophysical Research: Atmospheres*, 100(D9):18707–18726, 1995.
- [131] T. F. Thingstad and R. Lignell. Theoretical models for the control of bacterial growth rate, abundance, diversity and carbon demand. *Aquatic Microbial Ecology*, 13(1):19–27, 1997.
- [132] K. Thompson, Y. Lu, and E. Demirov. A simple method for reducing seasonal bias and drift in eddy resolving ocean models. *Ocean modelling*, 14(1-2):122–138, 2006.
- [133] R. C. Tian, D. Deibel, R. B. Rivkin, and A. F. Vzina. Biogenic carbon and nitrogen export in a deep-convection region: simulations in the labrador sea. *Deep Sea Research Part I: Oceanographic Research Papers*, 51(3):413–437, 2004.

- [134] P. Trguer, D. M. Nelson, A. J. Van Bennekom, D. J. DeMaster, A. Leynaert, and B. Quguiner. The silica balance in the world ocean: A reestimate. *Science*, 268(5209):375–379, 1995.
- [135] D. J. Ullman, G. A. McKinley, V. Bennington, and S. Dutkiewicz. Trends in the North Atlantic carbon sink: 1992-2006. *Global Biogeochemical Cycles*, 23:GB4011, 2009.
- [136] B. A. S. Van Mooy, R. G. Keil, and A. H. Devol. Impact of suboxia on sinking particulate organic carbon: Enhanced carbon flux and preferential degradation of amino acids via denitrification. *Geochimica Et Cosmochimica Acta*, 66(3):457–465, 2002.
- [137] T. Volk and M. I. Hoffert. Ocean carbon pumps: Analysis of relative strengths and efficiencies in ocean-driven atmospheric CO₂ changes. *Geophysical Monograph Series*, 32:99–110, 1985.
- [138] T. Wagener, C. Guieu, and N. Leblond. Effects of dust deposition on iron cycle in the surface Mediterranean Sea: results from a mesocosm seeding experiment. *Biogeosciences*, 7(11):3769–3781, 2010.
- [139] R. Wanninkhof. Relationship between wind speed and gas exchange over the ocean. *Journal of Geophysical Research: Oceans*, 97(C5):7373–7382, 1992.
- [140] R. Wanninkhof and W. R. McGillis. A cubic relationship between air-sea CO₂ exchange and wind speed. *Geophysical Research Letters*, 26(13):1889–1892, 1999.

- [141] D. A. Wolf-Gladrow, R. E. Zeebe, C. Klaas, A. Krtzinger, and A. G. Dickson. Total alkalinity: The explicit conservative expression and its application to biogeochemical processes. *Marine Chemistry*, 106(12):287–300, 2007.
- [142] I. Yashayaev. Hydrographic changes in the labrador sea, 1960-2005. *Progress In Oceanography*, 73(3-4):242–276, 2007.
- [143] J. Yoder, J. Moore, and R. Swift. Putting together the big picture: Remote-sensing observations of ocean color. *Oceanography*, 14(4):33–40, 2001.
- [144] J. P. Zehr. Nitrogen fixation by marine cyanobacteria. *Trends in Microbiology*, 19(4):162–173, 2011.
- [145] J. Zhu and E. Demirov. On the mechanism of interannual variability of the irmingier water in the labrador sea. *Journal of Geophysical Research: Oceans*, 116(C3):C03014, 2011.
- [146] J. Zhu, E. Demirov, F. Dupont, and D. Wright. Eddy-permitting simulations of the sub-polar north atlantic: impact of the model bias on water mass properties and circulation. *Ocean Dynamics*, 60(5):1177–1192, 2010.
- [147] I. Zondervan. The effects of light, macronutrients, trace metals and CO₂ on the production of calcium carbonate and organic carbon in coccolithophores - A review. *Deep-Sea Research Part II-Topical Studies in Oceanography*, 54(5-7):521–537, 2007.

Appendix A

PISCES

A.1 Model Equations

In the following, the source-minus-sink (SMS) equations for all model state variables are described briefly. Each term on the equations is associated with an underbrace ($\underbrace{\quad}$) which describes its functional process. All parameters and their default values are listed in Table A.2 of Section A.4.

A.1.1 Nanophytoplankton

$$\begin{aligned} SMS(P) = & \underbrace{(1 - \delta^P)\mu^P P}_{NPP} - \underbrace{m^P \frac{P}{K_P + P} P}_{Mortality} - \underbrace{(sh)w^P P^2}_{Aggregation} \\ & - \underbrace{(g^Z(P)Z + g^M(P)M)}_{Grazing} \end{aligned} \quad (A.1)$$

The first term is the net primary production (NPP), which equals the gross primary production (GPP) minus exudation. δ^P denotes the exudation rate, m^P is the excretion rate, K_m is the half-saturation constant for mortality, and w^P is the aggregation

rate of nanophytoplankton. The productivity of nanophytoplankton depends on several factors, including seawater temperature, mixed layer depth, light availability, and external nutrients concentrations:

$$\mu^P = \mu_P g(Z_{mixl}) f(L_{day}) \left[1 - \exp\left(\frac{-\alpha^P \theta^{chl,P} PAR^P}{L_{day}(\mu_{ref} + b_{resp})}\right) \right] L_{lim}^P \quad (\text{A.2})$$

$$\mu_P = \mu_{max}^0 b_P^T \quad (\text{A.3})$$

where μ_{max}^0 is the maximum growth rate at 0°C and b_P^T is the temperature (T) sensitivity for growth. From Equation A.2, b_{resp} is the respiration rate, μ_{ref} is the reference growth rate, L_{day} is the day length, and Z_{mixl} is the mixed layer depth. $f(L_{day})$ and $g(Z_{mixl})$ impose the dependency of growth rate to the day length and the mixed layer depth, respectively:

$$f(L_{day}) = 1.5 \frac{L_{day}}{0.5 + L_{day}} \quad (\text{A.4})$$

$$\Delta Z = \max(0, Z_{mixl} - Z_{eu}) \quad (\text{A.5})$$

$$T_{dark} = \frac{(\Delta Z)^2}{86400} \quad (\text{A.6})$$

$$g(Z_{mixl}) = 1 - \frac{T_{dark}}{T_{dark}^P + T_{dark}} \quad (\text{A.7})$$

where Z_{eu} is the euphotic layer depth, T_{dark} is the mean residence time of phytoplankton below the euphotic zone, T_{dark}^P is the reference residence time of nanophytoplankton, and ΔZ defines the thickness of the unlit part of the mixed layer.

$$\mu^P = a e^{bT} \left(1 - e^{-\frac{\alpha^P (\frac{chl}{C})^P PAR^P}{\mu_P L_{lim}^P}} \right) L_{lim}^P \quad (\text{A.8})$$

where the limitation terms for nutrients are defined by:

$$L_{PO_4}^P = \frac{PO_4}{K_{PO_4}^P + PO_4} \quad (\text{A.9})$$

$$L_{Fe}^P = \min(1, \max(0, \frac{\theta^{Fe,P} - \theta_{min}^{Fe,P}}{\theta_{opt}^{Fe,P}})) \quad (\text{A.10})$$

$$L_{NO_3}^P = \frac{K_{NH_4}^P NO_3}{K_{NO_3}^P K_{NH_4}^P + K_{NH_4}^P NO_3 + K_{NO_3}^P NH_4} \quad (\text{A.11})$$

$$L_{NH_4}^P = \frac{K_{NO_3}^P NH_4}{K_{NO_3}^P K_{NH_4}^P + K_{NH_4}^P NO_3 + K_{NO_3}^P NH_4} \quad (\text{A.12})$$

$$L_{lim}^P = \min(L_{PO_4}^P, L_{Fe}^P, L_{NO_3}^P + L_{NH_4}^P) \quad (\text{A.13})$$

where $\theta_{opt}^{Fe,P}$ is the optimal quota for iron. The half-saturation constant for each limiting nutrient on nanophytoplankton growth (K_i^P where $i = PO_4, NH_4, NO_3$) is a function of its biomass:

$$P_1 = \min(P, P_{max}) \quad (\text{A.14})$$

$$P_2 = \max(0, P - P_{max}) \quad (\text{A.15})$$

$$K_i^P = K_i^{P,min} \frac{P_1 + S_{rat}^P P_2}{P_1 + P_2} \quad (\text{A.16})$$

where P_{max} is the maximum threshold for nanophytoplankton concentration, S_{rat}^P is the size ratio of diatoms to nanophytoplankton, and $K_i^{P,min}$ is the half-saturation constant of nanophytoplankton.

The vertical attenuation of photosynthetically available radiation (PAR) is computed using a simplified version of the full spectral model of *Morel* (1988) [86]:

$$PAR_1(0) = PAR_2(0) = PAR_3(0) = \frac{\rho_{par} SW}{3} \text{ at } z = 0m \quad (\text{A.17})$$

where $PAR_1(0)$, $PAR_2(0)$, and $PAR_3(0)$ are the blue (400-500 nm), green (500-600 nm), and red (600-700 nm) parts of visible light at the sea surface, respectively. ρ_{par} denotes the fraction of solar radiation (SW). Below the sea surface, PAR is computed as follows:

$$PAR^P(z) = \beta_1^P PAR_1(z) + \beta_2^P PAR_2(z) + \beta_3^P PAR_3(z) \quad (\text{A.18})$$

where z is the vertical depth and β_i^P ($i=1,2,3$) is the light absorption coefficient which depends on the waveband and on the phytoplankton species.

The nanophytoplankton aggregation term w^P depends on the shear rate (sh) as the main driving force for aggregation is the local turbulence. This shear rate is set to 1 s^{-1} in the mixed layer and to 0.01 s^{-1} below.

The new and regenerated productions by nitrate and ammonium respectively, are computed as follows [91]:

$$\begin{aligned}\mu_{no3}^P &= \mu^P \frac{L_{no3}^P}{L_{no3}^P + L_{nh4}^P} \\ \mu_{nh4}^P &= \mu^P \frac{L_{nh4}^P}{L_{no3}^P + L_{nh4}^P}\end{aligned}\tag{A.19}$$

A.1.2 Diatoms

$$\begin{aligned}SMS(D) &= \underbrace{(1 - \delta^D)\mu^D D}_{NPP} - \underbrace{m^D \frac{D}{K_m + D} D}_{Mortality} - \underbrace{(sh)w^D D^2}_{Aggregation} \\ &\quad - \underbrace{(g^Z(D)Z + g^M(D)M)}_{Grazing}\end{aligned}\tag{A.20}$$

The diatoms production term is defined as for nanophytoplankton (Equation A.8) except that the limitation terms also include silicate:

$$\begin{aligned}L_{Si}^D &= \frac{Si}{K_{Si}^D + Si} \\ L_{lim}^D &= \min(L_{po4}^D, L_{Fe}^D, L_{no3}^D + L_{nh4}^D, L_{Si}^D)\end{aligned}\tag{A.21}$$

As for iron, the silicate half-saturation constant exhibits significant spatial variability [120, 72]. The following relationship can be inferred when plotted against maximum local yearly silicate concentration (Si_{max}) [98]:

$$K_{Si}^D = K_{Si}^{D,min} + \frac{7Si_{max}^2}{K_{Si}^2 + Si_{max}^2}\tag{A.22}$$

where $K_{Si}^{D,min}$ is the minimum half-saturation constant for silicate on diatoms growth.

The diatoms aggregation term (w_p^D) is increased in case of nutrient limitation since it has been shown that diatoms cells tend to excrete a mucus which increase their stickiness, leading to a more efficient aggregation [117, 16]:

$$w_p^D = w^P + w_{max}^D(1 - L_{lim}^D) \quad (\text{A.23})$$

A.1.3 Chlorophyll in nanophytoplankton and diatoms

The chlorophyll content in nanophytoplankton and diatoms are parameterized based on the photoadaptative model of *Geider et al.* (1998) [37]:

$$\begin{aligned} SMS(I^{Chl}) = & \underbrace{\rho_{Chl}^I(1 - \delta^I)(12\theta_{min}^{Chl,I} + (\theta_{max}^{Chl,I} - \theta_{min}^{Chl,I})\rho^{I^{Chl}})\mu^I I}_{NPP} - \underbrace{m^I \frac{I}{K_m + I} I^{Chl}}_{Mortality} \\ & - \underbrace{(sh)w^I I I^{Chl}}_{Aggregation} - \underbrace{\theta^{Chl,I}(g^Z(I)Z + g^M(I)M)}_{Grazing} \end{aligned} \quad (\text{A.24})$$

where I is the phytoplankton class (either P or D), $\theta^{Chl,I}$ is the chlorophyll-to-carbon ratio of the considered phytoplankton type. $\rho^{I^{Chl}}$ denotes the ratio of energy assimilated to energy absorbed. Following *Geider et al.* (1996) [36], this is defined as:

$$\rho^{I^{Chl}} = \frac{144\check{\mu}^I I}{\alpha^I I^{Chl} \frac{PAR}{L_{day}}} \quad (\text{A.25})$$

$$\check{\mu}^I = \mu_P g(Z_{mix})(1 - \exp(\frac{-\alpha^I \theta^{Chl,I} PAR^I}{L_{day} \mu_P L_{lim}^I})) L_{lim}^I \quad (\text{A.26})$$

where 144 refers to the square of the molar mass of carbon and is used to convert from mol to mg as the standard unit for chlorophyll is generally in mg/m^3 .

A.1.4 Iron in nanophytoplankton and diatoms

The iron content of phytoplankton I^{Fe} is computed as follows:

$$\begin{aligned}
 SMS(I^{Fe}) = & \underbrace{(1 - \delta^I)\mu^{I^{Fe}} I}_{NPP} - \underbrace{m^I \frac{I}{K_m + I} I^{Fe}}_{Mortality} \\
 & - \underbrace{(sh)w^I I I^{Fe}}_{Aggregation} - \underbrace{\theta^{Fe,I}(g^Z(I)Z + g^M(I)M)}_{Grazing}
 \end{aligned} \tag{A.27}$$

where $\theta^{Fe,I}$ is the iron-to-carbon ratio in phytoplankton. The growth rate ($\mu^{I^{Fe}}$) is parameterized as follows:

$$\mu^{I^{Fe}} = \theta_{max}^{Fe,I} L_{lim,1}^{I^{Fe}} L_{lim,2}^{I^{Fe}} \frac{1 - \frac{\theta^{Fe,I}}{\theta_{max}^{Fe,I}}}{1.05 - \frac{\theta^{Fe,I}}{\theta_{max}^{Fe,I}}} \mu_P \tag{A.28}$$

where $\theta_{max}^{Fe,I}$ is the maximum iron-to-carbon ratio. $L_{lim,1}^{I^{Fe}}$ is the iron limitation term defined as:

$$L_{lim,1}^{I^{Fe}} = \frac{bFe}{bFe + K_{Fe}^{I^{Fe}}} \tag{A.29}$$

$$K_{Fe}^{I^{Fe}} = K_{Fe}^{I^{Fe},min} \frac{I_1 + S_{rat}^I I_2}{I_1 + I_2} \tag{A.30}$$

$$I_2 = \max(0, I - I_{max}) \tag{A.31}$$

$$I_1 = I - I_2 \tag{A.32}$$

where bFe is the bioavailable iron concentration which is defined in Section A.1.19. $K_{Fe}^{I^{Fe},min}$ is the minimum half-saturation constant for iron content of the considered phytoplankton type, I_{max} is the threshold concentration for size dependency, and S_{rat}^I is the size ratio of phytoplankton. $L_{lim,2}^{I^{Fe}}$ accounts for an additional limitation on iron biomass growth due to surge uptake, as observations have revealed that iron uptake was enhanced for some species at low iron concentrations [42, 24]. In PISCES,

this is parameterized as:

$$L_{lim,2}^{I^{Fe}} = \frac{4 - 4.5L_{Fe}^I}{L_{Fe}^I + 0.5} \quad (\text{A.33})$$

The minimum iron-to-carbon ratio is defined as the demands for iron that are required for photosynthesis, respiration, and nitrate/nitrite reduction. The parameterization follows the work done by *Flynn and Hipkin* (1999) [31]:

$$\theta_{min}^{Fe,I} = \frac{0.0016}{55.85} \theta^{chl,I} + \frac{1.21 \times 10^{-5} \times 14 \times L_N^P}{55.85 \times 7.625} \times 1.5 + \frac{1.15 \times 10^{-4} \times 14}{55.85 \times 7.625} L_{NO_3}^P \quad (\text{A.34})$$

where the three terms in the equation correspond to photosynthesis, respiration, and nitrate/nitrite reduction, in the order of appearance.

A.1.5 Silicon in diatoms

$$\begin{aligned} SMS(D_{Si}) = & \underbrace{\theta_{opt}^{Si,D} (1 - \delta^D) \mu^D D}_{NPP} - \underbrace{m^D \frac{D}{K_m + D} D^{Si}}_{Mortality} \\ & - \underbrace{(sh) w^D D D^{Si}}_{Aggregation} - \underbrace{\theta^{Si,D} (g^Z(D) Z + g^M(D) M)}_{Grazing} \end{aligned} \quad (\text{A.35})$$

The silicon-to-carbon ratio ($\theta_{opt}^{Si,D}$) is diagnostically computed as it has been observed to vary by a factor of about 4 to 5 over the global ocean with a mean value of 0.14 ± 0.13 *molSi/molC* [110]. Heavier silification occurs in case of light, nitrogen, phosphorous, or iron stress (e.g. [128, 33, 72]) possibly due to the physiological adaptation of the silicon uptake by phytoplankton, depending on the growth rate and on the G2 cycle phase in which silicon is incorporated [72, 11]. On the other hand, lighter silification can only result from silicate limitation. Following these remarks, the variations of the Si/C ratio is parameterized using the method proposed by *Bucciarelli et al.* (2002,

unpublished manuscript):

$$\theta_{opt}^{Si,D} = \theta_m^{Si,D} L_{lim,1}^{D^{Si}} \min[5.4, (4.4e^{-4.23F_{lim,1}^{D^{Si}}} F_{lim,2}^{D^{Si}} + 1)(1 + 2L_{lim,2}^{D^{Si}})] \quad (\text{A.36})$$

$$F_{lim,1}^{D^{Si}} = \min\left(\frac{\mu^D}{\mu_P L_{min}^D}, L_{PO_4}^D, L_N^D, L_{Fe}^D\right) \quad (\text{A.37})$$

$$F_{lim,2}^{D^{Si}} = \min[1, 2.2 \max(0, L_{lim,1}^{D^{Si}} - 0.5)] \quad (\text{A.38})$$

$$L_{lim,1}^{D^{Si}} = \frac{Si}{Si + K_{Si}^1} \quad (\text{A.39})$$

$$L_{lim,2}^{D^{Si}} = \begin{cases} \frac{Si^3}{Si^3 + (K_{Si}^2)^3} & \text{if } \phi < 0 \\ 0 & \text{if } \phi > 0 \end{cases} \quad (\text{A.40})$$

A.1.6 Microzooplankton

$$\begin{aligned} SMS(Z) = & \underbrace{e^Z (g_P^Z + g^Z(D) + g^Z(POC))Z}_{\text{Grazing}} - \underbrace{m^Z f_Z(T)Z^2}_{\text{Mortality}} \\ & - \underbrace{r^Z f_Z(T) \left(\frac{Z}{K_m + Z} + 3\Delta(O_2) \right) Z}_{\text{Mortality/Excretion}} \end{aligned} \quad (\text{A.41})$$

As for phytoplankton growth, the grazing rate of zooplankton depends exponentially on temperature:

$$g_m^Z = g_{max}^{0,Z} f_Z(T) \quad (\text{A.42})$$

$$f_Z(T) = b_Z^T \quad (\text{A.43})$$

In the above equation, $g_{max}^{0,Z}$ represents the maximum grazing rate and b_Z^T is the temperature sensitivity term for grazing where T denotes the temperature.

Grazing on each food resource I is defined following the Michaelis-Menten parameterization with no switching and a threshold (F_{thresh}^Z) [38]:

$$F = \sum_J p_J^Z \max(0, J - J_{thresh}^Z) \quad (\text{A.44})$$

$$F_{lim} = \max(0, F - F_{thresh}^Z) \quad (\text{A.45})$$

$$g_I^Z = g_m^Z \left(\frac{F_{lim}}{F} \right) \frac{p_I^Z \max(0, I - I_{thresh}^Z)}{K_G^Z + \sum_J p_J^Z J} \quad (\text{A.46})$$

where J denotes all the resources microzooplankton can graze on (i.e. P , D , and POC) and p_J^Z is the preference microzooplankton has for J .

Growth efficiency of microzooplankton (e^Z) depends on the food quality:

$$e_N^Z = e_{max}^Z \min\left(1, \frac{\sum_I p_I^Z \theta^{N,I} I}{\theta^{N,C} \sum_I p_I^Z I}\right) \quad (\text{A.47})$$

$$\theta^{N,I} = \begin{cases} \theta^{N,C} \min\left(1, 0.5 + 0.5 \frac{L_N^I L_{lim}^I \mu_P}{\mu^I}\right) & \text{if } I \in \{P, D\} \\ \theta^{N,C} & \text{if } I = POC \end{cases} \quad (\text{A.48})$$

$$e^Z = e_N^Z \min\left(1, \frac{\sum_I \theta^{Fe,I} g^Z(I)}{\theta^{Fe,Z} \sum_I g^Z(I)}\right) \quad (\text{A.49})$$

where e_{max}^Z denotes the maximum growth efficiency of microzooplankton. Hence, e^Z decreases as food quality of their preys deteriorates (i.e. either $\theta^{Fe,I}$ or $\theta^{N,I}$ of phytoplankton is reduced).

A.1.7 Mesozooplankton

$$\begin{aligned} SMS(M) = & \underbrace{e^M (g^M(P) + g^M(D) + g^M(Z) + g^M(POC) + g_{FF}^M(GOC)) M}_{\text{Grazing}} \\ & - \underbrace{r^M f_M(T) \left(\frac{M}{K_m + M} + 3\Delta(O_2) \right) M}_{\text{Mortality/Excretion}} - \underbrace{m^M f_M(T) M^2}_{\text{Predation}} \end{aligned} \quad (\text{A.50})$$

In addition to the grazing parameterization which depends primarily on food concentrations, PISCES considers flux feeding, which has a potential impact on the fate of sinking particles below the euphotic layer [22, 121]. In PISCES, only the largest

particles are consumed by mesozooplankton via flux feeding as they are the fastest sinking particles:

$$g_{FF}^M(GOC) = g_{FF}^M f_M(T) w^{GOC} GOC \quad (\text{A.51})$$

where g_{FF}^M is the flux feeding rate of mesozooplankton.

The predation term in Equation A.50 is a sink for mesozooplankton due to grazing by the higher, non-resolved trophic levels.

A.1.8 Dissolved organic carbon

$$\begin{aligned} SMS(DOC) = & \underbrace{\delta^P \mu^P P + \delta^D \mu^D D}_{\text{Exudation}} + \underbrace{\lambda_{POC}^* POC}_{\text{Degradation}} - \underbrace{(Remin + Denit)}_{\text{Remineralization}} \\ & + \underbrace{(1 - \gamma^Z)(1 - e^Z - \sigma^Z) \sum_N g^Z(N) Z + (1 - \gamma^M)(1 - e^M - \sigma^M)}_{\text{SloppyFeeding}} \\ & - \underbrace{\left(\sum_N g^M(N) + g_{FF}^M(GOC) \right) M}_{\text{SloppyFeeding}} - \underbrace{(\Phi_1^{DOC} + \Phi_2^{DOC} + \Phi_3^{DOC})}_{\text{Aggregation}} \quad (\text{A.52}) \end{aligned}$$

where σ^I denotes the fraction of ingested food which is used for fecal pellets production. $(1 - e^I - \sigma^I)$ refers to non-ingested part of grazing, known as sloppy feeding. A fraction $(1 - \gamma^I)$ of sloppy feeding produces DOC. N includes all tracers zooplankton can graze on.

Remineralization of semi-labile DOC is parameterized as follows:

$$Remin = \min\left(\frac{O_2}{O_2^{ut}}, \lambda_{DOC} f_P(T) (1 - \Delta(O_2)) L^{bact} \frac{Bact}{Bact_{ref}} DOC\right) \quad (\text{A.53})$$

$$Denit = \min\left(\frac{NO_3}{r_{NO_3}^*}, \lambda_{DOC} f_P(T) \Delta(O_2) L^{bact} \frac{Bact}{Bact_{ref}} DOC\right) \quad (\text{A.54})$$

where λ_{DOC} is the remineralization rate. Remineralization can occurs under both oxic ($Remin$) and anoxic ($Denit$) conditions, which are determined by $\Delta(O_2)$, which is

defined in Equation A.90. It has been suggested that remineralization may be limited by nutrients as bacteria may take up nutrients depending on the quality of DOC [39, 131]. Thus, the limitation term for DOC degradation (L_{lim}^{bact}) is parameterized as follows:

$$L^{bact} = L_{lim}^{bact} L_{DOC}^{bact} \quad (\text{A.55})$$

$$L_{DOC}^{bact} = \frac{DOC}{DOC + K_{DOC}} \quad (\text{A.56})$$

$$L_{lim}^{bact} = \min(L_{NH_4}^{bact}, L_{PO_4}^{bact}, L_{Fe}^{bact}) \quad (\text{A.57})$$

$$L_{Fe}^{bact} = \frac{bFe}{bFe + K_{Fe}^{bact}} \quad (\text{A.58})$$

$$L_{PO_4}^{bact} = \frac{PO_4}{PO_4 + K_{PO_4}^{bact}} \quad (\text{A.59})$$

$$L_N^{bact} = L_{NO_3}^{bact} + L_{NH_4}^{bact} \quad (\text{A.60})$$

$$L_{NH_4}^{bact} = \frac{K_{NO_3}^{bact} NH_4}{K_{NO_3}^{bact} K_{NH_4}^{bact} + K_{NH_4}^{bact} NO_3 + K_{NO_3}^{bact} NH_4} \quad (\text{A.61})$$

$$L_{NO_3}^{bact} = \frac{K_{NH_4}^{bact} NO_3}{K_{NO_3}^{bact} K_{NH_4}^{bact} + K_{NH_4}^{bact} NO_3 + K_{NO_3}^{bact} NH_4} \quad (\text{A.62})$$

where K_i^{Bact} ($i = NH_4, NO_3, PO_4, Fe$) is the half-saturation constant for DOC remineralization. In PISCES, bacteria is not explicitly modeled:

$$z_{max} = \max(Z_{mix}, Z_{eu}) \quad (\text{A.63})$$

$$Bact = \begin{cases} \min(0.7(Z + 2M), 4\mu\text{mol}/l) & \text{if } z \leq z_{max} \\ Bact(z_{max}) \left(\frac{z_{max}}{z}\right)^{0.683} & \text{Otherwise} \end{cases} \quad (\text{A.64})$$

Here, the bacterial concentration is estimated as $0.7(Z + 2M)$, which decreases with depth below z_{max} according to a power-law function [129, 4].

The aggregation terms (Φ_i^{DOC} , where $i = 1, 2, 3$) are defined as follows:

$$\Phi_1^{DOC} = (sh)(a_1DOC + a_2POC)DOC \quad (\text{A.65})$$

$$\Phi_2^{DOC} = (sh)(a_3GOC)DOC \quad (\text{A.66})$$

$$\Phi_3^{DOC} = (a_4POC + a_5DOC)DOC \quad (\text{A.67})$$

Both turbulence-induced and Brownian aggregation processes are considered for dissolved organic matter.

A.1.9 Small particulate organic carbon

Particulate organic matter (carbon and iron content) is modeled based on two different size-classes: POC for small (1-100 μm) and GOC for bigger (100-5000 μm) organic matter. The temporal evolution of POC is expressed as follows:

$$\begin{aligned} SMS(POC) = & \underbrace{\sigma^Z \sum g^Z(X)Z}_{\text{Egestion}} - \underbrace{(g^Z(POC)Z + g^M(POC)M)}_{\text{Grazing}} \\ & + \underbrace{(1 - 0.5R_{CaCO_3}) \left(m^P \frac{P}{K_m + P} P + w^P P^2 \right)}_{\text{Mortality/Aggregation}} \\ & + \underbrace{0.5m^D \frac{D}{K_m + D} D + r^Z \frac{Z}{K_m + Z} Z + m^Z Z^2}_{\text{Mortality}} + \underbrace{\lambda_{POC}^*(GOC - POC)}_{\text{Degradation}} \\ & - \underbrace{w_{POC} \frac{\partial POC}{\partial z}}_{\text{Sinking}} + \underbrace{(\Phi_1^{DOC} + \Phi_3^{DOC} - \Phi)}_{\text{Aggregation}} \end{aligned} \quad (\text{A.68})$$

where w_{POC} is the sinking speed. The fate of mortality and aggregation of calcifying organism (nanophytoplankton) depends on the calcite production rate (R_{CaCO_3}). In PISCES, 50 % of the dead calcifiers is assumed to form POC where the other half goes to calcite.

The degradation rate λ_{POC}^* depends on temperature, and is reduced under anoxic conditions following *Mooy et al. (2002)* [136]:

$$\lambda_{POC}^* = \lambda_{POC} f_P(T)(1 - 0.45\Delta(O_2)) \quad (\text{A.69})$$

where λ_{POC} is the reference degradation rate for POC.

The aggregation of POC is modeled as follows:

$$\Phi = (sh)a_6POC^2 + (sh)a_7POC(GOC) + a_8POC(GOC) + a_9POC^2 \quad (\text{A.70})$$

where the first two terms refer to turbulent aggregation and the latter two terms correspond to differential settling aggregation.

A.1.10 Big particulate organic carbon

$$\begin{aligned} SMS(GOC) = & \underbrace{\sigma^M \left(\sum_I g^M(I)M + g_{FF}^M(GOC)M \right)}_{Egestion} + \underbrace{r^M \frac{M}{K_m + M} M}_{Mortality} + \underbrace{m^M M^2}_{Predation} \\ & + \underbrace{0.5R_{CaCO_3} \left(m^P \frac{P}{K_m + P} P + w^P P^2 \right)}_{Mortality/Aggregation} + \underbrace{0.5m^D \frac{D}{K_m + D} D}_{Mortality} \\ & + \underbrace{w^D D^2}_{Aggregation} - \underbrace{\lambda_{POC}^* GOC}_{Degradation} - \underbrace{w_{GOC} \frac{\partial GOC}{\partial z}}_{Sinking} + \underbrace{(\Phi_2^{DOC} + \Phi)}_{Aggregation} \quad (\text{A.71}) \end{aligned}$$

Similarly to the formulation for the fate of dead nanophytoplankton, 50 % of diatoms mortality is considered to become GOC, while the other half is transformed into biogenic silica.

Observational studies have shown that the average sinking speed of particulate organic matter increases with depth [8]. Given this fact, the sinking speed of GOC

is formulated, where the parameters are adjusted using a model of *Gehlen et al.* (2006) [35], as follows:

$$Z_{max} = \max(Z_{eu}, Z_{mxl}) \quad (\text{A.72})$$

$$w_{GOC} = \min(w_{GOC}^{min} + (200 - w_{GOC}^{min}) \frac{\max(0, z - Z_{max})}{5000}, w_{max}) \quad (\text{A.73})$$

A.1.11 Small particulate organic iron

The iron content of the particulate organic matter for small size-class is modeled explicitly:

$$\begin{aligned} SMS(SFe) = & \sigma^Z \sum_I \theta^{Fe,I} g^Z(I) Z + \theta^{Fe,Z} (r^Z f_z(T) \frac{Z}{K_m + Z} Z + m^Z f_z(T) Z^2) + \lambda_{GOC}^* BFe \\ & + \theta^{Fe,P} (1 - 0.5 R_{CaCO_3}) (m^P \frac{P}{K_m + P} P + (sh) w^P P^2) + \theta^{Fe,D} 0.5 m^D \frac{D}{K_m + D} \\ & + \lambda_{Fe}(POC) Fe' + Coagfe1 - \lambda_{POC}^* SFe - \theta_{Fe, POC} \Phi - \theta^{Fe, POC} g^M(POC) M \\ & + \kappa_{Bact}^{SFe} Bactfe - \theta^{Fe, POC} g^Z(POC) - w_{POC} \frac{\partial SFe}{\partial z} \end{aligned} \quad (\text{A.74})$$

where λ_{Fe} is the slope of iron scavenging rate, $\theta^{Fe,Z}$ and $\theta^{Fe,POC}$ are the Fe/C ratios for microzooplankton and POC, respectively. The description and formulation of Fe' , $Coagfe1$, and $Bactfe$ will be provided in Section A.1.19.

A.1.12 Big particulate organic iron

The temporal evolution of bigger particulate organic iron is computed in the similar way as POC:

$$\begin{aligned}
SMS(BFe) = & \sigma^M \left[\sum_I \theta^{Fe,I} g^M(I) + {}^t \text{heta} Fe, GOC g_{FF}^M(GOC) \right] M - \lambda_{POC}^* BFe \\
& + \theta^{Fe,M} \left[r^M f_M(T) \frac{M}{K_m + M} M + m^M f_M(T) M^2 \right] - w_{GOC} \frac{\partial BFe}{\partial z} \\
& + \theta^{Fe,D} \left(0.5 m^D \frac{D}{K_m + D} D + (sh) w^D D^2 \right) + \kappa_{Bact}^{BFe} Bact fe \\
& + \lambda_{Fe}(GOC) Fe' + \theta^{Fe,POC} \Phi + Coag fe2 - \theta^{Fe,GOC} g_{FF}^M(GOC) M \\
& + \theta^{Fe,P} 0.5 R_{CaCO_3} \left(m^P \frac{P}{K_m + P} P + (sh) w^P P^2 \right) \quad (A.75)
\end{aligned}$$

Again, all processes by different forms of iron will be discussed in Section A.1.19.

A.1.13 Biogenic silica

Biogenic silica is considered only in the big form, the same size criterion as GOC:

$$\begin{aligned}
SMS(PSi) = & \underbrace{\theta^{Si,D} m^D \frac{D}{K_m + D} D^{Si}}_{Mortality} + \underbrace{(sh) w^D D D^{Si}}_{Aggregation} + \underbrace{\theta^{Si,D} (g^Z(D) Z + g^M(D) M)}_{Grazing} \\
& - \underbrace{\lambda_{PSi}^* (Diss_{Si}) PSi}_{Dissolution} - \underbrace{w_{GOC} \frac{\partial PSi}{\partial z}}_{Sinking} \quad (A.76)
\end{aligned}$$

where the dissolution rate of PSi is parameterized based on *Ridgwell et al. (2002)* [104]:

$$Si_{eq} = 10^{6.44 - \frac{968}{T+273.15}} \quad (A.77)$$

$$Si_{sat} = \frac{Si_{eq} - Si}{Si_{eq}} \quad (A.78)$$

$$\lambda_{PSi}^* = \lambda_{PSi} \left[0.225 \left(1 + \frac{T}{15} \right) Si_{sat} + 0.775 \left(\left(1 + \frac{T}{400} \right)^4 Si_{sat} \right)^9 \right] \quad (A.79)$$

$$\chi = \begin{cases} \chi_{lab}^0 & \text{if } z \leq Z_{max} \\ \chi_{lab}^0 \exp(-(\lambda_{PSi}^{lab} - \lambda_{PSi}^{ref}) \frac{(z - Z_{max})}{w_{GOC}}) & \text{Otherwise} \end{cases} \quad (\text{A.80})$$

$$\lambda_{PSi} = \chi_{lab} \lambda_{PSi}^{lab} + (1 - \chi_{lab}) \lambda_{PSi}^{ref} \quad (\text{A.81})$$

A.1.14 Calcite

Calcite is the only form of calcium carbonate simulated in PISCES. Hence, aragonite, the other major constituent of calcium carbonate, is not considered. Furthermore, calcite is assumed to exist in the big form only, as for PSi .

The temporal evolution of calcite involves the following three processes:

$$SMS(CaCO_3) = \underbrace{P_{CaCO_3}}_{\text{Calcification}} - \underbrace{\lambda_{CaCO_3}^* CaCO_3}_{\text{Dissolution}} - \underbrace{w_{GOC} \frac{\partial CaCO_3}{\partial z}}_{\text{Sinking}} \quad (\text{A.82})$$

where the production term is defined as:

$$P_{CaCO_3} = R_{CaCO_3} (\eta^Z g^Z(P) Z + \eta^M g^M(P) M + 0.5 (w^P P^2 + m^P \frac{P}{K_m + P} P)) \quad (\text{A.83})$$

$$R_{CaCO_3} = r_{CaCO_3} L_{lim}^{CaCO_3} \frac{T}{0.1 + T} \max(1, \frac{P}{2}) \frac{\max(0, PAR - 1)}{4 + PAR} \frac{30}{30 + PAR} \times (1 + \exp(\frac{-(T - 10)^2}{25})) \min(1, \frac{50}{Z_{mxl}}) \quad (\text{A.84})$$

Here, the rain ratio (R_{CaCO_3}) is parameterized based on *Zondervan* (2007) [147]. Only a fraction of the grazed shells (η^i where $i = Z, M$) will be transformed into calcite. The remmanant is considered to be dissolved in the acidic guts of zooplankton [48].

The dissolution rate is defined following [35]:

$$\Delta CO_3^{2-} = \max(0, 1 - \frac{CO_3^{2-}}{CO_3^{2-}{}_{sat}}) \quad (\text{A.85})$$

$$\lambda_{CaCO_3}^* = \lambda_{CaCO_3} (\Delta CO_3^{2-})^{nca} \quad (\text{A.86})$$

A.1.15 Nitrate

$$\begin{aligned}
 SMS(NO_3) = & - \underbrace{(\mu_{NO_3}^P P + \mu_{NO_3}^D D)}_{GPP} - R_{NH_4} \lambda_{NH_4} \Delta(O_2) NH_4 \\
 & + Nitrif - R_{NO_3} Denit
 \end{aligned} \tag{A.87}$$

where nitrification (*Nitrif*) is a bacterial oxidation process which utilizes ammonium to form nitrate:

$$Nitrif = \lambda_{NH_4} \frac{NH_4}{1 + \overline{PAR}} (1 - \Delta(O_2)) \tag{A.88}$$

$$\overline{PAR} = \overline{PAR_1 + PAR_2 + PAR_3} \tag{A.89}$$

$$\Delta(O_2) = \min(1, \max[0, 0.4 \frac{O_2^{min,1} - O_2}{O_2^{min,2} + O_2}]) \tag{A.90}$$

where \overline{PAR} is the PAR averaged over the mixed layer, λ_{NH_4} is the maximum nitrification rate, R_I (where $I = NH_4, NO_3$) is the N/C stoichiometric ratios, and $\Delta(O_2)$ defines the oxic-anoxic conditions which varies between 0 (oxic) and 1 (anoxic). $O_2^{min,i}$ (where $i = 1, 2$) is the oxygen half-saturation constant for denitrification.

When the waters become suboxic (i.e. $\Delta(O_2) > 0$), nitrate is utilized instead of oxygen for the remineralization of organic matter. This process is known as denitrification (*Denit*):

$$Denit = \lambda_{DOC}^* \Delta(O_2) DOC \tag{A.91}$$

In PISCES, ammonium is assumed to be released from organic matter during denitrification.

A.1.16 Ammonium

$$\begin{aligned}
SMS(NH_4) = & - \underbrace{(\mu_{NH_4}^P P + \mu_{NH_4}^D D)}_{GPP} + N_{fix} - \lambda_{NH_4} \Delta(O_2) NH_4 \\
& + \underbrace{\gamma^Z (1 - e^Z - \sigma^Z) \sum_I g^Z(I) Z + \gamma^M (1 - e^M - \sigma^M) (\sum_I g^M(I) + g_{FF}^M(GOC)) M}_{SloppyFeeding} \\
& + Remin + Denit - Nitri f
\end{aligned} \tag{A.92}$$

where nitrogen fixation (N_{fix}) is a process by which the gaseous form of nitrogen in the atmosphere (N_2) is converted to ammonia (NH_3). In PISCES, it is a source to ammonium and is formulated based on previous studies (e.g. [82, 74, 144]):

$$\begin{aligned}
N_{fix} = & N_{fix}^m \max(0, \mu_P - 2.15) L_N^{Diaz} \\
& \times \min\left(\frac{bFe}{K_{Fe}^{Diaz} + bFe}, \frac{PO_4}{K_{PO_4}^{P,min} + PO_4}\right) (1 - e^{-\frac{PAR}{E_{fix}}})
\end{aligned} \tag{A.93}$$

$$L_N^{Diaz} = \begin{cases} 0.01 & \text{if } z \geq 0.8 \\ 1 - L_N^P & \text{Otherwise} \end{cases} \tag{A.94}$$

where N_{fix}^m is the maximum rate of nitrogen fixation.

A.1.17 Phosphate

$$\begin{aligned}
SMS(PO_4) = & - \underbrace{(\mu^P P + \mu^D D)}_{GPP} + Remin + Denit + \underbrace{\gamma^Z (1 - e^Z - \sigma^Z) \sum_I g^Z(I) Z}_{SloppyFeeding} \\
& + \underbrace{\gamma^M (1 - e^M - \sigma^M) (\sum_I g^M(I) + g_{FF}^M(GOC)) M}_{SloppyFeeding}
\end{aligned} \tag{A.95}$$

where all terms in the above equation have been described previously.

A.1.18 Silicate

$$SMS(Si) = -\underbrace{\theta_{opt}^{D,Si}(1-\delta^D)\mu^D D}_{NPP} + \underbrace{\lambda_{PSi}^*(DissSi)PSi}_{Dissolution} \quad (A.96)$$

where all terms in the above equation have been described previously as well.

A.1.19 Iron

$$\begin{aligned} SMS(Fe) = & -\underbrace{[(1-\delta^P)\mu^{PFe}P + (1-\delta^D)\mu^{DFe}D]}_{NPP} - Coagfe1 - Coagfe2 - Aggfe \\ & + \underbrace{\max[0, (1-\sigma^Z)\frac{\sum_I \theta^{Fe,I} g^Z(I)}{\sum_I g^Z(I)} - e_N^Z \theta^{Fe,Z}]}_{\sum_I g^Z(I)Z} \\ & + \underbrace{\max[0, (1-\sigma^M)\frac{\sum_I \theta^{Fe,I} g^M(I) + \theta^{Fe,GOC} g_{FF}^M(GOC)}{\sum_I g^M(I) + g_{FF}^M(GOC)} - e_N^M \theta^{Fe,Z}]}_{\sum_I g^M(I)M + g_{FF}^M(GOC)} - e_N^M \theta^{Fe,Z} \\ & \underbrace{[\sum_I g^M(I)M + g_{FF}^M(GOC)]}_{SloppyFeeding} + \underbrace{\lambda_{POC}^* SFe}_{Dissolution} - Scav - Bactfe \quad (A.97) \end{aligned}$$

where scavenging of iron by lithogenic particles (*Scav*) [138] is formulated following *Honeyman et al.* (1988) [44] and *Parekh et al.* (2004) [92]:

$$\lambda_{Fe}^* = \lambda_{Fe}^{min} + \lambda_{Fe}(POC + GOC + CaCO_3 + BSi) + \lambda_{Fe}^{dust} Dust \quad (A.98)$$

$$Scav = \lambda_{Fe}^* Fe' \quad (A.99)$$

In the seawater, iron is present largely as colloids. In PISCES, the aggregation of these colloids are represented as *Coagfe1* and *coagfe2*:

$$Coagfe1 = [sh(a_1 DOC + a_2 POC) + a_4 POC + a_5 DOC] Fe_{coll} \quad (A.100)$$

$$Coagfe2 = sh(a_3 GOC) Fe_{coll} \quad (A.101)$$

$Aggfe$ is the loss term due to enhanced scavenging which is triggered when dissolved iron concentration exceeds the total ligand concentration (L_T):

$$Aggfe = 1000\lambda^{Fe} \max(0, Fe - L_T)Fe' \quad (A.102)$$

The uptake of iron by heterotrophic bacteria is parameterized as follows:

$$Bactfe = \mu_P L_{lim}^{Bact} \theta_{max}^{Fe,Bact} \frac{Fe}{K_{Fe}^{B,1} + Fe} Bact \quad (A.103)$$

where $\theta_{max}^{Fe,Bact}$ represents the maximum iron-to-carbon ratio of bacteria.

As seen in the previous equations, dissolved iron (Fe) is expressed in two different forms: free inorganic iron (Fe') and dissolved complexed iron (FeL):

$$Fe' = \frac{-(1 + K_{eq}^{Fe} L_T - K_{eq}^{Fe} Fe) + \sqrt{(1 + K_{eq}^{Fe} L_T - K_{eq}^{Fe} Fe)^2 + 4K_{eq}^{Fe} Fe}}{2K_{eq}^{Fe}} \quad (A.104)$$

$$L_T = FeL + L' \quad (A.105)$$

$$Fe = FeL + Fe' \quad (A.106)$$

$$K_{eq}^{Fe} = \frac{FeL}{L'Fe'} \quad (A.107)$$

$$Fe_{coll} = 0.5FeL \quad (A.108)$$

$$L_T = \max[0.6, 0.09(DOC + 40) - 3] \quad (A.109)$$

A.1.20 Dissolved Inorganic Carbon

$$SMS(DIC) = \underbrace{\gamma^Z(1 - e^Z - \sigma^Z) \sum_I g^Z(I)Z + \gamma^M(1 - e^M - \sigma^M) \left(\sum_I g^M(I) + g_{FF}^M(GOC) \right) M}_{SloppyFeeding} - \underbrace{(\mu^P P + \mu^D D)}_{GPP} + Remin + Denit + \underbrace{\lambda_{CaCO_3}^* CaCO_3}_{Dissolution} - \underbrace{P_{CaCO_3}}_{Calcification} \quad (A.110)$$

where all terms in the above equation have been defined in the previous sections. At the sea surface, CO_2 is exchanged between the ocean and the atmosphere. The gas exchange coefficient is computed following the work of *Wanninkhof* (1992) [139]:

$$k_{g\text{CO}_2} = k'_{g\text{CO}_2}(1 - \%_{ice}) \quad (\text{A.111})$$

Here, $\%_{ice}$ denotes the sea-ice coverage. Atmospheric pCO_2 is an additional parameter of PISCES which is constant both in space and time throughout the simulation period.

A.1.21 Total alkalinity

$$\begin{aligned}
SMS(Alk) = & \theta^{N,C} \left\{ \underbrace{(\mu_{NO_3}^P P + \mu^D D - \mu_{NH_4}^P P - \mu_{NH_4}^D D)}_{GPP} + Remin + (r_{NO_3}^* + 1) Denit \right. \\
& + \underbrace{\gamma^Z (1 - e^Z - \sigma^Z) \sum_I g^Z(I) Z}_{\text{}} \\
& + \underbrace{\gamma^M (1 - e^M - \sigma^M) \left(\sum_I g^M(I) M + g_{FF}^M(GOC) M \right)}_{SloppyFeeding} \\
& + N_{fix} + \Delta(O_2) (r_{NH_4}^* - 1) \lambda_{NH_4} NH_4 - 2 Nitrif \} \\
& + \underbrace{2 \lambda_{CaCO_3}^* CaCO_3}_{Dissolution} - \underbrace{2 P_{CaCO_3}}_{Calcification}
\end{aligned} \quad (\text{A.112})$$

where all terms have been defined previously in this appendix.

The carbonate chemistry (i.e. *DIC* and *Alk*) follows the CMIP protocols except that alkalinity considers only carbonate, borate and water.

A.1.22 Dissolved oxygen

The temporal evolution of oxygen is computed as follows:

$$\begin{aligned}
 SMS(O_2) = & \underbrace{O_2^{ut}(\mu_{NH_4}^P P + \mu_{NH_4}^D D) + (O_2^{ut} + O_2^{nit})(\mu_{NO_3}^P P + \mu_{NO_3}^D D)}_{GPP} \\
 & - \underbrace{O_2^{ut}(\gamma^Z(1 - e^Z - \sigma^Z) \sum_I g^Z(I)Z)}_{SloppyFeeding} \\
 & + \underbrace{\gamma^M(1 - e^M - \sigma^M)(\sum_I g^M(I) + g_{FF}^M(GOC))M}_{SloppyFeeding} \\
 & - O_2^{ut} Remin - O_2^{nit} Nitrif + O_2^{nit} N_{fix}
 \end{aligned} \tag{A.113}$$

where R_2^{ut} is the oxygen-to-carbon ratio when ammonium is converted to organic matter and R_2^{nit} denotes the rate of oxygen consumption during nitrification.

As for CO₂ exchange at the air-sea interface (see Section A.1.20), the exchange of oxygen gas is modeled using the parameterization of *Wanninkhof* (1992) [139] for calculation of the gas exchange coefficient (see Equation A.111). The atmospheric oxygen concentration is constant over time and the the model domain, which however, cannot be set by the user.

A.2 External supply of nutrients

The model incorporates three different sources of nutrient input to the ocean: atmospheric dust deposition, river discharge, and sediment mobilization.

A.2.1 Atmospheric dust deposition

The model incorporates the supply of iron, silicon, phosphorus, and nitrogen particles by atmospheric dust deposition. The iron supply is estimated using the monthly-mean climatology of iron dust deposition [130]. The iron content of dust and its solubility in seawater of dust are set to a constant value of 3.5 % and 2 %, respectively. The dust deposition of silicon and phosphorus is also computed from the same input data and by following the method of *Moore et al.* (2001) [84] and *Moore et al.* (2004) [85], respectively. The phosphorus content of dust is set to 750 ppm [70] and its solubility in surface seawater is set to 10 % [103, 70]. Atmospheric deposition of nitrogen is modeled separately from the deposition of other dust elements that are estimated from the input data of iron dust. Upon the deposition in the surface seawater, all nitrogen dust are assumed to dissolve.

The dust concentration (D_{dust}) is computed in the following way:

$$D_{dust} = \frac{D_{dust}}{w_{dust}} \quad (\text{A.114})$$

where D_{dust} and w_{dust} are the amount of dust deposited at the sea surface and the constant dust sinking speed, respectively.

A.2.2 River discharge

In the model, river runoff provides DIC and DOC, as well as all other nutrients (iron, nitrogen, phosphorus, and silicon) to the ocean. Dissolved organic matter is assumed to remineralize immediately at the river mouth, and therefore, DOC is treated in the model as a source to DIC. The annual-mean climatological river discharge data [68] from the Global Erosion Model (GEM) is used for DIC and DOC input. The supply

of particulate organic carbon is neglected here as most of it is lost in the estuaries and in the coastal zone [119]. River input of iron, phosphorus, nitrogen, and silicon are calculated from the carbon supply by assuming a constant Fe/P/N/Si/C ratios in the rivers from the global estimates [79] [134] [15].

A.2.3 Reductive Mobilization of Iron from Marine Sediments

Iron concentrations in the sediment pore waters are usually several orders of magnitude greater than in the seawater. Previous studies have revealed that this substantial iron increase in the coastal areas is due to reductive mobilization from marine sediments [49, 15, 85]. In the model, this iron supply is parameterized as follows [85]:

$$z_{fesed} = \min(8, (\frac{z}{500})^{-1.5}) \quad (\text{A.115})$$

$$\zeta_{fesed} = -0.9543 + 0.7662 \ln(z_{fesed}) - 0.235(\ln(z_{fesed}))^2 \quad (\text{A.116})$$

$$F_{esed} = \min(1, \frac{\exp(\zeta_{fesed})}{0.5}) \quad (\text{A.117})$$

where all terms have been defined previously. Finally, the iron flux is calculated as:

$$F_{Fe}^{sed} = F_{Fe,max}^{sed} \times F_{esed} \times \%_{sed} \quad (\text{A.118})$$

where $\%_{sed}$ denotes the ratio of the corresponding horizontal grid size of ETOPO5 dataset [90] to the model grid size of PISCES. The above treatment is applied to account for the effect of sub-grid scale bathymetric variations on the iron source function.

A.2.4 Bottom Boundary Conditions

For all sinking tracers (particulate organic matter, biogenic silica, and calcite), the losses due to burials in the sediments are exactly balanced by the external supply from atmospheric dust deposition and river discharge. Hence, for particulate organic matter and biogenic silica, the non-buried part of particles at the bottom ocean is assumed to redissolve back to the water column instantaneously. The proportion of organic matter degradation due to denitrification is determined as follows [80]:

$$\begin{aligned} \log(P_{denit}) = & -2.2567 - 1.185 \log(F_{OC}) - 0.221(\log(F_{OC}))^2 + 0.4721 \log(\max(10, O_2)) \\ & - 0.3995 \log(\max(1, NO_3)) \log(\max(10, O_2)) + 1.25 \log(\max(1, NO_3)) \\ & - 0.0996 \log(z) + 0.4256 \log(F_{OC}) \log(\max(10, O_2)) \end{aligned} \quad (\text{A.119})$$

where the units for the tracer concentrations are in $\mu\text{mol}/L$ and F_{OC} denotes the organic carbon flux at the bottom. The flux of nitrate to the sediment due to denitrification is then computed:

$$F_{NO_3}^{denit} = R_{NO_3} P_{denit} F_{OC} \quad (\text{A.120})$$

The permanent burial of calcite is considered as a function of the saturation level of the overlying waters [3]:

$$\%_{CaCO_3} = \min\left(1, 1.3 \frac{0.2 - \Omega}{0.4 - \Omega}\right) \quad (\text{A.121})$$

where Ω is the saturation level of calcite. The permanent burial of calcite is determined by $\%_{CaCO_3}$.

A.3 Model State Variables

Table A.1: Description of the PISCES state variables

Abbreviations	Units	Description
NO ₃	$\mu\text{mol/L}$	Nitrate
NH ₄	$\mu\text{mol/L}$	Ammonium
PO ₄	$\mu\text{mol/L}$	Phosphate
Si	$\mu\text{mol/L}$	Silicate
Fe	$\mu\text{mol/L}$	Dissolved iron
P	$\mu\text{mol/L}$	Nanophytoplankton
D	$\mu\text{mol/L}$	Diatoms
P ^{Chl}	g/L	Chlorophyll content of nanophytoplankton
D ^{Chl}	g/L	Chlorophyll content of diatoms
P ^{Fe}	$\mu\text{mol/L}$	Iron content of nanophytoplankton
D ^{Fe}	$\mu\text{mol/L}$	Iron content of diatoms
D ^{Si}	$\mu\text{mol/L}$	Chlorophyll content of diatoms
Z	$\mu\text{mol/L}$	Microzooplankton
M	$\mu\text{mol/L}$	Mesozooplankton
DOC	$\mu\text{mol/L}$	Dissolved organic carbon
POC	$\mu\text{mol/L}$	Small particulate organic carbon
GOC	$\mu\text{mol/L}$	Big particulate organic carbon
SFe	$\mu\text{mol/L}$	Small particulate iron
BFe	$\mu\text{mol/L}$	Big particulate iron
PSi	$\mu\text{mol/L}$	Biogenic silica

CaCO ₃	$\mu\text{mol/L}$	Calcite
DIC	$\mu\text{mol/L}$	Dissolved inorganic carbon
ALK	$\mu\text{mol/L}$	Total alkalinity
O ₂	$\mu\text{mol/L}$	Dissolved oxygen

A.4 Model Parameters

Table A.2: PISCES model parameters

Parameter	Units	Default Value	Description
Phytoplankton			
μ_{max}^0	per day	0.06	Growth rate at 0°C
μ_{ref}	per day	1	Growth rate reference for light limitation
b_{resp}	per day	0.033	Basal respiration rate
b_P	-	1.066	Temperature sensitivity of growth
α^I	$(W/m^2)^{-1}/day$	2, 2	Initial slope of P-I curve
δ^I	-	0.05, 0.05	Exudation rate
β_1^I	-	2.1, 1.6	Absorption in the blue part of light
β_2^I	-	0.42, 0.69	Absorption in the green part of light
β_3^I	-	0.4, 0.7	Absorption in the red part of light
$K_{PO_4}^{I,min}$	$nmol/l$	0.8, 2.4	Minimum half-saturation constant for phosphate

$K_{NH_4}^{I,min}$	$\mu mol/l$	0.013, 0.039	Minimum half-saturation constant for ammonium
$K_{NO_3}^{I,min}$	$\mu mol/l$	0.13, 0.39	Minimum half-saturation constant for nitrate
$K_{Si}^{D,min}$	$\mu mol/l$	1	Minimum half-saturation constant for silicate
K_{Si}	$\mu mol/l$	16.5	Parameter for the variation of the half-saturation constant
K_{Si}^1	$\mu mol/l$	2	First parameter for Si/C
K_{Si}^2	$\mu mol/l$	20	Second parameter for Si/C
$K_{Fe}^{I,min}$	$nmol/l$	1, 3	Minimum half-saturation constant for iron uptake
S_{rat}^I	-	3, 3	Size ratio of phytoplankton
$\theta_m^{Si,D}$	$molSi/molC$	0.156	Optimal Si/C uptake ratio of diatoms
$\theta_{opt}^{Fe,I}$	$\mu molFe/molC$	7, 7	Optimal iron quota
$\theta_{max}^{Fe,I}$	$\mu molFe/molC$	40, 40	Maximum iron quota
m^I	per day	0.01, 0.01	Phytoplankton mortality rate
w^P	$day^{-1}mol^{-1}$	0.01	Minimum quadratic mortality of phytoplankton
w_{max}^D	$day^{-1}mol^{-1}$	0.02	Maximum quadratic mortality of diatoms
K_m	$\mu mol/l$	0.2	Half-saturation constant for mortality

$\theta_{max}^{Chl,I}$	$mgChl/mgC$	0.033, 0.05	Maximum Chl/C ratios of phytoplankton
$\theta_{min}^{Chl,I}$	$mgChl/mgC$	0.0033, 0.0033	Minimum Chl/ratios of phytoplankton
I_{max}	$\mu mol/l$	1, 1	Threshold concentration for size dependency
C_m	g/mol	12	Molar mass of carbon
Zooplankton			
b_Z	-	1.079, 1.079	Temperature sensitivity term
e_{max}^I	-	0.3, 0.3	Maximum growth efficiency of zooplankton
σ^I	-	0.3, 0.3	Non-assimilated fraction
γ^I	-	0.6, 0.6	Excretion as dissolved organic matter
g_m^I	per day	3, 0.7	Maximum grazing rate
g_{FF}^M	$(mmol/l)^{-1}$	2×10^3	Flux feeding rate
K_G^I	$\mu mol/l$	20, 20	Half-saturation constant for grazing
p_P^I	-	1, 0.3	Preference for nanophytoplankton
p_D^I	-	0.5, 1	Preference for diatoms
p_{POC}^I	-	0.1, 0.3	Preference for POC
p_Z^I	-	1	Preference for microzooplankton
F_{thresh}^I	$\mu mol/l$	0.3, 0.3	Food threshold for zooplankton
I_{thresh}^Z	$\mu mol/l$	0.01	Specific food thresholds for microzooplankton

I_{thresh}^M	$\mu mol/l$	0.01	Specific food thresholds for mesozooplankton
P_{min}	$\mu mol/l$	0.1	Minimum available concentration for nanophytoplankton
m^M	$(\mu mol/l)^{-1} day^{-1}$	0.03	Zooplankton quadratic mortality
r^I	per day	0.03, 0.005	Excretion rate
ν	-	0.5, 0.75	Fraction of calcite not dissolved in guts
θ_{zoo}^{Fe}	$\mu mol Fe/mol C$	10, 10	Fe/C ratio of zooplankton
Dissolved organic matter			
λ_{DOC}	per day	0.25	Remineralization rate
K_{DOC}	$\mu mol/l$	417	Half-saturation constant for remineralization
$K_{NO_3}^{Bact}$	$\mu mol/l$	0.03	NO_3 half-saturation constant for remineralization
$K_{NH_4}^{Bact}$	$\mu mol/l$	0.003	NH_4 half-saturation constant for remineralization
$K_{PO_4}^{Bact}$	$\mu mol/l$	0.003	PO_4 half-saturation constant for remineralization
K_{Fe}^{Bact}	$nmol/l$	0.01	Fe half-saturation constant for remineralization
a_1	$(\mu mol/l)^{-1} day^{-1}$	0.37	Aggregation rate (turbulence) of DOC → POC

a_2	$(\mu\text{mol}/\text{l})^{-1}\text{day}^{-1}$	102	Aggregation rate (turbulence) of DOC → POC
a_3	$(\mu\text{mol}/\text{l})^{-1}\text{day}^{-1}$	3530	Aggregation rate (turbulence) of DOC → GOC
a_4	$(\mu\text{mol}/\text{l})^{-1}\text{day}^{-1}$	5095	Aggregation rate (Brownian) of DOC → POC
a_5	$(\mu\text{mol}/\text{l})^{-1}\text{day}^{-1}$	114	Aggregation rate (Brownian) of DOC → POC
Particulate organic and inorganic matter			
λ_{POC}	per day	0.025	POC degradation rate
w_{POC}	m/day	2	POC sinking speed
w_{GOC}^{min}	m/day	30	GOC minimum sinking speed
w_{dust}	m/s	2	Sinking speed of dust
a_6	$(\mu\text{mol}/\text{l})^{-1}\text{day}^{-1}$	25.9	Aggregation rate (turbulence) of POC → GOC
a_7	$(\mu\text{mol}/\text{l})^{-1}\text{day}^{-1}$	4452	Aggregation rate (turbulence) of POC → GOC
a_8	$(\mu\text{mol}/\text{l})^{-1}\text{day}^{-1}$	3.3	Aggregation rate (settling) of POC → GOC
a_9	$(\mu\text{mol}/\text{l})^{-1}\text{day}^{-1}$	47.1	Aggregation rate (settling) of POC → GOC
λ_{Fe}^{min}	per day	3×10^{-5}	Minimum scavenging rate of iron
λ_{Fe}	$\text{l}/\mu\text{mol}/\text{day}$	0.005	Slope of the scavenging rate of iron

λ_{Fe}^{dust}	<i>l/mg/day</i>	100	Scavenging rate of iron by dust
λ_{CaCO_3}	per day	0.197	Dissolution rate of calcite
nca	-	1	Exponent in the dissolution rate of calcite
χ_{lab}^0	-	0.31	Proportion of the most labile phase in PSi
λ_{PSi}^{slow}	per day	0.003	Slow dissolution rate of PSi
λ_{PSi}^{fast}	per day	0.025	Fast dissolution rate of PSi
Nutrients			
λ_{NH_4}	per day	0.05	Maximum nitrification rate
$O_2^{min,1}$	$\mu mol/l$	6	Half-saturation constant for denitrification
$O_2^{min,2}$	$\mu mol/l$	1	Half-saturation constant for denitrification
L_T	<i>nmol/l4</i>	0.6	Total concentration of iron ligands
N_{fix}^m	$\mu mol/l/day$	0.013	Maximum rate of nitrogen fixation
K_{Fe}^{diaz}	<i>nmol/l</i>	0.1	Fe half-saturation constant of nitrogen fixation
E_{fix}	W/m^2	50	Photosynthetic parameter of nitrogen fixation
Fe_{ice}	<i>nmol/l</i>	10	Iron concentration in sea-ice
$F_{Fe,min}^{sed}$	$\mu mol/m^2/day$	1	Maximum sediment flux of Fe
Sol_{Fe}	-	0.02	Solubility of iron in dust

Stoichiometric ratios and various parameters			
O_2^{ut}	$molO_2/molC$	131/122	O/C for ammonium-based processes
O_2^{nit}	$molO_2/molC$	32/122	O/C ratio of nitrification
$r_{NH_4}^*$	$molC/molN$	3/5	C/N ratio of ammonification
$r_{NO_3}^*$	$molC/molN$	105/16	C/N ratio of denitrification
$\theta^{N,C}$	$molN/molC$	16/122	N/C Redfield ratio
r_{CaCO_3}	-	0.26	Rain ratio parameter

A.5 Namelist Parameters

Table A.3: Model parameters listed in *namelist_pisces* of NEMO version 3.4.1

Code name	Default value	Description
wsbio	2	POC sinking speed
xkmort	2×10^{-7}	Half-saturation constant for mortality
ferat3	10^{-5}	Fe/C ratio in zooplankton
wsbio	30	GOC sinking speed
conc0	$\times 10^{-6}$	Phosphate half-saturation
conc1	8×10^{-6}	Phosphate half-saturation for diatoms
conc2	10^{-9}	Iron half-saturation for nanophytoplankton
conc2m	3×10^{-9}	Maximum iron half-saturation for nanophytoplankton
conc3	3×10^{-9}	Iron half-saturation for diatoms

conc3m	8×10^{-9}	Maximum iron half-saturation for diatoms
xsize dia	10^{-6}	Minimum size criteria for diatoms
xsize phy	10^{-6}	Minimum size criteria for nanophytoplankton
conc nh4	10^{-7}	NH4 half-saturation for nanophytoplankton
conc dnh4	8×10^{-7}	NH4 half-saturation constant for diatoms
xksi1	2×10^{-6}	Half-saturation constant for Si uptake
xksi2	3.33×10^{-6}	Half-saturation constant for Si/C
xkdoc	4.17×10^{-4}	Half-saturation constant of DOC remineralization
concfbac	10^{-11}	Half-saturation for iron limitation of bacteria
qfelim	7×10^{-6}	Optimal quota of nanophytoplankton
qdfelim	7×10^{-6}	Optimal quota of diatoms
caco3r	0.16	Mean rain ratio
pislope	2	P-I slope
pislope2	2	P-I slope for diatoms
excret	0.05	Excretion ratio of phytoplankton
excret2	0.05	Excretion ratio of diatoms
bresp	0.00333	Basal respiration rate
chlcnm	0.033	Maximum Chl/C in nanophytoplankton
chlcdm	0.05	Maximum Chl/C in diatoms
chlcmin	0.0033	Minimum Chl/c in phytoplankton
fecnm	4×10^{-5}	Maximum Fe/C in nanophytoplankton
fecdm	4×10^{-5}	Minimum Fe/C in diatoms
grosip	0.151	Mean Si/C in diatoms

wchl	0.001	Phytoplankton quadratic mortality of
wchld	0.02	Maximum quadratic mortality of diatoms
mprat	0.01	Phytoplankton mortality rate
mprat2	0.01	Diatoms mortality rate
mpratm	0.01	Phytoplankton minimum mortality rate
part2	0.75	Part of calcite not dissolved in mesozooplankton guts
grazrat2	0.7	Maximal mesozooplankton grazing rate
resrat2	0.005	Exudation rate of mesozooplankton
mzrat2	0.03	Mesozooplankton mortality rate
xprefc	1	Microzooplankton preference for nanophytoplankton
xprefp	0.3	Microzooplankton preference for POC
xprefz	1	Microzooplankton preference for microzooplankton
xprefpoc	0.3	Microzooplankton preference for POC
xthresh2zoo	10^{-8}	Microzooplankton feeding threshold for mesozooplankton
xthresh2dia	10^{-8}	Diatoms feeding threshold for mesozooplankton
xthresh2phy	10^{-8}	Nanophytoplankton feeding threshold for mesozooplankton
xthresh2poc	10^{-8}	POC feeding threshold for mesozooplankton
xthresh2	2×10^{-7}	Food threshold for grazing
xkgraz2	2×10^{-5}	Half-saturation constant for mesozooplankton grazing
epsher2	0.3	Efficiency of mesozooplankton growth
sigma2	0.6	Fraction of mesozooplankton excretion as DOM

unass2	0.3	Non-assimilated fraction of P by mesozooplankton
grazflux	2×10^3	Flux-feeding rate
part	0.5	Part of calcite not dissolved in microzooplankton guts
grazrat	3.0	Maximal microzooplankton grazing rate
resrat	0.03	Microzooplankton exudation rate
mzrat	0.001	Microzooplankton mortality rate
xpref2c	0.1	Microzooplankton preference for POM
xpref2p	1	Microzooplankton preference for nanophytoplankton
xpref2d	0.5	Microzooplankton preference for diatoms
xthreshdia	10^{-8}	Diatoms feeding threshold for microzooplankton
xthreshphy	10^{-8}	Nanophytoplankton feeding threshold for microzooplankton
xthreshpoc	10^{-8}	POC feeding threshold for microzooplankton
xthresh	2×10^{-7}	Food threshold for feeding
xkgraz	2×10^{-5}	half sturation constant for grazing
epsher	0.3	Efficiency of microzooplankton growth
sigma1	0.6	Fraction of microzooplankton excretion as DOM
unass	0.3	Non-assimilated fraction of phytoplankton by microzooplankton
xremik	0.25	Remineralization rate of DOC
xremip	0.025	Remineralisation rate of POC
nitrif	0.05	NH4 nitrification rate
xsirem	0.003	Remineralization rate of Si

xsiremlab	0.025	Fast remineralization rate of Si
xsilab	0.31	Fraction of labile biogenic silica
xlam1	0.005	Scavenging rate of Iron
oxymin	10^{-6}	Half-saturation constant for anoxia
ligand	6×10^{-10}	Ligands concentration
kdca	6	Calcite dissolution rate constant
nca	1	Order of dissolution reaction

